Doctoral Dissertation

Development of Anode Materials for Alkali-Metal-Ion Rechargeable Batteries and Fabrication of Electrode−Electrolyte Interface Enhancing Their Properties

（アルカリ金属イオン二次電池負極材料の創製とそれを活かす電極－電解質界面の構築）

Masahiro Shimizu

January 2016

Department of Chemistry and Biotechnology
Graduated School of Engineering
Tottori University

Preface

The studies presented in this thesis were carried out under the guidance of Professor Hiroki Sakaguchi, Associate Professor Hiroyuki Usui, and Assistant Professor Yasuhiro Domi at Applied Chemistry Course, Department of Chemistry and Biotechnology, Graduated School of Engineering, Tottori University during 2013–2016. The present study has been partially supported by the Japan Society for the Promotion of Science (JSPS) research fellowship (No. 2611485) from 2014 to 2016.

The object of this thesis is to research and develop novel active materials based on alloy for alkali metal-ion rechargeable batteries such as Li-ion and Na-ion batteries. Furthermore, significant enhancement of their electrode performances was tried by fabrication of functional electrode−electrolyte interface enhancing their properties. The author wishes sincerely that the findings from my study would be able to contribute to the achievement of rechargeable batteries with high energy density and high safety.

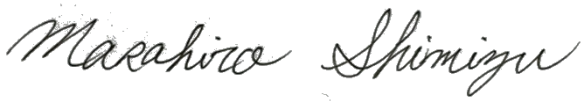

Masahiro Shimizu

Department of Chemistry and Biotechnology
Graduate School of Engineering
Tottori University
4-101 minami, Koyama-cho, Tottori 680-8552, Japan
January 2016

Content

General Introduction

Li-ion batteries are one of the most popular energy storage devices due to their high energy densities. In the light of application for large-scale systems such as power supply for electric vehicles and stationary battery, a further increase in its energy density has been required. Silicon is a promising negative-electrode material replacing the currently used graphite (LiC_6: 372 mA h g^{-1}) due to its high theoretical capacity of 3580 mA h g^{-1} ($Li_{15}Si_4$).[1,2] There is, however, the critical issue that Si undergoes severe volume expansion and contraction during alloying and dealloying reactions with Li. The volumetric changes ratio per Si atom from Si to $Li_{15}Si_4$ corresponds to 380%, which results in the generation of high stresses and large strains in the active material. The strains accumulated by repeated charge−discharge cycling causes disintegration of the Si electrode leading to a rapid capacity fading. This is the main reason why a practical application of Si electrodes has been hindered.

Recently, room temperature ionic liquids have widely applied to an organic synthesis, gas separation, vacuum technology, and energy devices including batteries and electrochemical capacitors in the science and industry field.[3−11] The electrolyte is one of the key factors determining the battery performance. Ionic liquids have received much attentions as an alternative to a conventional organic electrolyte consisting of carbonate-based solvents because of their excellent physicochemical properties of high thermal stability, negligible vapor pressure, and wide electrochemical window.[12−23] In ensuring more safety of the batteries with an increase in the energy density of the batteries, the replacement of a flammable organic solvent with an ionic liquid in an electrolyte solvent can remarkably improve the safety of batteries. Nevertheless, there have been few reports on application of ionic liquid electrolyte to Si-based negative electrode though there were many example of use for carbon-based materials.

On the other hand, there are concerns regarding the maintenance of stable supply of Li for application to such large-scale battery systems. At the present time, the main Li resources are

available in South America, especially Chile and Bolivia, which accounts for 76% of the total.[24,25] Therefore, in the near future, if the demand for Li increases by the popularization of large-scale Li-ion batteries for electric vehicle applications, the price of Li will significantly increase. Therefore, the development of next-generation energy storage devices that use Na-ions as the charge carrier is required. There is no doubt that global Na resources are inexhaustible. However, it would be very difficult to replace Li-ions with Na-ions in the current Li-ion battery system because Na-ions are larger than Li-ions. Thus, in a graphite negative-electrode currently used for a Li-ion battery, Li-insertion into the interlayer occurs to provide a reversible capacity, whereas Na-insertion is hindered due to its size, and charge−discharge reaction hardly occurs.[24–26] Recently, many researchers have studied hard-carbon as a negative electrode.[27–32] Hard-carbon can absorb Na-ions in its nano-scale pores, and exhibits a stable cycle performance, though the capacity is comparatively small such as 250 mA h g^{-1}. In order to further increase energy density of Na-ion batteries, new negatigve-electrode materials with a higher capacity are necessary.

This thesis consists of following eight chapters.

In Chapter 1, the influence of film-forming additive on electrochemical performance of Si negative-electrode for Li-Ion Batteries was evaluated through the use of thick film prepared by gas-deposition without any binder or conductive additive.

In Chapter 2, the ionic liquid consisted of 1-((2-methoxyethoxy)methyl)-1-methylpiperidinium bis(trifluoromethanesulfonyl)amide (PP1MEM-TFSA) were applied to an electrolyte solvent for Li-ion batteries. By using 1-hexyl-1-methylpiperidinium bis(trifluoromethanesulfonyl)amide (PP16-TFSA) including alkyl-substituted piperidinium cation with same chain length as ether-substituted one, the effect of cation structure on anode properties of Si electrodes was investigated.

In chapter 3, the solvation environment for Li ion in piperidinium-based ionic liquid electrolytes was revealed by Raman spectroscopic measurements. In addition, the effect of the solvation environment on the kinetics of interfacial Li-ion transfer between electrode and electrolyte was studied by means of electrochemical impedance spectroscopy using a $Li_4Ti_5O_{12}$ thick-film as a model electrode.

In chapter 4, two-dimensional lithiation distribution on Si electrode surfaces after cycling by Raman mapping analysis was conducted to elucidate the reason for the better performance of Si electrode obtained from PP1MEM-TFSA in chapter 1.

In chapter 5, electrochemical Na-insertion/extraction properties of tin monoxide (SnO) as a new negative-electrode material was examined, and the influence of electrolyte additive on charge−discharge performance was discussed.

In chapter 6, the reactivity of Si against Na was studied using silicon monoxide (SiO) in which Si clusters are finely dispersed in SiO_4 matrices. The reaction mechanism of SiO electrode as a Na-ion battery anode was discussed based on the correlation between crystallite sizes of Si and reversible capacities obtained from the SiO electrodes.

In chapter 7, electrochemical properties of compounds consisted of Sn and P were investigated as NIB anodes, and ionic liquid electrolytes were applied to the Sn−P negative electrode for enhancement of its electrode performance.

In chapter 8, electrochemical behavior of phosphorus as a Na-ion battery anode in ionic liquid electrolytes were investigated, and evaluation of non-flammability of the ionic liquid electrolytes was performed by using a closed-system fire-resistance test in line with the prescribed conditions (*Rapid equilibrium closed cup method*) by International Organization for Standardization and Japanese Industrial Standards Committee.

Finally, concluding remarks are presented.

Chapter 1

Effect of Film-forming Additive on Electrochemical Performance of Silicon Negative-Electrode for Li-ion Batteries

1.1 Introduction

Li-ion batteries have been utilized in large-scale battery systems such as power supply of electric vehicles in recent years. Unfortunately, the conventional Li-ion battery using a graphite negative-electrode has insufficient energy density to satisfy the growing demand. Silicon is one of promising candidates of anode materials for next-generation Li-ion batteries due to its huge theoretical capacity compared with that of graphite practically used. Si and Li form several Li-rich binary alloy phases such as $Li_{15}Si_4$ at room temperature and $Li_{22}Si_5$ at a high temperature of 415 ºC, which offers extremely high theoretical capacities of 3580 and 4200 mA h g^{-1}, respectively.[1,2,33] The volume of Si is, however, significantly changed during alloying/dealloying reactions. The volumetric change ratios per Si atom from Si to $Li_{15}Si_4$ and $Li_{22}Si_5$ correspond to 380% and 410%, which results in a generation of high stress and large strain in the active material. The strain accumulated by repeating charge−discharge cycling causes disintegration of Si electrodes, leading to a rapid capacity fading and a poor cycle stability. In addition, Si has disadvantages of a low electrical conductivity and a low diffusion coefficient of Li^+ in it (D_{Li+}, 10^{-14} to 10^{-12} cm^2 s^{-1}).[34–36] For these reasons, a practical application of Si electrodes has been hindered. To overcome these problems, considerable attempts have been carried out. Many researchers have studied composite materials consisted of carbon, with mechanically soft property and good electrical conductivity, and pure Si.[37–40]

Because an electrolyte solution is one of the key components determining battery performance, it is very important to select optimized electrolyte solution for each Si-based electrode.[41,42] It has been reported that film-forming additives, such as vinylene carbonate (VC),[43,44] fluoroethylene carbonate (FEC),[45–48] succinic anhydride,[49] and

tris(pentafluorophenyl) borane,[50] improve the electrochemical performances of Si-based electrode. A surface film would be formed on the negative-electrode through reductive decomposition of the additives in an initial stage of charging. This surface film should reasonably avoid stress accumulation in localized regions, which suppresses the severe disintegration of the Si-based electrode that leads to rapid capacity fading. However, the effects of film-forming additives on Si itself of active material are unclear; Si-based negative-electrode containing binder and conductive additive have been used in most of the previous studies.

In this chapter, the author investigated the effects of film-forming additives of VC and FEC on the electrochemical performances and the disintegration of Si negative-electrode through the use of thick-film prepared by gas-deposition (GD) without any binder and conductive additive.

1.2 Experimental Details

In preparation of Si thick-film electrodes by a gas-deposition method (Figure 1-1), commercial Si powder (99.9%, Wako Pure Chemical Industries, Ltd.) was used as the raw material. For the gas-deposition, a Cu current collector (20-μm thickness; 99.9%, Nilaco Co., Ltd.) was placed at a distance of 10 mm from the nozzle in a vacuum chamber with a guide tube. The nozzle with a 0.8 mm diameter was connected to the end of the guide tube. An argon carrier gas with a purity of 99.99% was used at a differential pressure of 7.0×10^5 Pa. After the chamber was evacuated to a base pressure of several ten Pa, an aerosol consisting of the argon carrier gas and the Si powder was generated in the guide tube, and instantly gushed from the nozzle onto the Cu substrate. The weight of the deposited active material on the substrate was measured to an accuracy of 1 μg by ultra-microbalance (XP6, METTLER TOLEDO) equipped with an anti-vibration table, and the author used Si thick-film electrode in the range of 28−30 μg.

The author assembled 2032-type coin cells consisted of the obtained GD-film electrode as the working electrode, Li foil (Rare Metallic, 99.9%, thickness: 1.0 mm) as the counter

electrode, electrolyte solution, and glass-based separator. The electrolyte solutions used were 1.0 mol dm^{-3} (M) lithium bis(trifluoromethanesulfonyl)amide (LiTFSA) dissolved in propylene carbonate (PC; $C_4H_6O_3$; Kishida Chemical Co., Ltd.), either alone or containing 5 vol.% of VC ($C_3H_2O_3$; Kishida Chemical Co., Ltd.) or FEC ($C_3H_3FO_3$; Kanto Denka Kogyo Co., Ltd.). The preparation of the electrolyte solution and the cell assembly were carried out in Ar-filled glove box (Miwa MFG, DBO-2.5LNKP-TS) with a dew point below −100 ºC and oxygen content below 1 ppm. Charge−discharge tests were carried out using an electrochemical measurement system (HJ-1001 SM8A, Hokuto Denko Co., Ltd. or BS2506, KEISOKUKI) in the potential range between 0.005 and 2.000 V vs. Li/Li^+ at 303 K under a constant current density of 3.0 A g^{-1} (0.83 *C*). The rate capability was evaluated at various current rates from 0.4 to 10 *C* (1.4 to 36 A g^{-1}). The surface morphology of the Si negative-electrode before and after charge−discharge cycling was observed using a field-emission scanning electron microscopy (FE-SEM, JSM-6701F; JEOL Co., Ltd.).

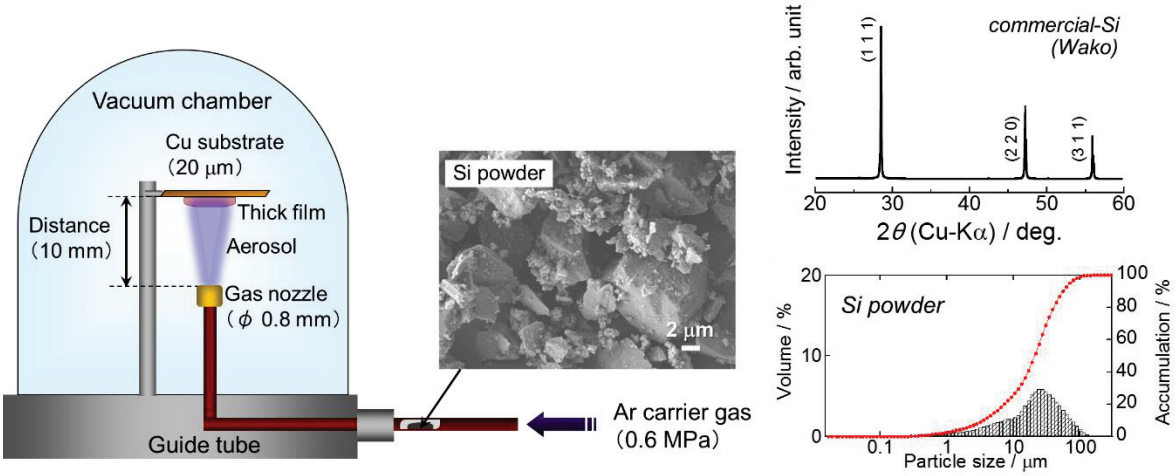

Figure 1-1. (left) Schematic illustration for preparation of Si thick-film electrodes using a gas-deposition method. In this study, Si powder (Wako Pure Chemical Industries, Ltd. 99.9%) with a diameter of 2−10 μm was used as the active material. (right) FE-SEM image, XRD pattern and particle distribution of the Si powder used in this study.

1.3 Results and Discussion

Figures1-2a and 2b show the first charge-discharge (Li insertion-extraction) curves of Si thick-film electrodes in LiTFSA-based electrolyte solutions, and the expansion of its differential capacity curves in negative direction, respectively. As shown in Figure 1-2a, potential plateaus were observed at around 0.1 and 0.4 V vs. Li^+/Li on charge and discharge curves in all electrolyte solutions, respectively. These potential plateaus are attributed to the alloying and dealloying reactions of Si with Li.[1,2] In Figure 1-2b, a peak was observed at around 0.8 V in additive-free electrolyte, which assigned to the reductive decomposition of the electrolyte solution containing LiTFSA and PC. This peak, on the other hand, became smaller in VC-containing electrolyte, and disappeared in FEC-containing one. It has been reported that VC and FEC are reductively decomposed at higher potentials of 1.0−1.1 V to form surface films on Si electrode.[43] Although the fractional peaks which assigned to reductive decomposition of VC and FEC did not appear in Figure 1b, surface films ought to form on Si electrode at the potentials between 1.0 and 1.1 V. On the basis of these results, it is considered that the VC- and FEC-derived surface films are electrical insulating, leading to the suppression of the reductive decomposition of the electrolyte. In addition, the suppressive effect of FEC is stronger than that of VC.

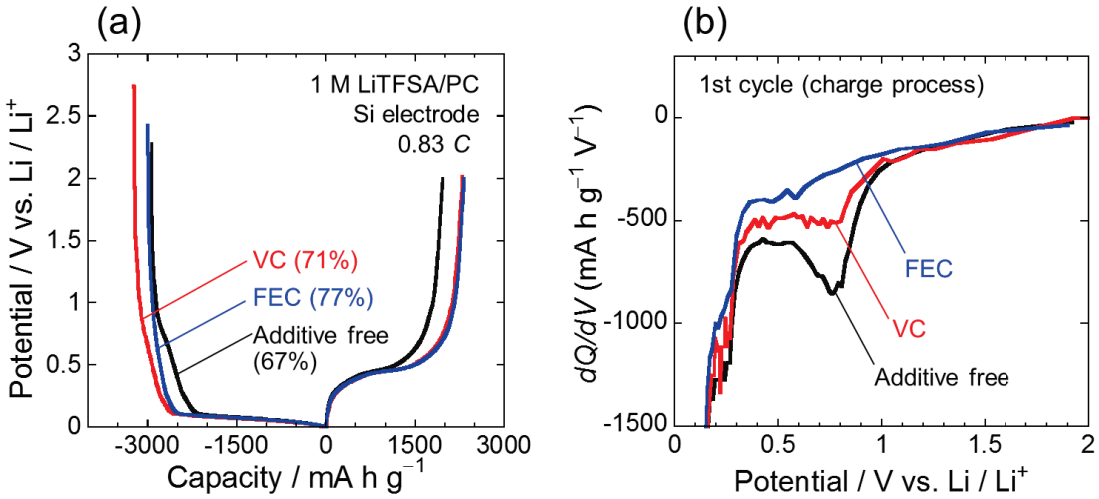

Figure 1-2. (a) First charge−discharge curves of Si thick-film electrodes in 1 M LiTFSA/PC with and without 5 vol.% additives, and (b) enlarged view of its differential capacity curves in the negative direction.

Figure 1-3 shows dependence of discharge capacities on cycle numbers for Si thick-film electrodes in 1 M LiTFSA/PC with 5 vol.% of VC, and FEC. For comparison, a cycle performance with additive-free electrolyte solution is also plotted in this Figure. The Si electrode in additive-free electrolyte showed rapid decay of discharge capacity until 100th cycle, resulting in a very poor cycle performance. As noted above, Si volume significantly changes during alloying/dealloying reactions with Li, and the expansion ratio of the specific volume from Si to $Si_{15}Li_4$ reaches approximately 380%.[1,2] Therefore, this capacity fading is arising from change in the Si volume, which cause exfoliation of active material layer from the current collector and/or pulverization of Si particle. In VC-containing electrolyte, on the other hand, the Si electrode showed better cycle performance; over 500 mA h g^{-1} of the discharge capacity was maintained even after 1000th cycle. As for FEC-containing electrolyte, the discharge capacity was about 350 mA h g^{-1} at 1000th cycle. Therefore, it was revealed that the film-forming additives of VC and FEC significantly improve the cycle performance of Si electrode. To clarify changes in the surface morphology of Si thick-film electrode during charge-discharge cycles, FE-SEM observation was performed.

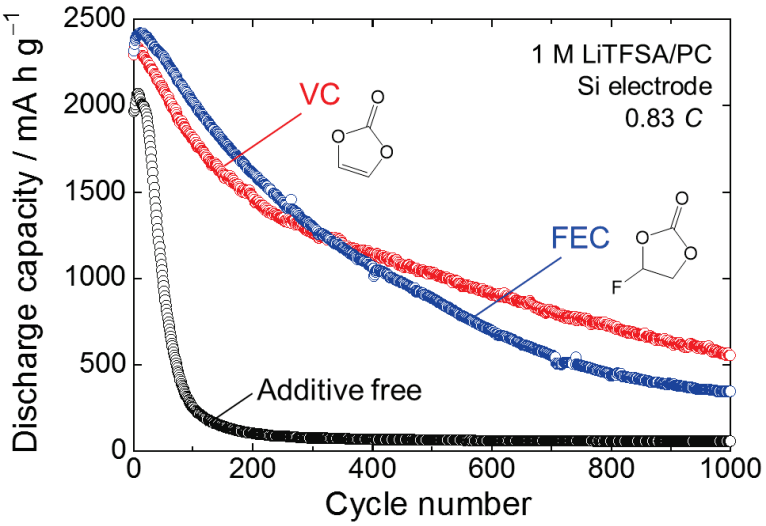

Figure 1-3. Cycling performance of Si thick-film electrodes in 1 M LiTFSA/PC with and without 5 vol.% additives.

Figure 1-4 shows FE-SEM images of Si electrode surface before and after 100th cycles in the electrolytes with and without additives. The as prepared Si electrode exhibited a comparatively smooth surface, as shown in Figure 1-4a. In Figure 1-4b, the author can clearly confirm the disintegration of Si electrode in the electrolyte with no additives related to rapid capacity fading; dead Si seems to be removed. In addition, it is obvious that the regions where the disintegration occurred were localized. After cycling in VC- and FEC-containing electrolytes (Figures 1-4c and 4d), on the other hand, the disintegration of the Si electrode was relatively suppressed, even though an exfoliation of Si and a formation of cracks were observed. The exfoliation was uniformly occurred over the entire electrode compared to that in the electrolyte without additives. Based on these results, VC- and FEC-derived surface films should have mechanical properties to relax high stresses and large strains in the active materials, leading to prevent the disintegration of Si negative-electrode.

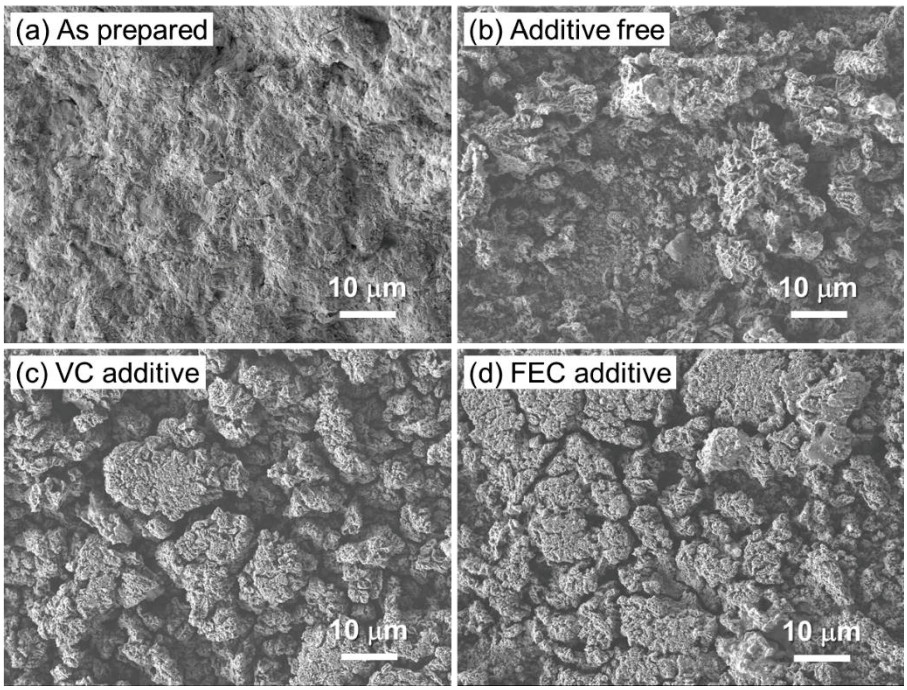

Figure 1-4. FE-SEM images of Si thick-film electrodes (a) as prepared and after 100th charge−discharge cycles (0.83 *C*) in 1 M LiTFSA/PC with (b) no additive, (c) 5 vol.% VC, and (d) 5 vol.% FEC.

While the cycle performance of Si electrode was improved using film-forming additives, capacity fading could not be prevented completely. In order to suppress a little exfoliation of active material and formation of crack during charge-discharge reactions, the amount of Li insertion into Si was controlled. Figure 1-5 shows dependence of discharge capacities on cycle numbers for Si thick-film electrodes in 1 M LiTFSA/PC with and without 5 vol.% film-forming additives at constant charge capacities of 1000 or 1500 mA h g^{-1}. Cycle performance of Si negative-electrode was improved even in the additive-free electrolyte solution; a discharge capacity of 1000 mA h g^{-1} was maintained over 110th cycle, which indicates that the limitation of charge capacity is very effective for an improvement of the cycle performance. Additional increase in durability, however, is demand for the application of LIBs.

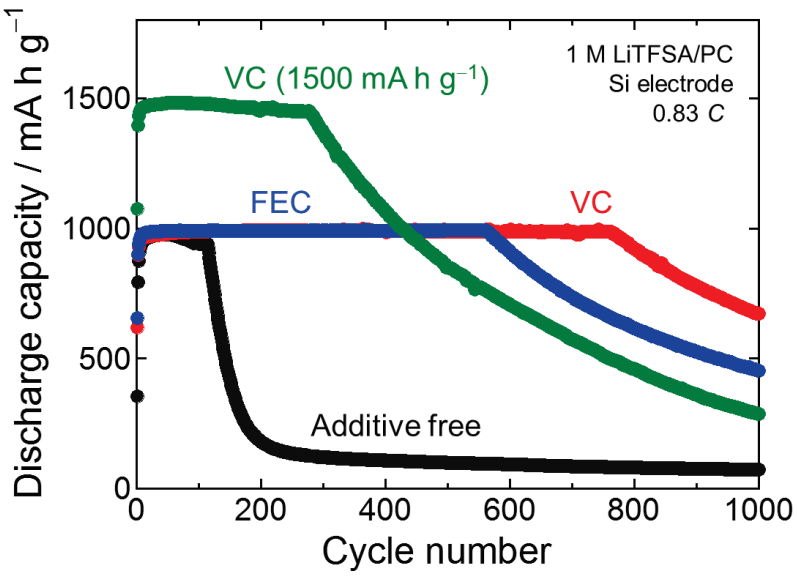

Figure 1-5. Dependence of discharge capacities on cycle numbers for Si electrodes 1 M LiTFSA/PC with and without 5 vol.% additives at constant charge capacities of 1000 or 1500 mA h g^{-1}.

A discharge capacity of 1000 mA h g^{-1} was maintained until 760th and 560th cycles in the electrolyte solutions containing VC and FEC, respectively. In addition, the discharge capacities were 670 and 450 mA h g^{-1} even at 1000th cycle in VC- and FEC-containing electrolytes, respectively. These results indicate that the Si electrode in additive-containing electrolytes show better cycling performance, and that VC improves the durability of Si negative-electrode compared to FEC. It is considered that VC-derived surface film has mechanical properties suitable for relaxation of the stress from Si compared to FEC-derived one, and that disintegration of Si electrode is suppressed in the electrolyte containing VC. The difference in the mechanical properties would be attributed to the chemical structure of these additives; VC has a carbon-carbon double bond, and therefore would be reductively electropolymerized, in addition to ring-opening polymerization, whereas FEC has no double bond.[52,53] In the case of a capacity limitation to 1500 mA h g^{-1} in the electrolyte containing VC, the discharge capacity of 1500 mA h g^{-1} was maintained until 280th cycle, and it was 290 mA h g^{-1} at 1000th cycle, as shown in Figure 1-5. On the basis of these results, it was revealed that an appropriate value of charge capacity is very important in order to obtain good cycle performance.

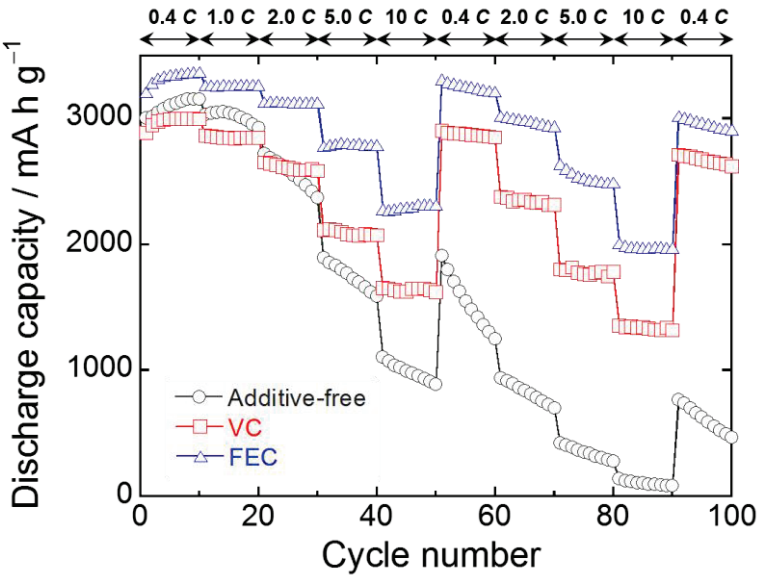

Figure 1-6. Rate performance of Si thick-film electrodes in 1 M LiTFSA/PC with and without 5 vol.% additives at various current rates from 0.4 to 10 C.

Figure 1-6 shows rate performance of Si thick-film electrodes at various current rates from 0.4 to 10 *C* (1.4 to 36 A g^{-1}). The Si electrode in the additive-free electrolyte showed a rapid decay of the discharge capacity at high current rate of 10 *C*; the discharge capacity was about 890 and 80 mA h g^{-1} at 50 and 90th cycles, respectively. When the current rate was returned to the initial value of 0.4 *C*, the discharge capacity was about 470 mA h g^{-1} at 100th cycle which is less than one-sixth of initial value of 3000 mA h g^{-1}. This poor rate capability is attributed to disintegration of Si electrode due to the large volume change during alloying/dealloying reactions with Li. On the other hand, the Si electrode in VC- and FEC-containing electrolytes achieved a comparatively high discharge capacity of ca. 1300 and 2000 mA h g^{-1} even at a high current rate of 10 *C* (90th cycle), respectively. When the current rate was returned to 0.4 *C*, more than 90% of initial discharge capacity was maintained. Consequently, film-forming additives should enable rapid charge-discharge of Si electrode.

Nakai *et al*. have previously reported that FEC-derived surface film protected against not only the decomposition of the electrolyte solution, but also oxidation of the Si negative-electrode.[27] Based on their result, surface of Si electrode was oxidized in the electrolyte solution without FEC after charge-discharge cycles, and then Si oxide was formed. On the other hand, oxidation of Si did not proceed in FEC-containing electrolyte. Consequently, it is considered that better rate performance with FEC is attributed to improvement of Si utilization rate due to non-oxidation of Si.

1.4 Summary

The author investigated the effect of film-forming additives of VC and FEC on the electrochemical performance of Si negative-electrode prepared by a gas-deposition method. Si electrode in VC-containing electrolyte exhibited good cycle performance with the discharge capacity of 1000 mA h g^{-1} beyond 750th cycles at a constant charge capacity of 1000 mA h g^{-1}. In FEC-containing electrolyte, in addition, the discharge capacity of 2000 mA h g^{-1} was

obtained even at a high current rate of 10 *C*. VC- and FEC-derived surface films are electrical insulating, which leads to the suppression of the additional reductive decomposition of the electrolyte. Changes in the surface morphology of Si thick-film electrode in VC- or FEC-containing electrolytes were suppressed compared to those without film-forming additives. Based on our results, it was revealed that VC and FEC effectively improve the electrochemical performances of Si negative-electrode in Li-ion batteries.

Chapter 2

Effect of Cation Structures of Ionic Liquid on Electrochemical Properties of Si Negative-Electrode for Li-ion Batteries

2.1 Introduction

In chapter 1, the author demonstrated that the cycle performance of a Si electrode was significantly improved by using a film-forming additives of VC and FEC.

Meanwhile, room-temperature ionic liquids have received intensive attentions as an alternative to conventional organic electrolytes based on carbonate solvents because of their excellent physicochemical properties of high thermal stability, negligible vapor pressure, wide electrochemical window, and high ionic conductivity.[12–23] The replacement of a flammable organic solvent with an ionic liquid in an electrolyte solvent can remarkably improve the safety of batteries. Nevertheless, there have been a few reports on Si-based electrode in ionic liquid electrolytes. Kim *et al*. prepared a $FeSi_{2.7}$ thin-film by using a RF magnetron sputtering, and investigated its electrochemical behaviors in *N*-buthyl-*N*-methyl-pyrrolidinium bis(trifluoromethanesulfonyl)amide (Py14-TFSA). Although the electrode showed a lower reversible capacity of 760 mA h g^{-1} than that obtained from an organic electrolyte at the first cycle, an excellent capacity retention of 92% at the 100th cycle was achieved in the ionic liquid electrolyte. The reason for the lower initial capacity was suggested to be increase in two kinds of resistance: Li-ion migration in ionic liquid and charge transfer reaction on the electrode.[53] The author also demonstrated that the cycle stability of Si-based electrodes are remarkably improved by applying commercial ionic liquids to an electrolyte solvent.[54,55] In the case of using ionic liquid electrolytes, however, charge−discharge (Li insertion−extraction) capacities of Si electrode are tend to be smaller than that in organic electrolytes due to the slower kinetics of Li-ion transfer at the interface between electrode and electrolyte. In the TFSA-based ionic liquid electrolytes, Li ion is four-coordinated through the oxygen atoms of two bidentate TFSA

anions to form $[Li(TFSA)_2]^-$ ion clusters.[56–59] In addition to this, ionic liquids do not contain any neutral molecules. Therefore, when an electrode is negatively charged, the cations of ionic liquids are accumulated on the electrode surface to compensate the negative charge of the electrode, and the solvated Li-ions ($[Li(TFSA)_2]^-$) exist opposite to the cations in Helmholtz layer, which forms electric double layer at the electrode−electrolyte interface (Figure 2-1).[60] Li-insertion reaction into Si proceeds via several steps: (1) Li-ion migration in the electrolyte bulk, (2) desolvation of $[Li(TFSA)_2]^-$ and Li-ion transport in the electric double layer and/or a solid electrolyte interphase (SEI) layer, (3) alloying reaction of Si with Li, (4) Li diffusion in Si.[61] Among these components, desolvation process is hard to occur by a strong electrostatic interaction between Li ion and TFSA anions, which impedes Li-insertion into Si compared with organic electrolytes systems at low current densities in which solvation/desolvation process controls the reaction rate. In addition, charge and discharge reaction rates are controlled by Li-ion diffusion in an electrolyte bulk under high current densities.[62] Charge−discharge capacities are thus limited in ionic liquid electrolyte systems. The author considers that if cation of ionic liquid has functionality reducing the interaction between Li ion and TFSA anions, it can enable efficient Li-ion transfer at the electrode−electrolyte interface. As a result, Li-insertion reaction can easily occur, and it can provide the enhancement of charge−discharge capacities of Si electrode. Jung *et al*. investigated negative-electrode properties of graphite electrodes in TFSA-based ionic liquid electrolytes consisted of pyrrolidinium cation with various functional groups using cyclic voltammetry, and reported that the Li insertion−extraction properties are involved with cation structure of ionic liquids.[63] There has been, however, no study that tried to improve the electrochemical performance of Si electrodes by modifying cation structure of ionic liquid to the best of author's knowledge.

Our group recently revealed that excellent cycle performanes of Si-based electrodes were achieved in the commercially available ionic liquid consisted of piperidinium cation and TFSA

anion, and that the electrode performances originate from its high stability against cathodic decomposition.[54–55] TFSA-based ionic liquids show a much higher thermal stability than that obtained from ionic liquids with bis(fluorosulfonyl)amide (FSA) anion, which has a strong advantage in the light of insuring safety of battery.[64] In this chapter, therefore, the author introduced ether group having electron-donating ability into piperidinium cation to reduce the electrostatic interaction between Li ion and TFSA anions by its oxygen atom of local negative charge. For comparison, the author also synthesized ionic liquid with alkyl-substituted piperidinium cation having as same chain length as ether-substituted one. In order to directly observe the electrochemical reaction between Si electrode and the electrolyte, Si thick-films prepared by a gas-deposition (GD) method were used. This method does not require any binder and conductive additive to prepare thick-film electrodes.[65] It enables us to clarify an original anode property of pure Si electrode. The author herein reports the effect of cation structure of ionic liquids on anode properties of Si electrodes from the viewpoint of the interaction between Li ion and TFSA anions.

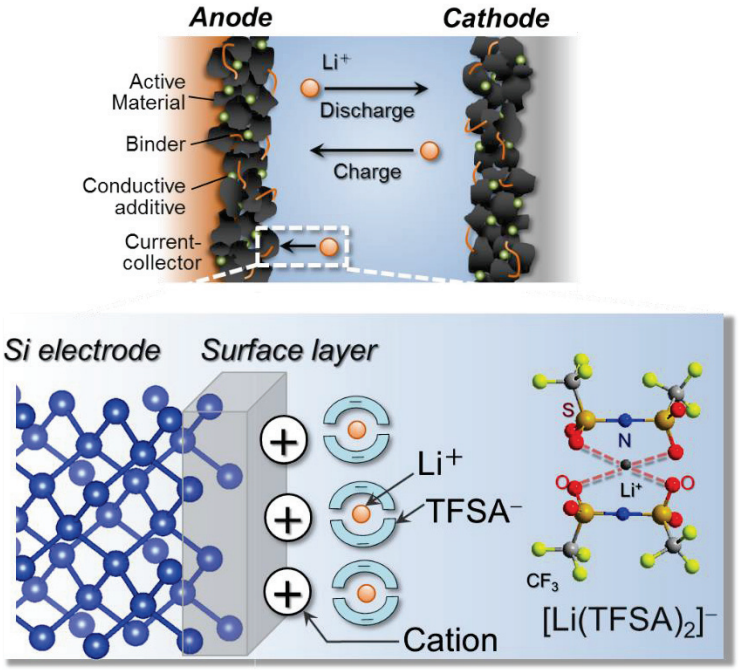

Figure 2-1. Schematic illustration of an electric double layer consisted of cation of ionic liquid and solvated Li-ion ($[Li(TFSA)_x]^{1-x}$) when an electrode is negatively charged (Li-insertion reaction).

2.2 Experimental Details

Characterization of ionic liquids

Two kinds of ionic liquids used in this study were synthesized by an organic method as previously reported[66], and are shown in Figure 2-2. One is 1-((2-methoxyethoxy)methyl)-1-methylpiperidinium bis(trifluoromethanesulfonyl)amide (PP1MEM-TFSA). The other is 1-hexyl-1-methylpiperidinium bis(trifluoromethanesulfonyl)amide (PP16-TFSA). These ionic liquids were dried in a vacuum chamber at 363 K for 24 h for removing water in advance. The water contents of the ionic liquids were confirmed to be less than 50 ppm using a Karl-Fisher moisture titrator (FZ-Compact, Labconco Corporation). The ionic liquid electrolytes were prepared by dissolving the salt of lithium bis(trifluoromethanesulfonyl)amide (99.9%, LiTFSA) in each one at a concentration of 1.0 mol dm^{-3} (M). For comparison, the author used the organic-based electrolyte of 1.0 M LiTFSA-dissolved in propylene carbonate (Kishida Chemical Co., Ltd.). The preparation of the electrolytes was performed within a purge-type glove box (DBO-2.5LNKP-TS, Miwa MFG) filled with an argon atmosphere from which oxygen and water had been completely removed. The glove box maintained a dew point below −100 °C and an oxygen content below 1 ppm.

The viscosity of the ionic liquids was measured by an E-type viscometer (Visconic ED, TOKYO KEIKI Inc.) under air atmosphere at 303 K.

The electrical conductivity was investigated by an electrochemical impedance measurement (CompactStat, Ivium Technologies) through the use of the cell equipped with two Pt electrodes under argon atmosphere at various temperatures from 293 to 353 K.

A thermogravimetric (TG) analysis was conducted to determine thermal decomposition temperature of the ionic liquids by a TG analyzer (Thermo plus EVO II, Rigaku Co., Ltd.) with a heating rate of 10 °C min^{-1} from ambient temperature to 500 °C under argon atmosphere.

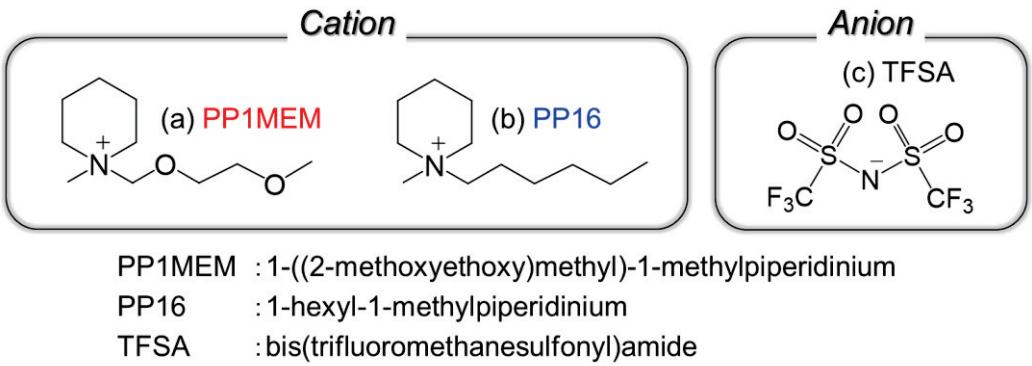

Figure 2-2. Cation and anion structures of ionic liquids used in this study. (a) 1-((2-methoxyethoxy)methyl)-1-methylpiperidinium. (b) 1-hexyl-1-methylpiperidinium. (c) bis(trifluoromethanesulfonyl)amide.

Preparation of Si thick-film electrodes

Si thick-film electrodes were prepared by a gas-deposition method using a commercial Si powder (99.9%, Wako Pure Chemical Industries, Ltd.) and an argon carrier gas (chapter 1).

Evaluation for anode properties of Si electrodes in ionic liquid electrolytes

The author fabricated 2032-type coin cells consisted of a Si thick-film electrode as the working electrode, Li foil (99.90%, thickness: 1.0 mm, Rare Metallic) as the counter electrode, ionic liquid electrolyte, and propylene-based separator. The areas of the Si thick-film and Li sheet in the cell are 0.5 cm^2 and 1.90 cm^2, respectively. The electrolytes were prepared by dissolving a salt of lithium bis(trifluoromethanesulfonyl)amide (LiTFSA) in each piperidinium-based ionic liquid with a concentration 1.0 mol dm^{-3} (M). For comparison, the author used an organic-based electrolyte of 1.0 M LiTFSA-dissolved in propylene carbonate (PC; $C_4H_6O_3$; Kishida Chemical Co., Ltd.). The preparation of the electrolytes and the cell assembly were performed throughout in a purge-type glove box (DBO-2.5LNKP-TS; Miwa MFG) filled with argon atmosphere in which oxygen and water were completely removed. The

glove box maintained a dew point below −100 ºC and oxygen content below 1 ppm. Charge–discharge tests were carried out using an electrochemical measurement system (HJ-1001 SM8A, Hokuto Denko Co., Ltd.) in the potential range between 0.005 and 2.000 V vs. Li/Li^+ at 303 K under the constant current density of 0.42 A g^{-1} (0.12 *C*). An electrochemical impedance spectroscopic (EIS) analysis was performed at 0.005 V vs. Li/Li^+ in the frequency of 100 kHz to 10 mHz with amplitude of 5 mV. The surface morphologies of the Si thick-film electrodes after charge–discharge cycle were observed by a field-emission scanning electron microscope (FE-SEM, JSM-6701F JEOL Co., Ltd.). An analysis of the interactions between Li ion and TFSA anions in each ionic liquid electrolyte were conducted by a Raman microscopy system (NanofinderFLEX, Tokyo Instruments, Inc.) with 532 nm line of Nd:YAG laser at room temperature.

2.3 Results and Discussion

The physicochemical properties of piperidinium-based ionic liquids synthesized in this study are summarized in Figure 2-3 and Table 2-1. PP1MEM-TFSA exhibited approximately half viscosity compared with that of PP16-TFSA, which means that a coulombic interaction between the dissociated cation and anion was weakened by its ether functional group in PP1MEM cation. It is well known that introducing of alkoxy group having electron-donating ability into quaternary ammonium cation reduces viscosity of ionic liquids.[67–69] Consequently, in PP1MEM-TFSA system, the higher conductivities were obtained from not only neat ionic liquid but also the electrolyte. The two kind of ionic liquids showed no decomposition at least up to 250 ºC, though the weight loss of PP1MEM-TFSA was detected at a lower temperature in comparison with PP16-TFSA. The high thermal stability of these ionic liquids is superior to organic solvents, which can enhance the safety of Li-ion batteries.

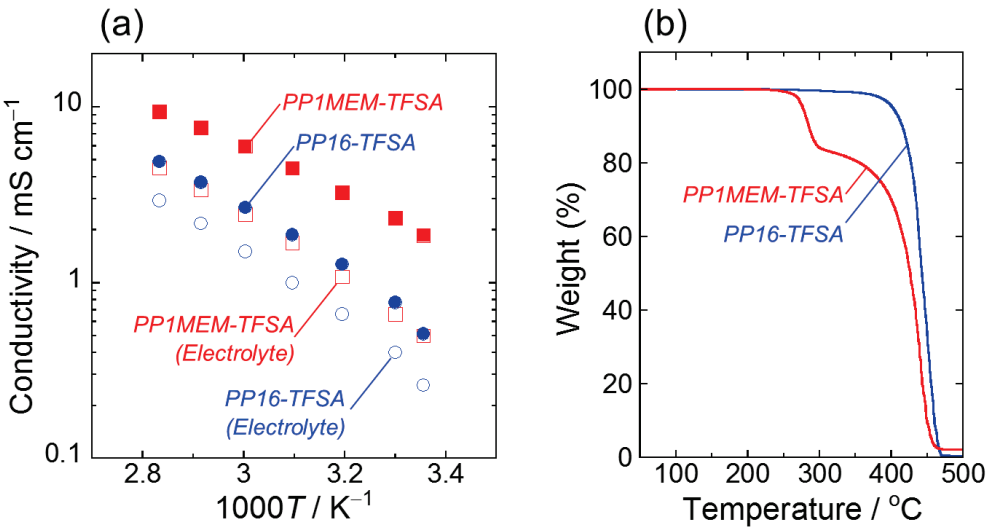

Figure 2-3. (a) Temperature dependence of electrical conductivity of neat ionic liquids and electrolytes consisted of LiTFSA with a concentration of 1.0 mol dm^{-3}. (b) TG curves of neat ionic liquid at the rate of 10 °C min^{-1} under Ar gas.

Table 2-1. Summary of physicochemical properties of TFSA-based ionic liquids synthesized in this study. The electrolytes were prepared by dissolving of LiTFSA with a concentration of 1.0 M.

Cation	M.W.[a]	η [b] / mPa s	σ [c] / mS cm^{-1} (neat)	σ [c] / mS cm^{-1} (electrolyte)	T_{dec} [d] / °C
PP1MEM	468	69	2.3	0.7	285
PP16	464	132	0.8	0.4	415

[a] Molecular weight
[b] Viscosity at 303 K
[c] Conductivity at 303 K
[d] Thermal decomposition temperature (10% weight loss)

Figure 2-4 shows the first charge−discharge (Li insertion−extraction) curves of Si thick-film electrodes in the piperidinium-based ionic liquid electrolytes and organic electrolyte using PC. In every case, potential plateaus were observed at around 0.1 and 0.4 V vs. Li/Li^+ on charge−discharge curves, indicating alloying and dealloying reactions of Si with Li. In PC, the initial charge and discharge capacities were 3640 and 3060 mA h g^{-1}, respectively, with the first coulombic efficiency of 84%. The irreversible capacity is attributed to a formation of surface layer induced by a reductive decomposition of electrolyte, the surface layer is mainly consisted of organic and inorganic compounds such as lithium alkyl carbonates ($ROCO_2Li$) and lithium carbonate (Li_2CO_3).[70] By contrast, Si electrode in PP16-TFSA showed the relatively small discharge capacity of 1780 mA h g^{-1}. The initial charge capacity based on Li−Si alloying reaction can be estimated to be about 2070 mA h g^{-1} from range of Li-insertion plateau between 0.005 and 0.120 V vs. Li/Li^+. This capacity corresponds to 58% of the silicon's theoretical capacity (3580 mA h g^{-1}). It is consider that the low utilization of Si is caused by slow kinetics of Li-ion transfer at the interface between the electrode and the electrolyte.[60–62] In the TFSA-based ionic liquid electrolytes, Li-ion is four-coordinated through the oxygen atoms of two bidentate TFSA anions.[56–59] The strongly electrostatic interaction between Li ion and TFSA anions impedes Li-insertion reaction into Si, which causes the decrease in discharge capacity as well as charge capacity as in the PP16-TFSA. It was noteworthy that the discharge capacity of 2670 mA h g^{-1} was achieved in PP1MEM-TFSA. An important point to be emphasized is that the capacity was much higher than that in PP16-TFSA by *ca*. 900 mA h g^{-1} though these ionic liquids consist of the same anion of TFSA. To evaluate reproducibility, the performances were measured for another electrodes. The standard deviations in the first discharge capacities for PC, PP1MEM-TFSA, and PP16-TFSA are 3058 ± 0.850 mA h g^{-1}, 2681 ± 7.95 mA h g^{-1}, and 1887 ± 106 mA h g^{-1}, respectively. Although the standard deviation in PP16-TFSA is larger than that in PP1MEM-TFSA, a superiority of PP1MEM-TFSA is

evident. This result indicates that introducing of ether functional group into cation is valid to exert the high theoretical capacity of Si. The author thought that the initial large capacity in PP1MEM-TFSA was presumably due to a smooth Li-ion transfer at interface between the electrode and the electrolyte.

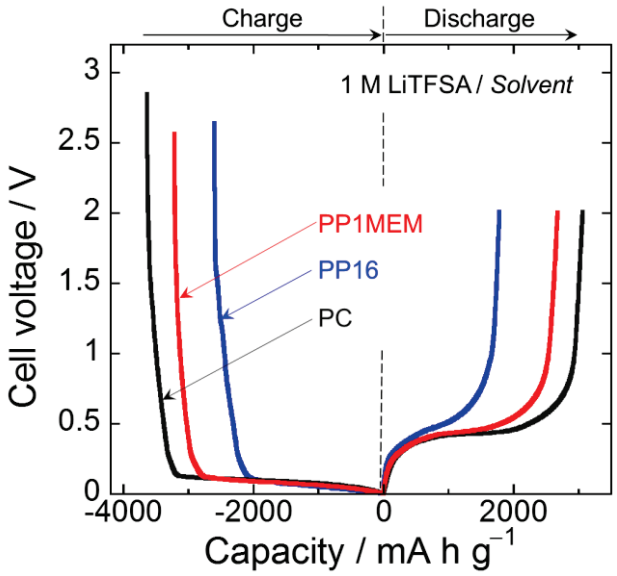

Figure 2-4. Initial charge–discharge curves of Si thick-film electrodes in ionic liquid electrolytes with cations of PP1MEM and PP16, and in an organic-based electrolyte of 1 M LiTFSA-dissolved in PC.

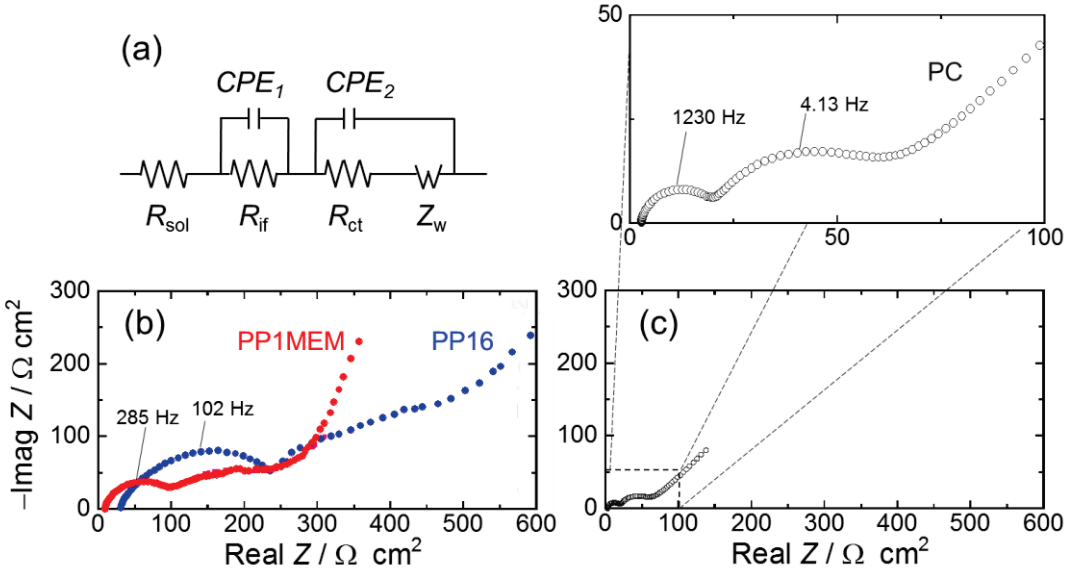

Figure 2-5. (a) Equivalent circuits for impedance analysis in this study. Nyquist plots of Si thick-film electrodes charged at 0.005 V in (b) PP1MEM-TFSA and PP16-TFSA. For comparison, the Nyquist plots in (c) PC were also plotted.

In order to investigate electrochemical behaviors of Li-ion at the interface, an electrochemical impedance measurements were conducted in the frequency range of 100 kHz to 10 mHz. Figure 2-5 displays Nyquist plots of Si thick-film electrode charged at 0.005 V vs. Li/Li^+ in each electrolyte. In all of the Nyquist plots, it was observed two semicircles and a straight line with a slope of approximately 45° in high frequency region and low frequency region, respectively. The first semicircle denotes interfacial resistance (R_{if}), and is associated with interfacial Li-ion transfer processes that includes desolvation of $[Li(TFSA)_2]^-$, Li-ion transport in electrical double layer and/or a surface layer induced by the decomposition of electrolyte. The second semicircle corresponds charge transfer resistance (R_{ct}), and is related to the process of Li−Si alloying reaction. The straight line in the low frequency named as Warburg impedance (Z_w) is derived from solid-state diffusion of Li in Si.[61] Resistances of these components were analyzed by using an equivalent circuit shown in Figure 3a. The author does not discuss here a component of surface layer because it is still a debatable point. The interfacial resistances (R_{if}) in PP1MEM-TFSA and PP16-TFSA were 90 Ω cm^2 and 230 Ω cm^2, respectively, and respective charge transfer resistances (R_{ct}) were 130 Ω cm^2 and 200 Ω cm^2. Both the resistance values in PP1MEM-TFSA were lower than those obtained in PP16-TFSA as expected. In particular, interfacial resistance in PP1MEM-TFSA was less than half of that in PP16-TFSA, indicating a smooth Li-ion transfer at the electrode−electolyte interface. It was speculated that the charge transfer resistance in PP1MEM-TFSA reduced as a result of improving the Li-insertion into the Si electrode. In the case of using PC, the interfacial resistance and charge transfer resistance became the smallest value among the three kind of electrolytes. These lower resistances originate from weaker interaction between Li ion and solvent molecules in organic electrolyte compared with the electrostatic interaction between Li ion and TFSA anions in ionic liquid electrolyte system. The magnitude of charge and discharge capacities in each electrolyte depends on the values of the respective interfacial resistances.

From the results of EIS measurements, the author thought that the smooth Li-ion transfer in PP1MEM-TFSA is owing to the reduced interaction between Li-ions and TFSA anions in comparison with PP16-TFSA.

To investigate the interactions between Li ion and TFSA anions in each ionic liquid electrolyte, Raman spectroscopic measurements were carried out. Figure 2-6 compares Raman spectra for the neat ionic liquids and the electrolytes containing LiTFSA with a concentration of 1.0 M in the frequency range of 730 to 760 cm^{-1}. The intense bands were observed at 742 cm^{-1} in all cases, which is ascribed to the CF_3 bending vibration δ_s (CF_3) coupled with the S−N stretching vibration ν_s (S−N−S) of the TFSA anion.[71–73] This band is assigned to "free" TFSA anions, where Li ion is not coordinated by TFSA anions. In other words, it means the interaction between dissociated cation and TFSA anion in ionic liquid. On the other hand, it is well known that the band position of 742 cm^{-1} showing the interaction shifts to 748 cm^{-1} by coordination of TFSA anions to Li ion.[56,57,74] For electrolytes containing LiTFSA, the author can confirm shoulders at around 748 cm^{-1} in the Raman spectrum of each ionic liquid electrolyte. In addition, the shoulder in the PP1MEM-TFSA was obviously smaller than that observed in PP16-TFSA, which suggests that the interaction between Li ion and TFSA anions in PP1MEM-TFSA is less than that in PP16-TFSA. In order to exactly explore the interactions in each electrolyte, their Raman spectra were separated into the two components including uncoordinated TFSA anions (free TFSA) and coordinated TFSA anions (Li−TFSA) by deconvolution processing as shown in Figure 2-6.

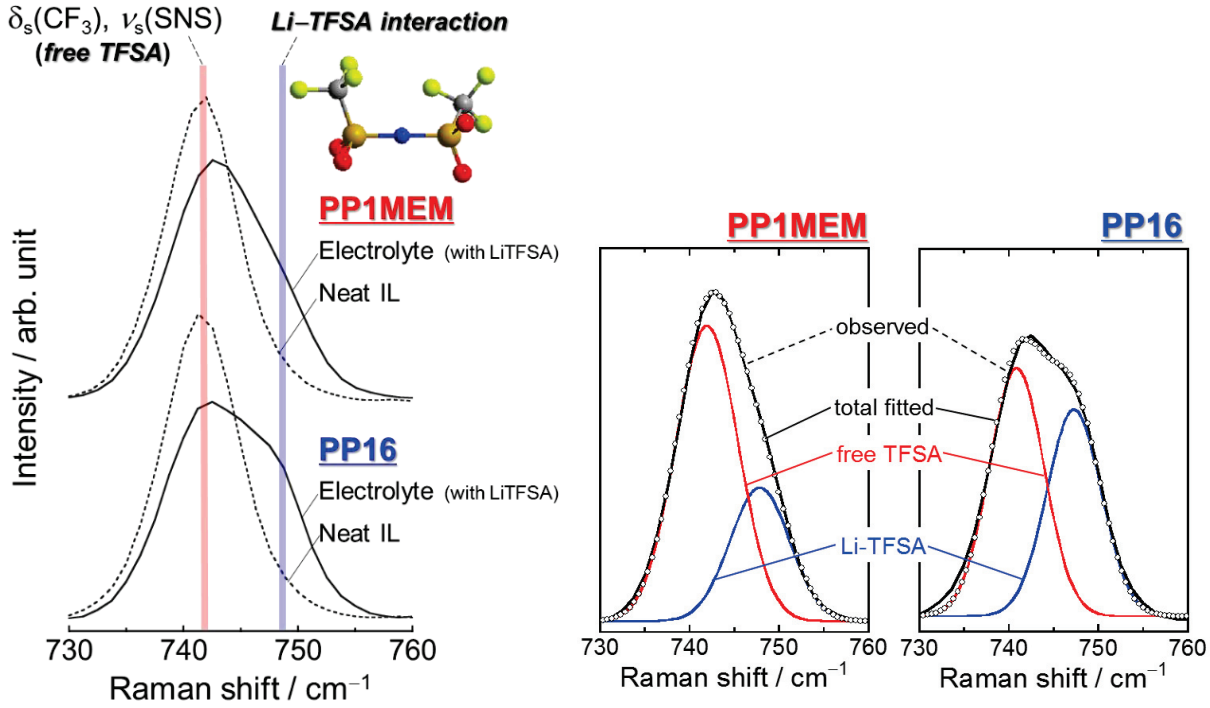

Figure 2-6. (left) Raman spectra of ionic liquids and the electrolytes consisted of the piperidinium-based ionic liquids and LiTFSA in the frequency range of 730 to 760 cm^{-1}. The cations of ionic liquids are PP1MEM (upper) and PP16 (lower), respectively. (right) Decomvoluted Raman bands of 1.0 M LiTFSA-dissolved in PP1MEM-TFSA and PP16-TFSA. The dotted, black, blue, and red lines show the observed spectrum, the total Raman spectrum, the deconvoluted components of free TFSA anion and coordinated TFSA anion (Li−TFSA).

Comparing the intensity ratios of coordinated TFSA that interacts with Li ions, the relative ratio of Li−TFSA interaction in PP1MEM-TFSA system was smaller than that PP16-TFSA system. Kunze *et al*. have studied an interaction in mixture of LiTFSA and pyrrolidinium-based ionic liquid with cation having alkyl side chain or ether side chain by Raman spectroscopic measurement and nuclear magnetic resonance analysis.[74] According to this literature, less than two anions are required for the coordination of Li ion in 1-(ethoxymethyl)-1-methylpyrrolidinium bis(trifluoromethanesulfonyl)amide (Pyr1[2O1]-TFSA) whereas more than two TFSA anions are necessary to solvate Li ion in the 1-butyl-1-methylpyrrolidinium bis(trifluoromethanesulfonyl)amide (Pyr14-TFSA). The coordination number of TFSA anions to Li ion are 1.55 and 2.12, respectively. This result indicates that the Li−TSFA interaction can

be weaken by introducing of ether functional group into cation of ionic liquid, and agrees with our results of Raman measurements. The intensity ratios of Li−TFSA to uncoordinated TFSA (free TFSA) in PP1MEM-TFSA and PP16-TFSA are 0.19 and 0.34, respectively, which suggests that the coordination number of TFSA anions to Li ion in PP1MEM-TFSA is less than two, and smaller than that in PP16-TFSA. Although the total charge of PP1MEM cation is +1.0, the oxygen atoms in the cation are negatively charged due to its electron-withdrawing nature. The author therefore considers the effect reducing the interaction between Li ion and TFSA anions by PP1MEM cation originates from the two oxygen atoms in the cation structure. Possible reasons for the small coordination number in PP1MEM-TFSA are one or more of the following: (i) a repulsive force due to electrostatic interaction between TFSA anion and local negative charge of oxygen atoms in the PP1MEM cation, (ii) an attractive force due to electrostatic interaction between an isolated Li ion and the oxygen atoms, (iii) an attractive electrostatic interaction between Li ion binding with TFSA anion and the oxygen atoms. However, it is thought that Li ion in TFSA-based ionic liquid electrolytes is preferentially solvated by TFSA anions owing to a very strong interaction between Li ion and TFSA anion.[60] In addition, the results of Raman measurements for the ionic liquid electrolytes shows the fact that the interaction between Li ion and the oxygen atoms of PP1MEM cation coexists with the interaction between Li ion and TFSA anion, which is probably in a competitive relationship. Tsuzuki *et al*. have studied the an interaction of LiTFSA complex with *N*,*N*-diethyl-*N*-methyl-*N*-2-methoxyethylammonium (DEME) cation and DEME-TFSA by ab initio molecular calculations.[50] Interaction energy potentials (E_{int}) calculated for DEME-Li systems in various geometries are always repulsive though the potential has a local minimum when the Li ion approaches the oxygen atom in DEME cation with a distance of 2.0 Å, which shows that an isolated Li ion does not form the stable complex with DEME cation. Meanwhile, the potential calculated for DEME−LiTFSA complex has a minimum in a similar way to the DEME-Li

system when the Li···O distance is 2.0 Å. E_{int} of fully optimized geometry of the DEME-LiTFSA complex at the HF/6-311G** level is −18.4 kcal mol^{-1}. Furthermore, they calculated an interaction between DEME-TFSA and LiTFSA complex in view of a bulk ionic liquid environment, and reported that its E_{int} (−23.2 kcal mol^{-1}) for most stable orientation is substantially larger than that for the DEME−LiTFSA complex. Based on the results of ab initio calculations, the author considers the effects of the PP1MEM cation on the coordination number of TFSA anion to Li ion as follows. PP1MEM cation in the electrolyte attracts Li ion interacting TFSA anion through the two oxygen atoms in the cation structure by an electrostatic interaction between the positively charged Li ion and the negatively charged oxygen atoms. After that, a complex consisted of PP1MEM cation and LiTFSA is formed, and the complex is surrounded by an additional TFSA anion for a charge compensation. On the other hand, alkyl group of PP16 cation has no electron-withdrawing nature, and thereby permit at least more than two TFSA anions to coordinate Li ion. This appears to be a reason why the coordination number of TFSA anions to Li ion in PP1MEM-TFSA is smaller than that in PP16-TFSA. When an negative electrode is charged to provide capacity, the cations of ionic liquids are accumulated on the electrode surface, and the $[Li(TFSA)_x]^{1-x}$ exists opposite the cations in Helmholtz layer. The symbol "x" denotes coordination number, and generally results in "2".[74] Desolvation of $[Li(TFSA)_x]^{1-x}$ occurs at the electrode−electrolyte interface before Li-insertion into Si. The desolvation process is impeded by strongly electrostatic interaction between Li ion and TFSA anions in comparison with organic electrolytes system, which limits charge−discharge capacities in the ionic liquid electrolytes system. In consequence, the capacities become smaller with increasing coordination number due to its slow kinetics, as observed in PP16-TFSA. It was revealed that PP1MEM cation played a role reducing the interaction between Li ion and TFSA anions, and the coordination number was less than two. The decrease in the number led to significant increase in capacities of Si electrode. It was

demonstrated that PP1MEM cation enhanced not only Li-ion transfer at the electrode−electrolyte interface but also the initial charge−discharge capacities of Si electrode.

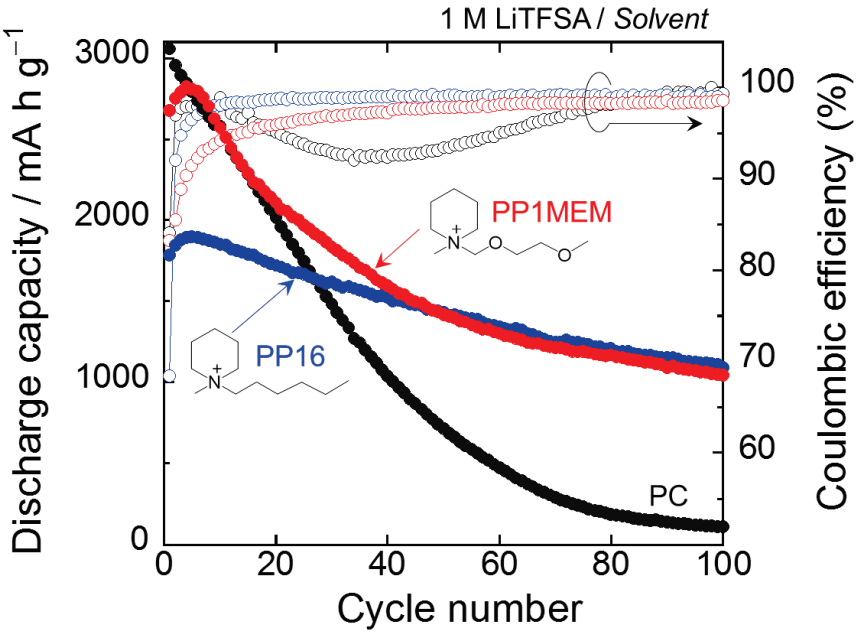

Figure 2-8. Dependence of discharge (Li-extraction) capacities and coulombic efficiencies on cycle numbers for Si electrodes in PP1MEM-TFSA and PP16-TFSA. For comparison, the performance in PC was also plotted.

Figure 2-7 represents a dependence of discharge (Li-extraction) capacities and coulombic efficiencies on cycle numbers for Si electrodes in the piperidinium-based ionic liquid electrolytes. For comparison, the performance in PC was also plotted in this figure. Although Si electrode in PC showed the high discharge capacity of 3060 mA h g^{-1} at the first cycle, the capacity was quickly decreased to 110 mA h g^{-1} by 100th cycle, resulting in a very poor cycle performance. The significant capacity decay is attributed to a disintegration of Si electrode caused by a stress generated during alloying/dealloying reaction of Si with Li. Although the coulombic efficiency of the electrode in PC was temporarily increased to 99% at the 10th cycle, the efficiency was decreased to 92% at the 33th cycle. The decline results from the disintegration such as the peeling of the active material from the current collector. On the other

hand, The Si electrode in PP1MEM-TFSA showed the first coulombic efficiency of 83%, which is larger than that obtained from PP16-TFSA (68%). These irreversible capacities come from the decomposition of electrolytes to form a surface layer on the anode. It was reported that surface layer derived from TFSA-based ionic liquids is composed of lithium fluoride (LiF), lithium carbonate (Li_2CO_3), lithium sulfate (Li_2SO_4), and lithium sulfite (Li_2SO_3).[23] The Si electrodes in PP1MEM-TSFA and PP16-TFSA gave better cyclability: the capacities of over 1000 mA h g^{-1} were maintained even after 100th cycle. The author was able to confirm the excellent reproducibility of anode performances in each case, and an advantage of utilization of ionic liquid electrolyte are obvious throughout the 100 cycles test (Figure 2-8).

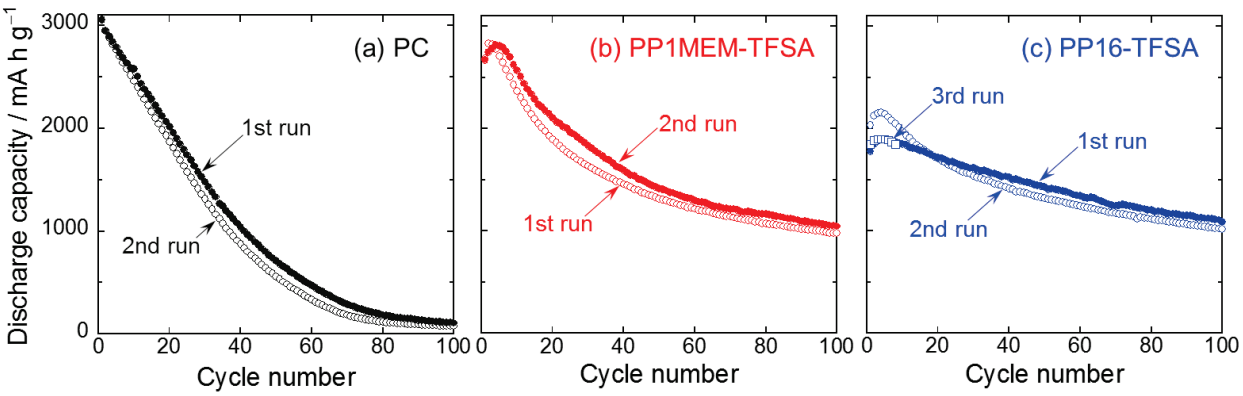

Figure 2-8. Results of reproductive experiment for cycling performances of Si electrode in (a) PC, (b) PP1MEM-TFSA, and (c) PP16-TFSA. To evaluate reproducibility, the performances were measured for another electrodes as 2nd or 3rd run sample.

Although the capacity in PP1MEM-TFSA was higher than that in PP16-TFSA until 40th cycle, behaviors of cycle performances in each electrolytes overlapped after 50th cycle. From range of Li-insertion plateau between 0.005 and 0.120 V vs. Li/Li^+, the initial lithiation capacities based on Li−Si alloying reaction in PP1MEM-TFSA and PP16-TFSA can be estimated to be about 2800 mA h g^{-1} and 2070 mA h g^{-1}, respectively. These capacities are basically close to

the theoretical capacity of $Li_{13}Si_4$ (3110 mA h g^{-1}) and Li_7Si_3 (2230 mA h g^{-1}), and the volumetric change ratios per Si atom from Si to $Li_{13}Si_4$ and Li_7Si_3 correspond to 340% and 260%.[51] The Si in PP1MEM-TFSA expands by the difference in the volumetric change ratio, which results in a generation of a larger strain in the active material. In addition, the author could not confirm an additional potential plateau or a shoulder related to the electrolyte decomposition with the exception of lithiation reaction from the charge profiles after second cycle (Figure 2-9). It is suggested that the lower efficiency in PP1MEM-TFSA is not relevant to the formation of surface layer such as solid electrolyte interphase (SEI). From the above, the reason for the capacity decay in the initial 40th cycle in PP1MEM-TFSA is considered to be due to the greater breakup of Si electrode. It was noteworthy that the Si electrode in PP1MEM-TFSA exhibited the initial capacity comparable to that in PC but still attained the high capacity of 1050 mA h g^{-1} at the 100th cycle. The essential difference in electrode performances obtained from the ionic liquid electrolyte and the organic electrolyte will be reported in future article.

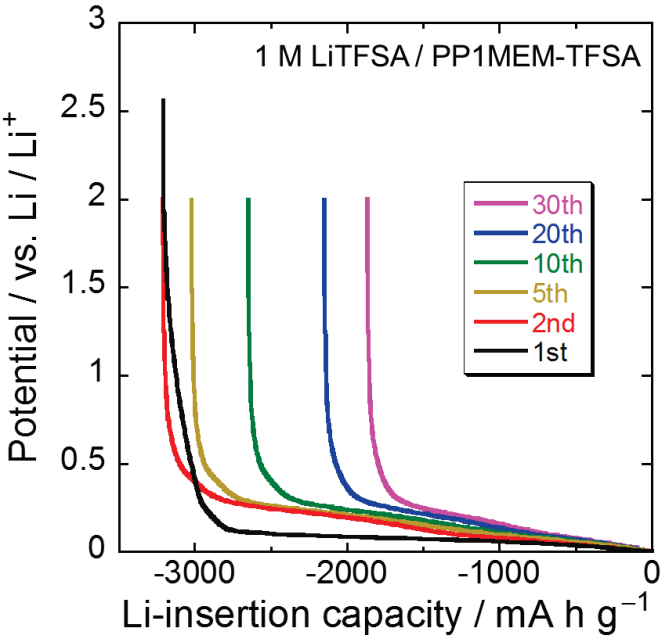

Figure 2-9. Charge (Li-insertion) profiles of Si thick-film electrode in PP1MEM-TFSA.

Figure 2-10 displays FE-SEM images of the Si electrodes before and after 100th charge−discharge cycle in PC, PP1MEM-TFSA, and PP16-TFSA. The as prepared Si electrode showed a comparatively smooth surface as shown in Figure 2-10a. After cycling in PC, the author can clearly observe the disintegration of Si electrode related to the rapid capacity fading (Figure 2-10b). On the contrary, the disintegration of Si electrodes were relatively suppressed in the cases of using the ionic liquid electrolytes though there were changes in surface morphology such as partial breakup and the formation of cracks (see Figures 2-10c and 10d). Among them, the degree of disintegration of Si electrode in PP1MEM-TFSA was larger than that in PP16-TFSA, which also means that the capacity decay of Si electrode during the initial 40th cycle in PP1MEM-TFSA originates from the disintegration of the electrode.

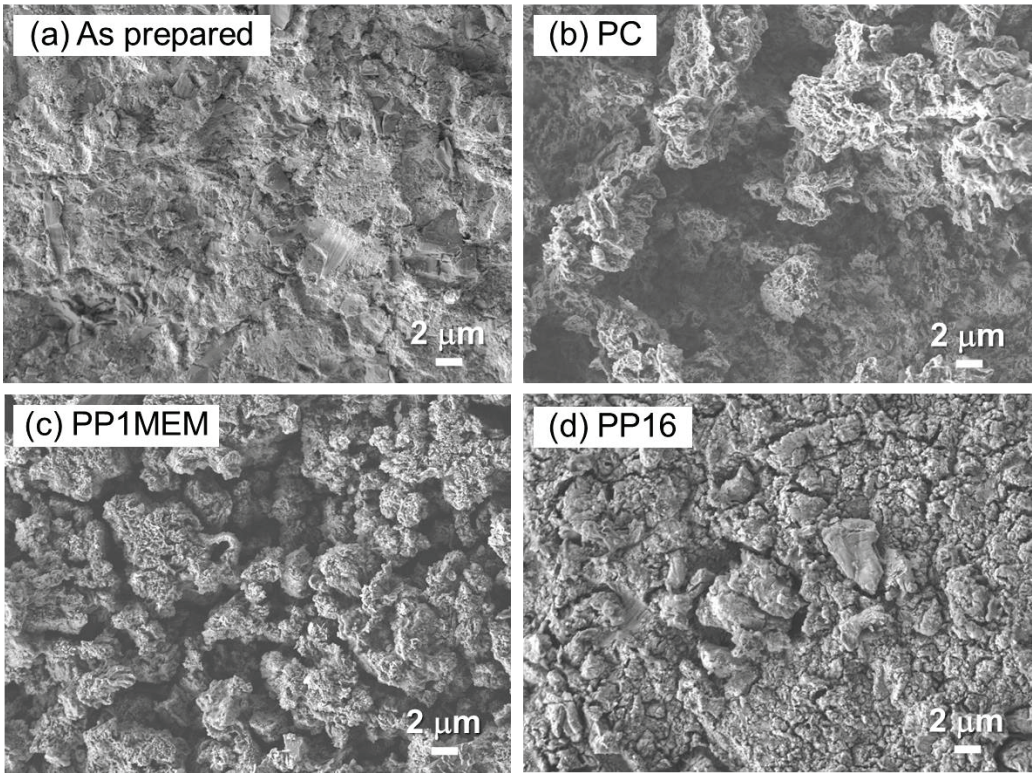

Figure 2-10. FE-SEM images of Si thick-film electrodes (a) as prepared and after 100th charge–discharge cycle in (b) PC, (c) PP1MEM-TFSA, and (d) PP16-TFSA.

Figure 2-11 illustrates a rate performance of Si electrodes in ionic liquid electrolytes. The characteristic of PP1MEM cation that reduces the interaction between Li ions and TFSA anions is expected to upgrade an anode performance of Si electrodes at high-rate charge−discharge condition. The rate capability was evaluated at various current densities from 420 (0.12 *C*) to 8400 mA g^{-1} (1.2 *C*). The Si electrode in PP16-TFSA showed a rapid capacity decay with increasing current density: the capacity at 1.2 *C* was 210 mA h g^{-1}, which corresponds to about one-tenth of the capacity at 0.12 *C*. This poor rate capability results from slow kinetics of interfacial Li-ion transfer between the electrode and the electrolyte. On the other hand, PP1MEM-TFSA delivered a comparatively high discharge capacity of 1150 mA h g^{-1} even at a high current density of 4200 mA g^{-1} (1.2 *C*), indicating that the Li-ion transfer was remarkably improved by PP1MEM cation. An application of PP1MEM-TFSA to Si-based composite electrodes that the author has demonstrated their superiority expects that the electrode performance can be further improved.

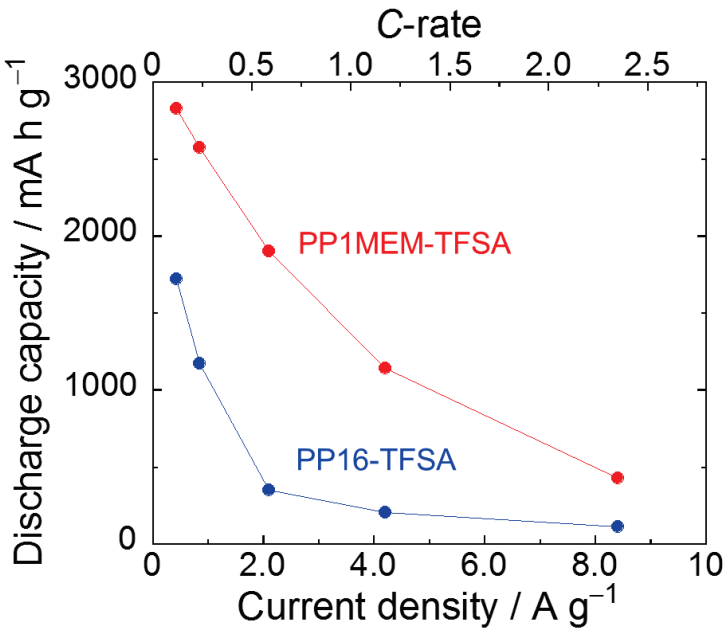

Figure 2-11. Rate capability of Si electrodes in PP1MEM-TFSA and PP16-TFSA at various current rates from 0.42 to 8.4 A g^{-1}.

2.4 Summary

The Si thick-film electrodes were prepared by a gas-deposition method, and the influences of cation structure of ionic liquid on anode properties of Si electrodes were investigated from the viewpoint of interaction between Li ion and TFSA anions. The Si electrode in ionic liquid consisted of PP1MEM cation having electron-donating group and TFSA anion exhibited the high discharge capacity of 2670 mA h g^{-1} at the first cycle, which is larger than that in PP16-TFSA by *ca*. 900 mA h g^{-1}. Raman analysis and EIS measurements revealed that PP1MEM cation played a role reducing the interaction between Li ion and TFSA anions, and that Li-ion transfer at the interface between electrode and electrolyte was improved compared with PP16-TFSA. The excellent cycle performances, discharge capacities of over 1000 mA h g^{-1} at 100th cycle, were attained in both the ionic liquid electrolytes whereas the Si electrode in PC showed the capacity of 110 mA h g^{-1}. Additionally, the improved interfacial Li-ion transfer, the smooth Li-insertion into Si in PP1MEM-TFSA led to a good high-rate performance: the capacity of 1150 mA h g^{-1} at relatively a high current density of 4200 mA g^{-1} (1.2 *C*) was achieved. These results indicates that the introduction of ether functional group into cation structure is effective strategy for enhancement of anode performance of Si electrodes.

Chapter 3

Influence of Cation Structure on Interfacial Li-ion Transfer between Electrode and Ionic Liquid Electrolyte: Analysis of Reaction Kinetics Using $Li_4Ti_5O_{12}$ as a Model Electrode

3.1 Introduction

An electrolyte, one of the three main constituents of a battery, is a key factor which governs the battery performance such as a reversible capacity and a cycle stability. Room-temperature ionic liquids have been regarded as an alternative to a conventional organic electrolyte for Li-ion batteries due to their favorable properties of non-flammability, negligible vapor pressure, wide electrochemical window, and high ionic conductivity.[12–23] The replacement of a flammable organic solvent with an ionic liquid in an electrolyte solvent can remarkably improve the safety of batteries. It is well known that ionic liquids including bis(trifluoromethanesulfonyl)amide (TFSA) anion show a low melting point and a high electrochemical stability.[8–11] Many researchers have studied the feasibility of applying the TFSA-based ionic liquids to an electrolyte solvent.[77,79,80] The use of the ionic liquids, however, causes critical issues concerning kinetics of Li-ion transfer at the electrode−electrolyte interface.[81–84] In the TFSA-based ionic liquid electrolytes, Li ion is four-coordinated through the oxygen atoms of two bidentate TFSA anions to form $[Li(TFSA)_2]^-$ clusters in which Li ion strongly interacts with the TFSA anions by Coulomb force. [56–59] The interaction is much larger than that between Li ion and molecule solvents in an organic electrolyte system. This phenomenon limits Li-insertion into a negative electrode at low current densities in which solvation/desolvation process controls the reaction rate. In addition, charge and discharge reaction rates are controlled by Li-ion diffusion in an electrolyte bulk under high current densities. Consequently, the use of an ionic liquid electrolyte which generally has a strong electrostatic interaction in itself and has a lower diffusion coefficient of Li ion than that in an

organic electrolyte results in the reason for restriction of a reversible capacity at a high rate.[60,62,83]

In chapter 2, the author demonstrated that the cycle stability of a Si negative-electrode can be markedly improved by using the ionic liquid consisting of methoxyethoxymethyl-modified piperidinium cation and TFSA anion (PP1MEM-TFSA).[83] Furthermore, the Si electrode in the ionic liquid electrolyte exhibited the higher initial reversible-capacity than that in an ionic liquid consisting of alkyl-substituted piperidinium cation and TFSA anion (PP16-TFSA) by *ca*. 900 mA h g^{-1} at a relatively low current density of 0.12 *C* though the capacity obtained from the organic electrolyte of 1 M LiTFSA-dissolved in propylene carbonate (PC) was largest among the three kinds of electrolytes.[83] The results suggested that the cation structure of ionic liquids used as an electrolyte solvent strongly influenced the Li-insertion into the electrode.[63] the author inferred that the PP1MEM cation kinetically promoted the interfacial Li-ion transfer between electrode and electrolyte. The hypothesis has remained as a matter to be discussed further. Nonetheless, the kinetic analysis of Li-insertion into the negative electrode is a quite challenge because Si absorbs Li through multi-stage alloying reactions, and the large volumetric changes in Si during charge−discharge reactions cause the severe disintegration of the electrode. The author therefore focused on spinel-type $Li_4Ti_5O_{12}$ which is practically used in a negative electrode for a commercial Li-ion battery. $Li_4Ti_5O_{12}$ has been recognized as a safer active material preventing Li dendritic growth due to its higher Li insertion−extraction voltages at 1.55 V vs. Li/Li^+ than other anode materials such as graphite (C), silicon (Si), and tin (Sn). The Li-insertion mechanism is an intercalation type and the reaction proceeds based on two-phase between spinel-type $Li_4Ti_5O_{12}$ ($Li_{8a}[Li_{1/3}Ti_{5/3}]_{16d}O_4$) and rocksalt-type $Li_7Ti_5O_{12}$ ($[Li_2]_{16c}[Li_{1/3}Ti_{5/3}]_{16d}O_4$), showing a very flat plateau in charge−discharge potential curves.[85−87] Furthermore, there is little change in the lattice parameter during charge and discharge reactions, and thus achieve a high reaction reversibility and an excellent cycle stability for a

long period without noticeable capacity decay.[88,89] These characteristics are very suitable for the kinetic analysis of interfacial Li-ion transfer between electrode and ionic liquid electrolyte.

In respect to intercalation-type $Li_4Ti_5O_{12}$ and graphite negative-electrodes when using organic electrolytes, Ogumi and Abe *et al*. have clarified that the desolvation of Li ion is responsible for a large activation barrier for Li-ion transfer at the interface between electrode and electrolyte.[90,91] They concluded that the kinetics of the interfacial Li-ion transfer is influenced by a solvent molecule in an electrolyte solution, and that the activation energy reflects the facility of desolvation of Li ion from the solvent. The activation energies for the interfacial Li-ion transfer between $Li_4Ti_5O_{12}$ electrode and organic electrolyte were reported to be 48.6 kJ mol^{-1} in propylene (PC)-based electrolyte and 44.0 kJ mol^{-1} in ethylene carbonate (EC) + diethyl carbonate (DEC)-based electrolyte.[92] In the light of the above, it is considered that a higher activation energy of interfacial Li-ion transfer is required for an ionic liquid electrolyte due to a strong electrostatic interaction between Li ion and TFSA anions. However, little attention has been given to the interfacial Li-ion transfer in an ionic liquid electrolyte though there were only few reports in which commercial ionic liquids were employed.[63,82] To the best of author's knowledge, there has been no study that tried to examine the influence of functional group attached to cation of ionic liquid on Li-insertion kinetics. In the present study, the author investigated the effect of methoxyethoxymethyl (MEM) group in cation structure on the interfacial Li-ion transfer between electrode and electrolyte using a $Li_4Ti_5O_{12}$ electrode without any binder or conductive additive in terms of reaction kinetics. For the detailed analysis, PP16-TFSA including alkyl-substituted piperidinium cation with same chain length as ether-substituted one was also synthesized and applied to the electrolyte solvent. The author herein discusses the above effect on the basis of the physicochemical properties of the ionic liquids and the solvation environment of Li ions in the electrolyte solutions.

3.2 Experimental Details

Preparation of electrolytes and $Li_4Ti_5O_{12}$ thick-film electrodes

The ionic liquid electrolytes were prepared by dissolving the salt of lithium bis(trifluoromethanesulfonyl)amide (99.9%, LiTFSA) in each one at a concentration of 1.0 mol dm^{-3} (M). For comparison, the author used the organic-based electrolyte of 1.0 M LiTFSA-dissolved in propylene carbonate (Kishida Chemical Co., Ltd.). The preparation of the electrolytes was performed within a purge-type glove box (DBO-2.5LNKP-TS, Miwa MFG) filled with an argon atmosphere from which oxygen and water had been completely removed. The glove box maintained a dew point below −100 °C and an oxygen content below 1 ppm.

$Li_4Ti_5O_{12}$ thick-film electrodes were prepared by a gas-deposition method using a commercial $Li_4Ti_5O_{12}$ powder (99%, Aldrich) with a diameter of *ca*. 100 nm.

Characterization and Electrochemical measurement

The thickness and surface morphology of the deposited $Li_4Ti_5O_{12}$ film on the Cu substrate was investigated through the use of confocal laser scanning microscope (CLSM, VK-9700, Keyence).

The apparent Li-ion transference number (t_{Li+}) was determined by combination measurements consisted of ac impedance and dc polarization using an electrochemical analyzer (CompactStat, Ivium Technologies).[93–95] A symmetric cell of [Li metal | ionic liquid electrolyte | Li metal] was applied for the electrochemical measurement. A polypropylene film having pores with a dimeter of 70−240 nm was soaked in the electrolytes and was used as the separator. The frequency range of the impedance analysis was 100 kHz−100 mHz, and the dc polarization at 10 mV was performed to monitor a steady current for 8 h at 303 K.

To analyze an average solvation number of TFSA anion per Li ion in the ionic liquid electrolytes, Raman spectroscopy system (NanofinderFLEX, Tokyo Instruments, Inc.) with 532 nm line of Nd:YAG laser was used at room temperature. In order to avoid an effect of

water in air, the author put the electrolyte solution into a quartz cell, and tightly sealed in it within an argon atmosphere. The average solvation numbers of PC solvents (N_{PC}) per Li ion was determined by the following equations[91,96,97]:

$$\frac{C_{free}}{C_{solv}} = \frac{I_{free}}{I_{solv}} \cdot \frac{\Gamma^*_{solv}}{\Gamma^*_{free}}$$

$$I_{solv} = -\frac{\Gamma^*_{solv}}{\Gamma^*_{free}} I_{free} + C_{PC,tot}\Gamma^*_{solv}$$

$$N_{PC} = \frac{C_{solv}}{C_{Li,tot}} = \frac{C_{PC,tot}}{C_{Li,tot}(1 + C_{free}/C_{solv})}$$

where Γ^*_{free}* and Γ^*_{solv} denote Raman intensities per unit concentration of the free PC and the PC solvating Li ion, respectively (Total concentration of PC; $C_{PC,tot} = C_{free} + C_{solv}$).

The author fabricated 2032-type coin cells consisting of a $Li_4Ti_5O_{12}$ thick-film electrode as the working electrode, Li foil (99.90%, thickness: 1.0 mm, Rare Metallic) as the counter electrode, electrolyte, and propylene-based separator. The area of the $Li_4Ti_5O_{12}$ film and Li sheet were 0.2 cm^2 and 1.90 cm^2, respectively. To evaluate the effect of cation structure in the ionic liquids on the electrode performance, a rate capability test was carried out using an electrochemical measurement system (HJ-1001 SD8, Hokuto Denko Co., Ltd.) in the potential range between 1.00 and 3.00 V vs. Li/Li^+ at 303 K.

Electrochemical impedance spectroscopic (EIS) analysis using a three-electrode type cell was performed at 1.55 V vs. Li/Li^+ in the frequency range of 100 kHz−100 mHz with an amplitude of 5 mV. The EIS measurement was conducted at various temperatures from 298 to 328 K per 5 K to determine an apparent activation energy of interfacial Li-ion transfer between the $Li_4Ti_5O_{12}$ electrode and the ionic liquid electrolytes. Before the EIS measurement, the

electrode was once cycled and charged (lithiated) up to 1.55 V vs. Li/Li^+ at 0.1 *C* (17.5 mA g^{-1}), and then was kept at the potential for 20 min. Two electrode-type cell was applied only when an activation energy in an organic electrolyte was evaluated.

3.3 Results and Discussion

Characterization of ionic liquid electrolytes

To reveal the effect of cation structure on Li-ion transfer in the ionic-liquid electrolyte bulk, the author evaluated the apparent Li-ion transference number (t_{Li+}) in each of the electrolyte solution by means of combination measurements consisted of ac impedance and dc polarization using a symmetric cell of [Li metal | ionic liquid electrolyte | Li metal] at 303 K. Electrochemical impedance spectroscopic (EIS) analysis for the cell was conducted to measure electrolyte bulk resistances (R_{bulk}) and charge transfer resistances (R_{ct}) at the initial state (Figure 3-1a and 1b). The impedance of the cell was normalized by using the sum of areas of two Li electrodes. In the respective Nyquist plots, one semicircle which denotes R_{ct} was confirmed. The resistance is derived from the interfacial Li-ion transfer between the Li metal and the ionic liquid electrolyte. The values were analyzed using an equivalent circuit shown in Figure 3-1c. Then, a polarization voltage of 10 mV (ΔV) for 8 h was applied to monitor an initial current and a steady-state current. After the steady-state current ($Li \rightleftarrows Li^+ + e^-$) was confirmed (Figure 3-1d), EIS measurement was conducted to determine the t_{Li+} according to the following equation:[93–95]

$$t_{Li+} = \frac{I(\infty)R_{bulk}(\infty)[\Delta V - I(0)R_{ct}(0)]}{I(0)R_{bulk}(0)[\Delta V - I(\infty)R_{ct}(\infty)]} \qquad (1)$$

where $I(0)$ and $I(\infty)$ are the initial state and steady-state currents, respectively. It should be noted that this equation (1) reported by Vincent and Bruce can be applied only to the evaluation

for transference number of a cation with a valence "+1" in an electrolyte bulk.[93] As for ionic liquid electrolytes in which Li ions are inevitably solvated by anions to form negatively charged $[Li(TFSA)_x]^{1-x}$, the determination of transference number of Li ion requires the ratio of self-diffusion coefficient of cation species measured using pulsed-field gradient spin-echo NMR. Therefore, the transference numbers evaluated in the present study is apparent values and have no physical meaning. The author will strictly investigate the transference number in a future study. The apparent transference number and measured values for the parameters are summarized in Table 3-2. The smaller value of R_{bulk} in PP1MEM-TFSA is due to its higher ionic conductivity, and the lower value of R_{ct} indicates a smooth Li-ion transfer at the Li metal and the ionic liquid electrolyte. The calculated t_{Li+} in the respective electrolytes were 0.32 for 1 M LiTFSA/PP1MEM-TFSA and 0.07 for 1 M LiTFSA/PP16-TFSA.

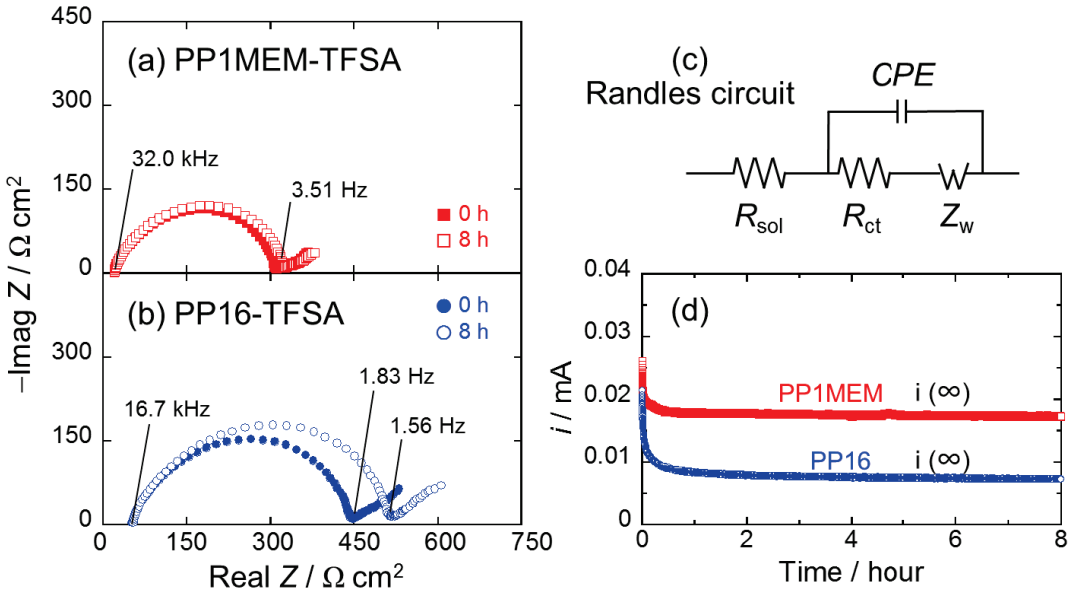

Figure 3-1. Impedance spectra of [Li metal | 1 M LiTFSA/TFSA-based ionic liquid | Li metal] symmetric cells at 303 K. The cation of ionic liquids are (a) PP1MEM and (b) PP16, respectively. Polarization voltage: 10 mV. (c) Randles circuit used in this study for analysis of each cell impedance. (d) Time dependence of dc currents for the symmetric cell at 303 K.

Table 3-1. Summary of measured values for the parameters and transference number of Li^+ (t_{Li+}) obtained from impedance analysis for the [Li metal | 1 M LiTFSA/TFSA-based ionic liquid | Li metal] symmetric cells at 303 K. Polarization voltage:10 mV.

Cation	i_0 (μA)	i_∞ (μA)	$R_{(0)\ \text{bulk}}$ (Ω)	$R_{(\infty)\ \text{bulk}}$ (Ω)	$R_{(0)\ \text{lithium}}$ (Ω)	$R_{(\infty)\ \text{lithium}}$ (Ω)	t_{Li^+}
PP1MEM	26.2	17.3	20.5	21.5	300	312	0.32
PP16	21.4	7.27	54.0	56.0	405	475	0.07

In organic electrolytes generally used for Li-ion batteries, Li-salt ionizes to be stabilized by solvation of solvent molecules to Li ion. On the other hand, because ionic liquids do not contain any neutral molecules, Li ion therefore undergoes coordination from anions of the ionic liquid to stabilize itself.[56–59] Since the counter anion of the ionic liquids used in this study is TFSA anion, Li ions are inevitably solvated by the TFSA anions to form the $[Li(TFSA)_x]^{1-x}$ complexes due to the strong electrostatic interaction generated between the Li ion and the TFSA anions. The symbol "x" denotes the solvation number, which significantly influences on the kinetics of the Li-ion transfer at the electrode−electrolyte interface.[41] For a quantitative evaluation of the solvation number in two kinds of the ionic liquid electrolytes with the different cation structure, Raman spectroscopic measurements to electrolyte solutions of $(LiTFSA)_x(PP1MEM\text{-}TFSA)_{1-x}$ and $(LiTFSA)_x(PP16\text{-}TFSA)_{1-x}$ (x = 0, 0.05, 0.10, 0.15, 0.20) were performed in accordance with the literatures reported by Lassègues or Balducci *et al*.[99,100] Although these spectra appear to be the same in a wide range (Figure 3-2), the PP1MEM-TFSA system is distinctly different from the PP16-TFSA system (Figure 3-3). Figure 3-4 compares Raman spectra of the electrolyte solutions in the wavenumber range from 730 to 760 cm^{-1}.

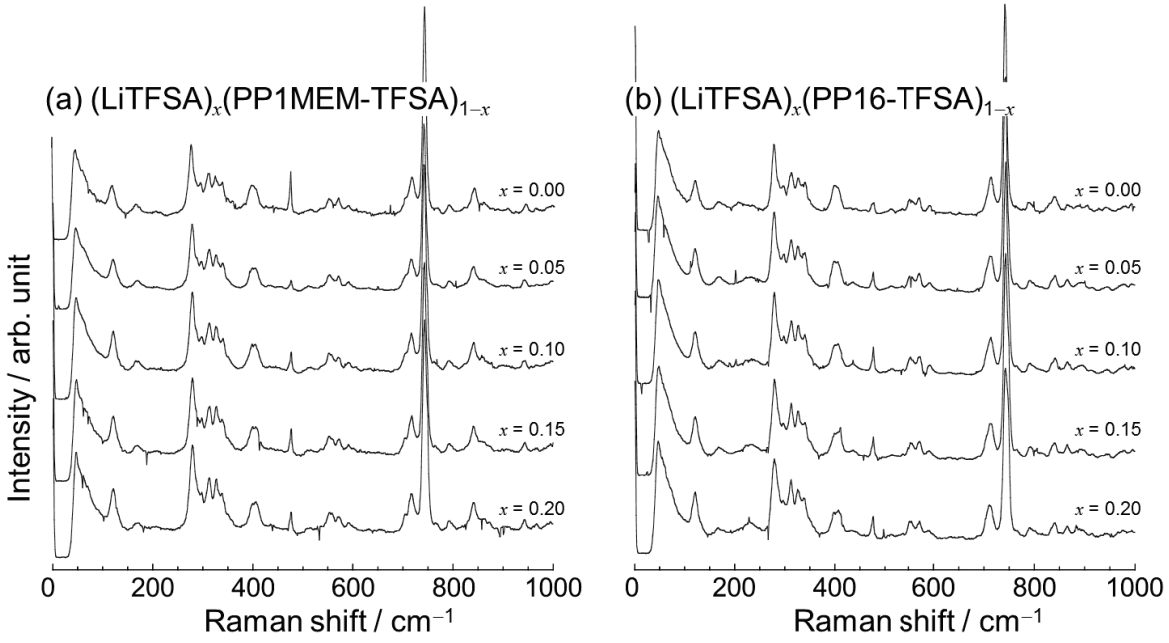

Figure 3-2. Raman spectra of (LiTFSA)$_x$(TFSA-based ionic liquid)$_{1-x}$ and in the frequency range of 0 to 1000 cm^{-1}. The cation of ionic liquids are (a) PP1MEM and (b) PP16, respectively.

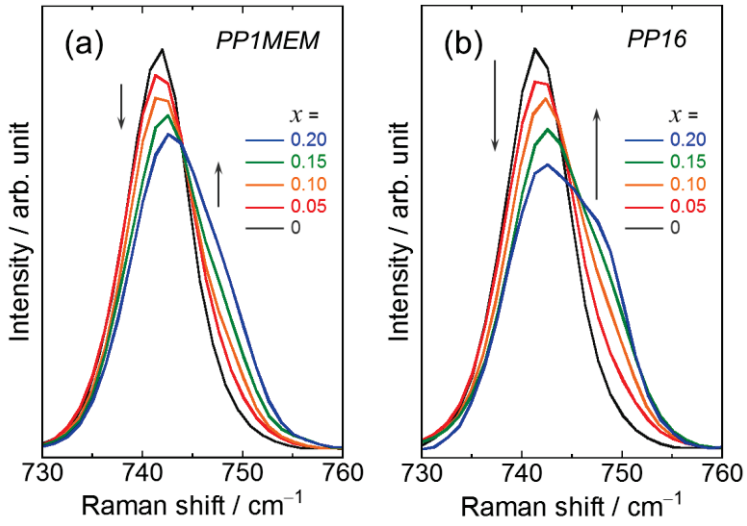

Figure 3-3. Raman spectra of (a) (LiTFSA)$_x$(PP1MEM-TFSA)$_{1-x}$ and (b) (LiTFSA)$_x$(PP16-TFSA)$_{1-x}$ solution in the frequency range of 730 to 760 cm^{-1}. (x = 0, 0.05, 0.10, 0.15, 0.20)

The intense bands located at 742 cm^{-1} in all cases are ascribed to the CF_3 bending vibration coupled with the S−N stretching vibration of the TFSA anion.[57] The band means the existence of *free* TFSA anions ($TFSA^-_{free}$), that is, TFSA anions in the electrolyte solutions do not interact with Li ions and do not behave as a ligand for forming the $[Li(TFSA)_x]^{1-x}$ complex. In other words, the TFSA anions interact with dissociated cations (counter cations) of the respective ionic liquids. On the other hand, the additional band which is observed as a shoulder appeared at around 748 cm^{-1} in the case of presence of LiTFSA-salt (molar fraction: $x \leq 0.05$). This result indicates that Li ions were solvated by the TFSA anions to form the $[Li(TFSA)_x]^{1-x}$ complexes owing to the electrostatic interaction, and the additional band at 748 cm^{-1} here is defined as TFSA anions interacting with Li ion ($TFSA^-_{solv}$). All of the Raman spectra were deconvoluted into the two components including the $TFSA^-_{free}$ and the $TFSA^-_{solv}$ using a Gaussian function. In both the system, the band intensity of $TFSA^-_{free}$ (742 cm^{-1}) decreased with increasing LiTFSA concentration. Contrariwise, the increase in the intensity for $TFSA^-_{solv}$ (748 cm^{-1}) was confirmed as the molar fraction of x is large. Note that the increase ratio of $TFSA^-_{solv}$ in the PP1MEM-TFSA system was smaller than that in the PP16-TFSA system, which shows that the interaction between Li ions and surrounding TFSA anions in the $(LiTFSA)_x(PP1MEM\text{-}TFSA)_{1-x}$ solutions is weaker in comparison to that in the $(LiTFSA)_x(PP16\text{-}TFSA)_{1-x}$ solutions.

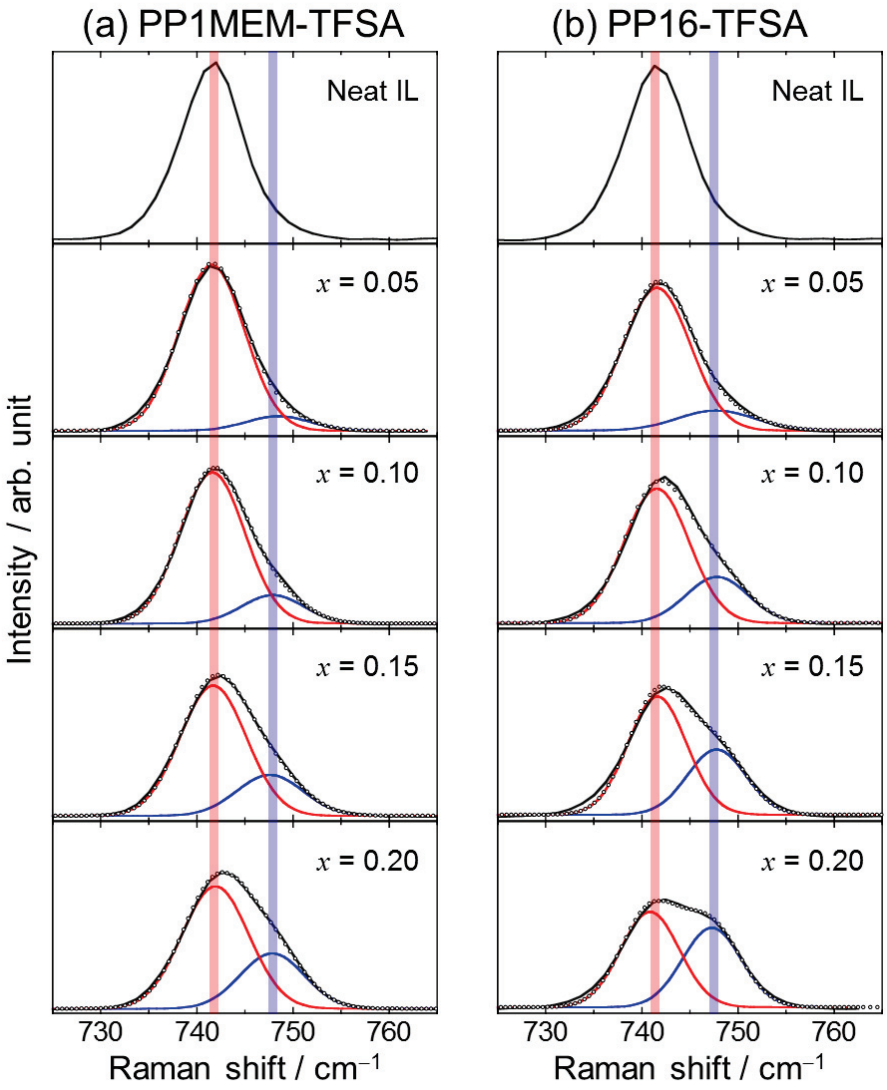

Figure 3-4. Deconvoluted Raman bands of (a) $(LiTFSA)_x(PP1MEM\text{-}TFSA)_{1-x}$ and (b) $(LiTFSA)_x(PP16\text{-}TFSA)_{1-x}$ solutions. The black, dotted, red, and blue lines correspond to the observed spectrum, the total Raman spectrum, the deconvoluted components of *free* TFSA anions ($TFSA^-_{free}$) and TFSA anions interacting with Li^+ ($TFSA^-_{solv}$).

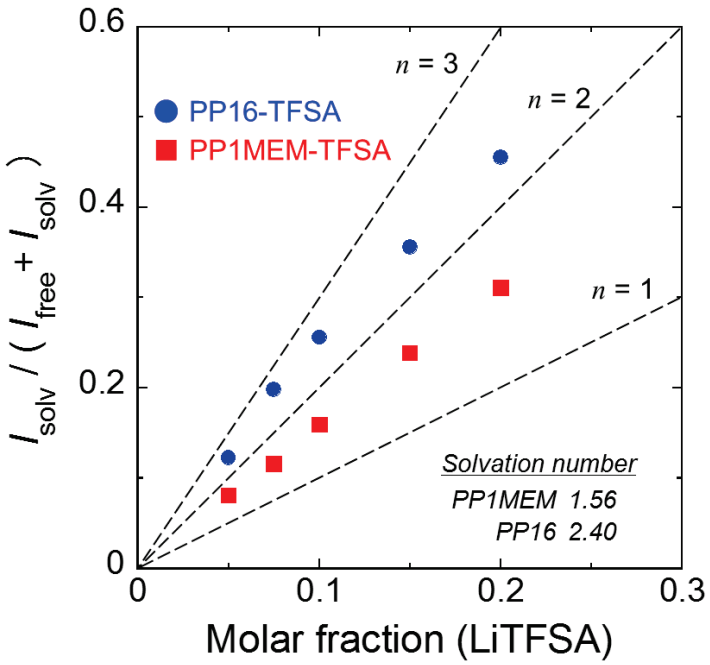

Figure 3-5. Plot of I_{solv} / (I_{free}+ I_{solv}) as a function of x for (LiTFSA)$_x$(PP1MEM-TFSA)$_{1-x}$ and (LiTFSA)$_x$(PP16-TFSA)$_{1-x}$. The dotted lines show slopes in case which an average solvation number (n) of TFSA anion per Li ion is one, two, and three. The average solvation number of TFSA anions is 1.56 for PP1MEM-TFSA system and 2.40 for PP16-TFSA system.

Figure 3-5 depicts plots of $I_{solv}/(I_{free} + I_{solv})$ as a function of molar fraction (x) of LiTFSA for the electrolyte solutions, leading to the determination of an average solvation number of TFSA anions per Li ion.[99,100] The I_{free} and I_{solv} stand for the Raman intensities of $TFSA^-_{free}$ and $TFSA^-_{solv}$, respectively. The slope of dashed line represents to an average solvation number (N_{TFSA} = 1~3) as a guide. Comparing slopes obtained from plots of the respective intensity ratios, it was found that the average solvation number of TFSA anions is 1.56 for the PP1MEM-TFSA system and 2.40 for the PP16-TFSA system. The values given from the Raman measurements clearly show that the solvation environment is greatly affected by the functional group attached with cation of ionic liquid. In the case of using commercially available ionic liquids (*e.g.* PP13-TFSA: *N*-methyl-*N*-propylpiperidinium bis(trifluoromethanesulfonyl)imide

and EMI-TFSA: 1-ethyl-3-methylimidazolium bis(trifluoromethylsulfonyl)imide), the solvation number generally results in "2".[74] It is well known that an ionic liquid having a cation with long alkyl chains behaves as a cationic surfactant and the cation forms an aggregation like a micelle whose hydrophobic parts are arranged inward. Kunze *et al*. studied the aggregation behavior of pyrrolidinium-based ionic liquids (Py1*x*, *x* = 3~8) with TFSA anion by means of NMR relaxation and Raman spectroscopic measurements. The difference calculated by subtracting spin-lattice relaxation rate from spin-spin relaxation rate in the ionic liquids became larger than 0 when the side chain length is longer than three (propyl), which indicates that the Py1*x* (x = 4~8) cations tend to aggregate. Additionally, in Raman spectra with the presence of LiTFSA-salt, the band intensity associated with the interaction between Li ion and TFSA anions increased and the solvation number grew with increasing side chain length. This is because the aggregation degree of Py1*x* cations gradually enlarged.[74] In view of the aggregation effect, it is suggested that the interaction between PP16 cations and TFSA anions weakened. Thereby allows Li ions to be strongly trapped by the TFSA anions. This is probably considered as the reason why the average solvation number in the PP16-TFSA system became larger than that in the PP1MEM-TFSA system. By contrast, the PP1MEM cation has two negatively-charged oxygen atoms as an ether functional group (methoxyethoxymethyl) in its structure. It is inferred from the characteristics that the functional group has the ability of attracting Li ions through its lone-pair electrons.

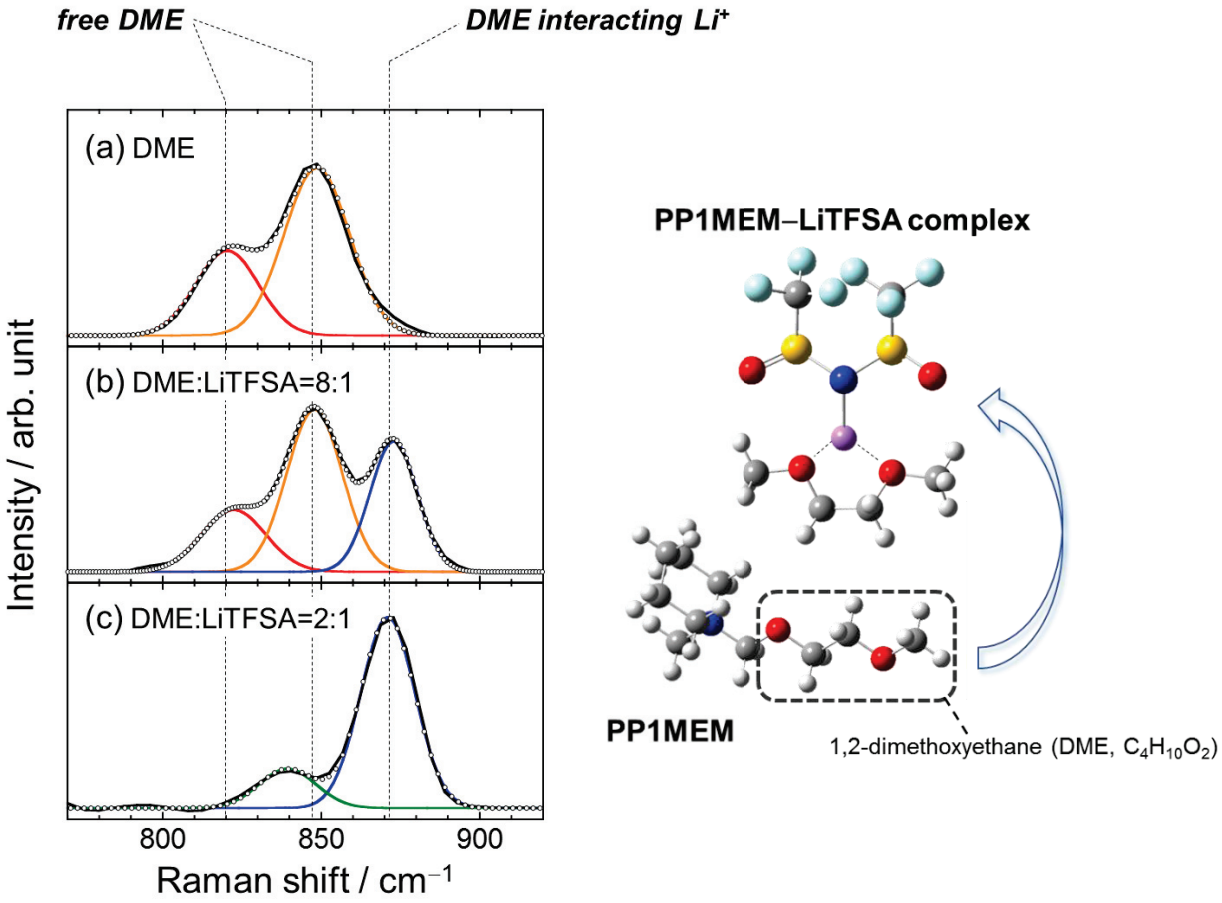

Figure 3-6. Raman spectra of (a) pure DME solvent and DME−LiTFSA solutions. The molar ratios of DME to LiTFSA are (b) 8:1 and (c) 2:1, respectively. Schematic illustration of proposed structure of PP1MEM−LiTFSA complex based on the results of the Raman measurements is shown.

For example, an organic solvent of 1,2-dimethoxyethane (DME; $C_4H_{10}O_2$), same molecular frame as the methoxyethoxymethyl group, forms a $[Li(DME)_2]^+$ complex with Li ion via the two oxygen atoms at a certain molar ratio (Figure 3-6). In the case of the ionic liquid electrolyte, however, the phenomenon which the oxygen atoms in the functional group attract only Li-ion is unlikely in light of a repulsive force between positive Li ion and positively-charged PP1MEM cation. Tsuzuki *et al*. reported the following on the basis of ab initio molecular

calculations: *N*,*N*-diethyl-*N*-methyl-*N*-(2-methoxyethyl)ammonium (DEME) cation with an electron withdrawing group forms a stable complex with LiTFSA complex rather than Li cation. The TFSA anion in the LiTFSA complex plays a key role to screen the repulsive interaction between Li caion and DEME cation.[76] The author also searched a signature of interaction between Li ion and ether moiety of PP1MEM from Raman spectra of the $(LiTFSA)_x(PP1MEM\text{-}TFSA)_{1-x}$ solutions ($x = 0$, 0.10 and 0.20). Figure 3-7 displays the Raman spectra in the range of 1260 to 1300 cm^{-1} (fingerprint region). Neat PP1MEM-TFSA showed the asymmetric stretching ν(C−O−C) vibration coupled with C−H vibration at 1271 cm^{-1}. When LiTFSA was added to the pure ionic liquid with a molar fraction of 0.10, the band intensity was relatively reduced, and the additional band was appeared in a high wavenumber side of 1277 cm^{-1}. A band associated with molecular solvents typically shifts to high wavenumber side upon binding of the solvent molecules to metal ions. It is inferred that the ether side chain of PP1MEM cation became rigid by the interaction of the ether moiety with Li ion (coordination of Li ion into the ether moiety). This is probably the reason for the reduced band intensity (1271 cm^{-1}) and the appearance of the new band (1277 cm^{-1}). At a further addition of LiTFSA (x = 0.25), however, a band located at 1275 cm^{-1} also observed. It is expected that the configuration of PP1MEM cation surrounded by TFSA anions is very complicated, so that what the band means is still unclear. As one hypothesis, the author guesses that the band indicates the stabilization of PP1MEM-LiTFSA at a certain molar fraction. In a future study, the author will investigate what the bands show by computational chemistry support. Allowing for the results, it is considered that the PP1MEM cation attracts Li-ion binding with TFSA anion through the two oxygen atoms in its ether side chain to form PP1MEM-LiTFSA complex. As a result of the attractive force induced by the negatively-charged oxygen atoms in the PP1MEM cation, the average solvation number of TFSA anions in the PP1MEM-TFSA system appears to be less than two and smaller than that in the PP16-

TFSA system. The fact that the solvation number becomes smaller means that Li ions in PP1MEM-TFSA are relatively free from the constraint generated by the electrostatic interaction.

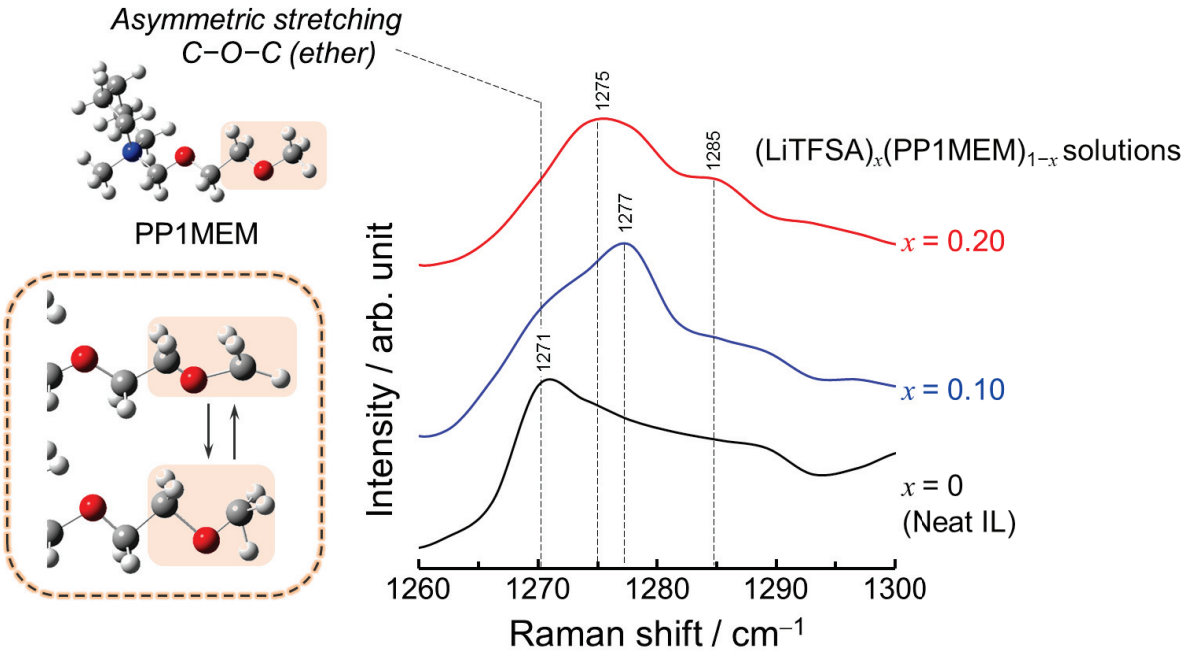

Figure 3-7. Raman spectra of $(LiTFSA)_x(PP1MEM\text{-}TFSA)_{1-x}$ (x = 0, 0.10 and 0.20) in the frequency range of 1260 to 1300 cm^{-1} (finger region). The electrolyte solutions were put into a quartz cell, and tightly sealed in it within an argon atmosphere to avoid an effect of water in air.

Effect of cation structure on Li-insertion/extraction property of $Li_4Ti_5O_{12}$ electrode

Figure 3-8a and 8b show XRD pattern and Raman spectrum of the film prepared by gas-deposition using a $Li_4Ti_5O_{12}$ powder (inset image) on a Cu substrate. All of the peaks with the exception of the Cu current collector are attributed to lithium titanium oxide ($Li[Li_{1/3}Ti_{5/3}]O_4$) with a spinel framework structure ($Fd\bar{3}m$ space group).[85] Sharp peaks located at 233, 434, and 670 cm^{-1} in the Raman spectrum are assigned to the vibrations of crystalline lattice of $Li_4Ti_5O_{12}$

such as F_{2g}, E_g, and A_{1g} phonon modes.[87] Results obtained from the XRD and Raman measurements indicate that the film prepared by gas-deposition was composed of pure $Li_4Ti_5O_{12}$ without any impurity, and that its composition was unchanged during the film formation. Figure 3-8c displays an optical image of the $Li_4Ti_5O_{12}$ electrode and a three-dimensional height profile analyzed by CLSM. The difference in the level between the substrate and the film formed by using a mask was *ca*. 36 μm, which corresponds to the thickness of the deposited active-material layer. The author successfully obtained the $Li_4Ti_5O_{12}$ thick-film electrode with a thickness of several tens of micro-meters which does not contain any binder or conductive additive. It is thus possible to directly observe electrochemical reactions at the interface between the $Li_4Ti_5O_{12}$ and the ionic liquid electrolytes.

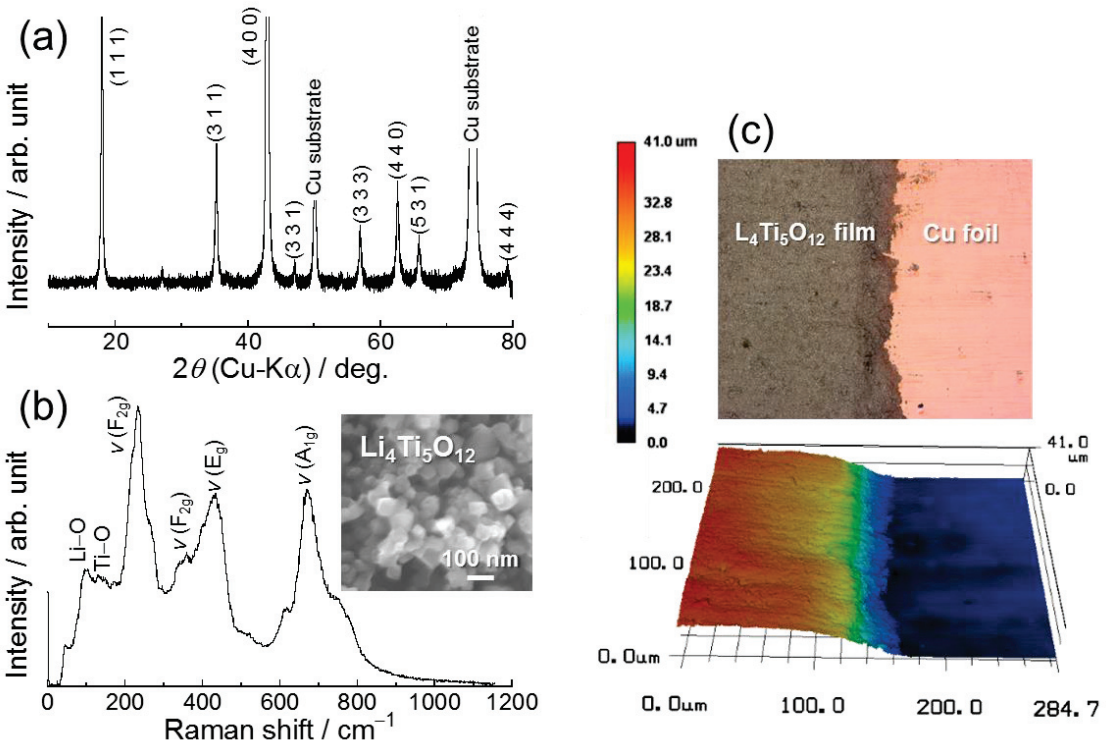

Figure 3-8. (a) XRD pattern and (b) Raman spectrum of $Li_4Ti_5O_{12}$ thick-film electrode prepared by a gas-deposition method. FE-SEM image of $Li_4Ti_5O_{12}$ powder used in this study is inserted. (c) Optical image of the $Li_4Ti_5O_{12}$ electrode and three-dimensional height profile analyzed by a confocal scanning laser microscope. The deposited film thickness is *ca*. 36 μm.

For exploring the benefits granted by the less solvation number of TFSA anions to Li ion, galvanostatic charge−discharge tests were conducted. Figure 3-9 represents rate capabilities of the electrodes in the piperidinium-based ionic liquid electrolytes at various *C*-rates from 0.1 *C* (17.5 mA g^{-1}) to 20 *C* (3500 mA g^{-1}). In the rate performance tests from 0.1 *C* to 20 *C*, both charge and discharge were conducted at the same current densities, and the geometric current density of 1.0 *C*-rate corresponds to 0.13 mA cm^{-2}. For comparison, the performance in an organic electrolyte using PC was also shown. At the low current density (*e.g.* 0.1 *C* and 0.2 *C*), PP1MEM-TFSA delivered a high discharge (Li-extraction) capacity than 170 mA h g^{-1}, which is comparable to that in the organic electrolyte. The notable point is that the $Li_4Ti_5O_{12}$ electrode in PP1MEM-TSFA exhibited the larger capacities than those in PP16-TFSA even at the low *C*-rates where an influence of concentration polarization on charge−discharge property is reduced. The result indicates that the Li-insertion/extraction capacities in the ionic liquid electrolytes are greatly affected by the solvation environment of Li ion in the respective electrolytes. When the current density was raised from 0.2 *C* to 0.5 *C*, the reversible capacity in PP16-TFSA dropped down from 143 mA h g^{-1} to 82 mA h g^{-1} with a retention of 57%. Then, the clear polarizations for charge−discharge processes appeared in the electrolytes (Figure 3-10).

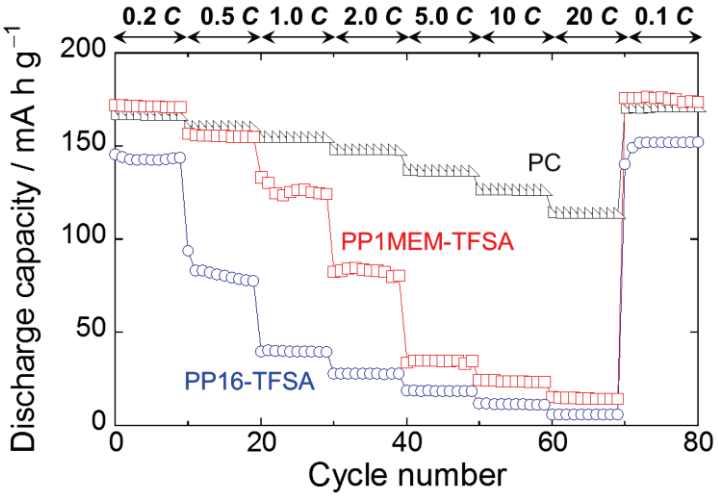

Figure 3-9. Rate capability of $Li_4Ti_5O_{12}$ thick-film electrodes in piperidinium-based ionic liquid electrolytes at various *C*-rates from 0.1 *C* (17.5 mA g^{-1}) to 20 *C* (3500 mA g^{-1}). For comparison, the performance in the organic electrolyte of 1 M LiTFSA/PC is also plotted.

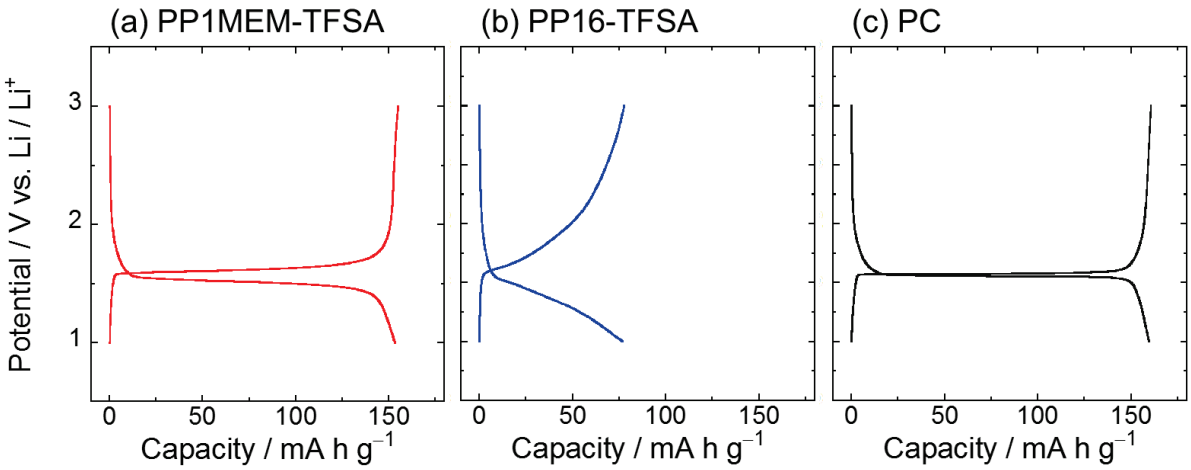

Figure 3-10. Charge-discharge profiles of $Li_4Ti_5O_{12}$ thick-film electrodes at 0.5 *C* rate in ionic liquid electrolyte of (a) PP1MEM-TFSA, (b) PP16-TFSA, and (c) organic electrolyte of PC.

At a high rate in which mass transport of Li ion dominates an electrochemical reaction, the charge−discharge reaction rate are controlled by Li-ion diffusion in the electrolyte solution. The poor rate performance in PP16-TFSA is presumably due to both the slow kinetics of interfacial Li-ion transfer and the low Li-ion diffusion derived from the ionic liquid electrolyte. Whereas, the electrode in PP1MEM-TFSA yield a 90% capacity of the first capacity at 0.5 *C*, and only a capacity of 16 mA h g^{-1} was decreased. Furthermore, the superiority observed in PP1MEM-TFSA became marked at a relatively high rate, as the author expected; a capacity of 125 mA h g^{-1} equivalent to more than the triple of the capacity in PP16-TFSA was attained at 1.0 *C*. Li-insertion reaction into a $Li_4Ti_5O_{12}$ electrode in an ionic liquid electrolyte takes place after the following elementary steps: (i) Li-ion (solvated by TFSA anions) migration/diffusion in the electrolyte bulk, (ii) desolvation of $[Li(TFSA)_x]^{1-x}$ and Li-ion transport across the inner Helmholtz plane formed by a cation accumulation at the interface between the electrode and the ionic liquid electrolyte. Because of the strong electrostatic interaction between Li ion and TFSA anions[83], the diffusion in the electrolyte bulk and the reaction for desolvation of the

TFSA anions from the Li ion becomes slow. These phenomena limit charge−discharge capacities. As the author described above, the average solvation numbers of TFSA anions are 1.56 for the PP1MEM-TFSA system and 2.40 for the PP16-TFSA system. Given the correlation between the solvation number and the rate capabilities, the author assumed that either the Li-ion diffusion in the electrolyte bulk or the kinetics of interfacial Li-ion transfer depends on the solvation environment of Li ions such as the solvation number of TFSA anions.

The EIS analyses were carried out for the $Li_4Ti_5O_{12}$ electrodes in the ionic liquid electrolytes with different cation structure to discuss which factor affects charge−discharge rate performance by investigating an activation energy of the interfacial Li-ion transfer. Figure 3-11a depicts a typical Nyquist plot of a negative electrode at the charge (Li-inserted) state with little influence of a surface layer, and the Nyquist plot composed of one semicircles in a high frequency and a straight line with a slope of approximately 45° in a low frequency region. In general, these components are interpreted as following: the first semicircle (R_{ct}) originates from the interfacial Li-ion transfer processes which includes the desolvation of $[Li(TFSA)_x]^{1-x}$, the Li-ion transport in an electrical double layer and/or a surface layer induced by decomposition of electrolyte. The straight line in the low frequency is derived from the solid-state diffusion of Li (Z_w). At the Nyquist plots in the PP1MEM-TFSA and PP16-TFSA systems (Figure 3-11b), the author could observe the components mentioned above. The each resistance was analyzed using the equivalent circuit shown in Figure 3-11a. The constant phase element (CPE) was employed in place of capacitance (C) for taking into account the roughness of the electrode surface. To examine the kinetics of the Li-insertion reactions in the respective electrolytes, the author monitored the temperature dependence of the interfacial Li-ion transfer resistance in the range from 298 K to 333 K.[92] The author confirmed that the resistances obviously decreased with increasing temperature. In addition to this, the inverse of the resistances as a function of

reciprocal temperature showed Arrhenius-type behavior (Figure 3-11c). The inverse of the resistances (interfacial conductivities) obeys the Arrhenius-type equation:

$$\frac{1}{R_{ct}} = A\exp(-\frac{E_a}{RT}) \qquad (2)$$

where the symbol A, E_a, R and T denote frequency factor, activation energy, gas constant, and absolute temperature, respectively. The apparent activation energy for the interfacial Li-ion transfer can be determined by the slope of the Arrhenius plots.[91]

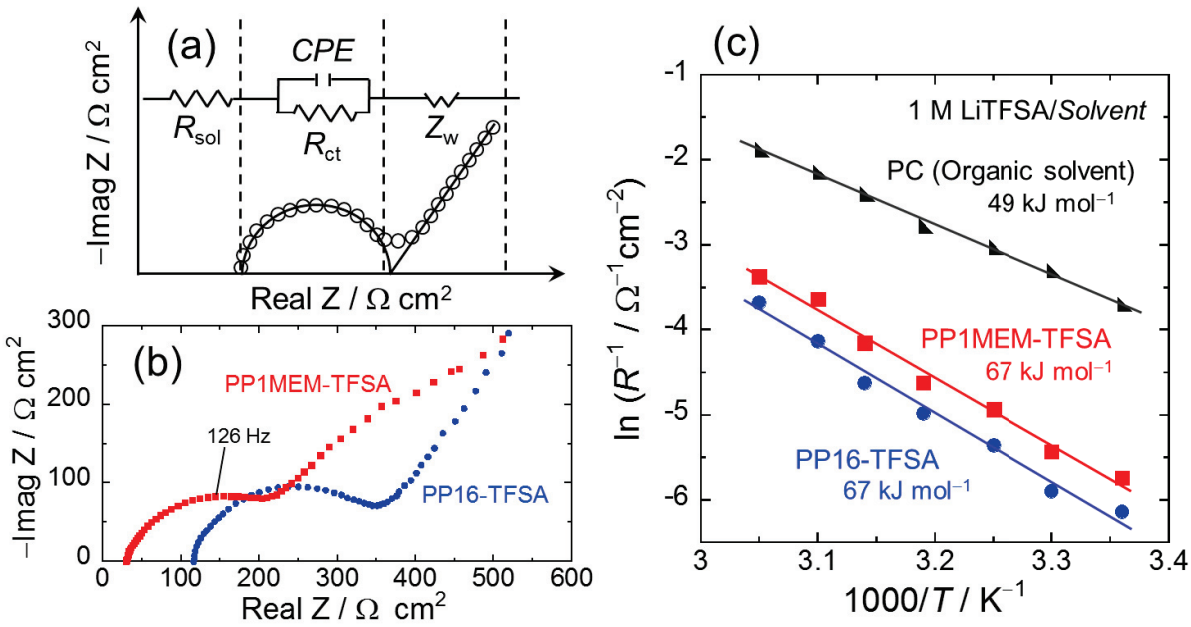

Figure 3-11. (a) Typical Nyquist plot and the result of fitting by equivalent circuits for impedance analysis. (b) Nyquist plots of $Li_4Ti_5O_{12}$ thick-film electrodes charged at 1.55 V vs. Li/Li^+ the first cycle in PP1MEM-TFSA and PP16-TFSA at 303 K. (c) Temperature dependence of interfacial resistance of the electrodes in the electrolyte of 1 M LiTFSA-dissolved in PP1MEM-TFSA, PP16-TFSA and PC. Activation energies were obtained from the slope.

Abe *et al*. reported that the activation energy for the interfacial Li-ion transfer between $Li_4Ti_5O_{12}$ thin film and ionic liquid electrolyte showed about 70 kJ mol^{-1} without depending on cation species.[82] On the other hand, in the other literature, they demonstrated that the activation energy estimated from Li-ion transfer at the lanthanum lithium titanate (LLT)/ionic liquid electrolyte interface using a four-electrode electrochemical cell was different with cation species consisting ionic liquids.[81] For example, the activation energy at the LLT/EMI-TFSA interface is lower than that at LLT/PP13-TFSA by 10 kJ mol^{-1}, and they described the reason that the interaction between Li ion and TFSA anion is more weakened by cation-anion interaction of imidazolium-based ionic liquid than by that of piperidinium-based ionic liquid. From this points, it is no wonder that the activation energy obtained from the $Li_4Ti_5O_{12}$ electrode/PP1MEM-TFSA interface is smaller than that from the $Li_4Ti_5O_{12}$ electrode/PP16-TFSA interface. Contrary to our expectation, the activation energy calculated from the R_{ct} was same degree of 67 kJ mol^{-1} and agreed with the value reported by Abe *et al*.[82] By assuming that the desolvation of TFSA anions from Li ion progresses in a stepwise fashion, and the influence of earlier desolvation on the kinetics of the interfacial Li-ion transfer is relatively small and the last desolvation is dominant, the phenomenon which the activation energy remained unchanged can be explained. On the other hand, the solvation number of PC molecules per Li ion was about 3.8 (Figure 3-12); nevertheless the activation energy obtained from the organic electrolyte of 1 M LiTFSA-dissolved in PC resulted in the most smallest value of 49 kJ mol^{-1} among the three kind of electrolytes and gave close agreement with the value reported by Doi *et al*.[92] These experimental results again remind us that the interaction between Li ion and TFSA anions is much higher than that between Li ion and molecular solvents in the organic electrolyte, and the electrostatic interaction generated in the ionic liquid electrolytes is responsible for the slow kinetics of the interfacial Li-ion transfer. From the Raman analysis, it was revealed that the solvation numbers of TFSA anions per Li ion were 1.56 for PP1MEM-

TFSA and 2.40 for PP16-TFSA, which indicate that Li ions in PP1MEM-TFSA are relatively free from the constraint generated by the electrostatic interaction, and transport ability of the Li-ion in PP1MEM-TFSA was enhanced. Based on the results, the author inferred that the reason for the improved rate performance in PP1MEM-TFSA is derived from the Li-ion diffusion in the electrolyte rather than from the kinetics of the interfacial Li-ion transfer at electrode−electrolyte.[62] What these examples makes clear is that the PP1MEM cation played a key role of enhancement for Li-ion diffusion in the electrolyte bulk. An optimization of not only the cation but also anion would realize Li-ion batteries with a high energy density and a high safety.

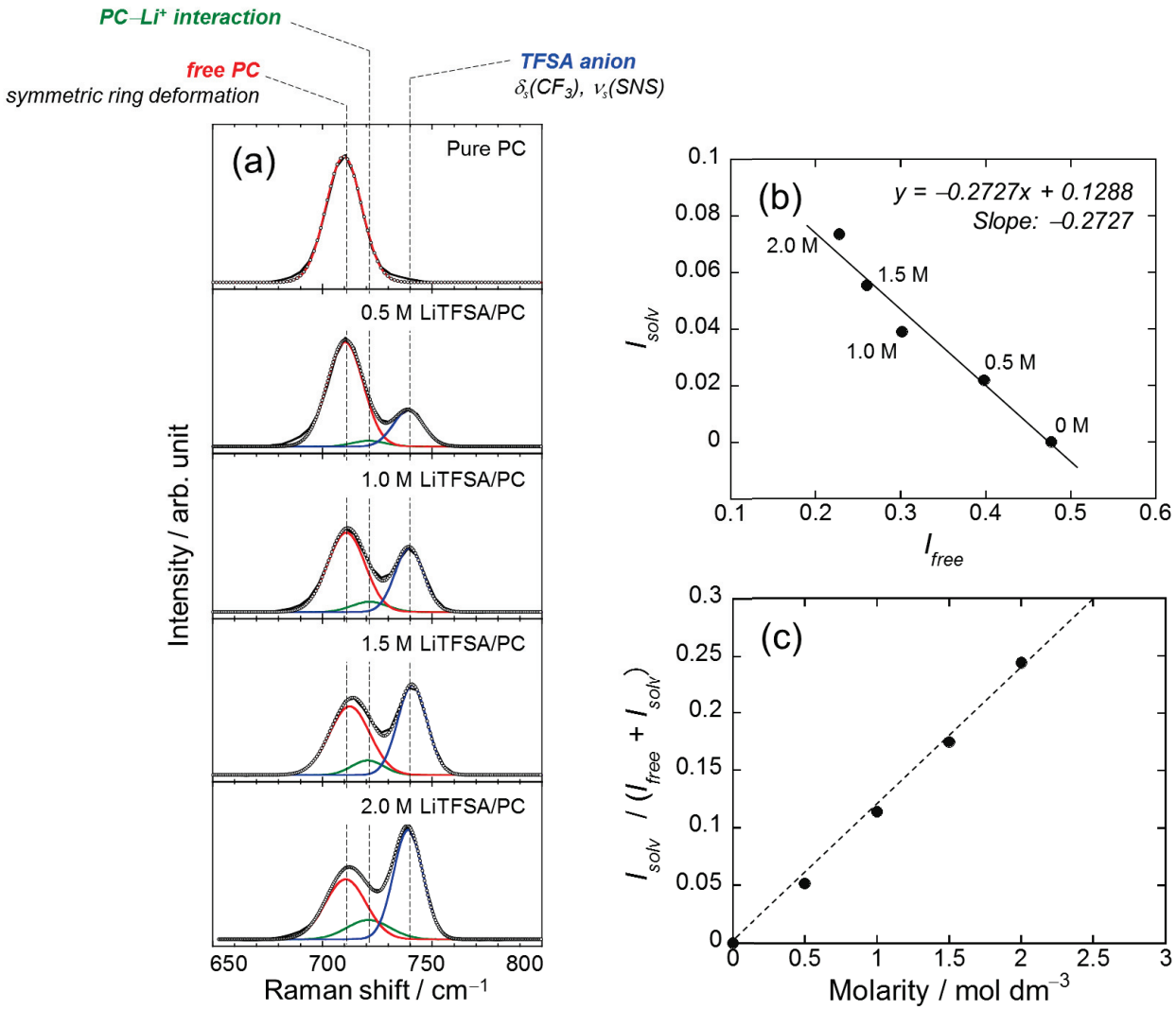

Figure 3-12. (a) Raman spectra of pure propylene carbonate (PC) solvent and electrolytes consisted of LiTFSA and PC with various concentration (0.5, 1.0, 1.5, 2.0 M). (b) Relation between the intensities of free PC (I_{free}) and PC solvating Li^+ (I_{solv}) in the 0.5−2.0 M LiTFSA/PC electrolytes. (c) Plot of I_{solv} / (I_{solv}+ I_{free}) versus molarity of LiTFSA. The bands at 710 cm^{-1} and 739 cm^{-1} is assigned to the symmetric deformation mode of "*free*" PC molecules and CF_3 bending vibration δ_s (CF_3) coupled with the S−N stretching vibration ν_s (S−N−S) of TFSA anions, respectively. By dissolution of LiTFSA-salt in PC solvent, the new band appears at 721 cm^{-1}, which is attributed to the PC solvating Li ion.

3.4 Summary

The transport ability and solvation environment for Li ion in piperidinium-based ionic liquid electrolytes were investigated by EIS technique and Raman spectroscopic measurements. In addition, the effect of cation structure of ionic liquid on the kinetics of interfacial Li-ion transfer between electrode and electrolyte was studied using a $Li_4Ti_5O_{12}$ thick-film prepared by gas-deposition without any binder or conductive additive. The apparent transference numbers of Li ion in PP1MEM-TFSA and PP16-TFSA were 0.32 and 0.07, respectively. Raman analysis of the electrolyte solutions revealed the following: the PP1MEM cation weakens the interaction between Li ion and TFSA anions, and thereby diminishes the solvation number of TFSA anions (N_{TFSA} 1.56) compared with that in PP16-TFSA (N_{TFSA} 2.40). When the current density was increased from 0.2 *C* to 1.0 *C*, the discharge capacity of $Li_4Ti_5O_{12}$ electrode in PP16-TFSA drastically dropped, and the electrode showed the capacity of only 40 mA h g^{-1}. On the other hand, the less solvation number in PP1MEM-TFSA enhanced the rate performance (125 mA h g^{-1} at 1.0 *C*). From the EIS measurements, it was found that the apparent activation energy associated with the interfacial Li-ion transfer showed same degree of 67 kJ mol^{-1} without depending on the cation species. This result indicates that the reason for the improved rate performance in PP1MEM-TFSA originates from not the kinetics of the interfacial Li-ion transfer at electrode−electrolyte but from the enhanced Li-ion diffusion in the electrolyte bulk.

Chapter 4

Analysis of Mechanism of Improved Cycle Performance of Si Negative-Electrode in Ionic Liquid Electrolyte Using Raman Microspectroscopy

4.1 Introduction

In chapter 2, the author also demonstrated that the cycle stability of a Si electrode was remarkably improved by using the ionic liquid of 1-((2-methoxyethoxy)methyl)-1-methylpiperidinium bis(trifluoromethylsulfonyl) amide (PP1MEM-TFSA).[83] PP1MEM-TFSA delivered a comparatively high capacity of 1050 mA h g^{-1} even at the 100th cycle, whereas the capacity in an organic electrolyte of 1.0 M LiTFSA-dissolved in propylene carbonate (PC) drastically decreased to 110 mA h g^{-1}. Song *et al*. prepared $SiO_{1.3}$ film on a stainless steel substrate by pulse laser deposition, and studied its anode property in an ionic liquid electrolyte composed of lithium bis(trifluoromethanesulfonyl)amide (LiTFSA) and *N*-methyl-*N*-methylpyrrolidinium bis(trifluoromethanesulfonyl)amide (Py13-TFSA).[77] The $SiO_{1.3}$ electrode in the ionic liquid electrolyte achieved a reversible capacity of 930 mA h g^{-1} at the 200th cycle with a good capacity retention of 88% whereas the capacity in an organic electrolyte of 1.0 M lithium hexafluorophosphate ($LiPF_6$)-dissolved in the mixture of ethylene carbonate (EC) and diethyl carbonate (DEC) had rapidly faded by the initial 50th cycle. They investigated the characteristics of the surface layers formed on their anodes after cycling, and concluded the reason for its higher cycle performance obtained from Py13-TFSA is that the surface layer covering the $SiO_{1.3}$ electrode is stable and thinner than that in the organic electrolyte.[101]

As is well known, during the first charge (Li-insertion) process, electrolytes based on organic solvents are generally decomposed to form a surface layer consisting of organic and inorganic compounds on a negative electrode.[102,103] Additionally, in the case of using Si-based electrodes, drastic volume changes accompany Li−Si alloying and dealloying reactions, which generates cracks on the electrode surface and a partial breakup of the Si electrode.[104] This

causes damage to the surface layer and thereby exposes a new surface of the negative electrode, and as a result, a renewed surface layer is reconstructed by decomposition of the electrolyte. The continuous formation of the surface layer makes itself thicker, which leads to an increase in the resistance for Li-insertion into the Si.[105] For these reasons, the Si electrode is partially passivated, and intact (unreacted) regions remain after cycling. In other words, the utilization of the active material becomes lower, which is one of the causes that reduces the cycling performance of Si electrode in organic electrolyte systems. In contrast, it is reported that ionic liquid-derived surface layers are stable and thinner.[77,101] Meanwhile, the reason why Si electrodes exhibit better cycling performances in ionic liquid electrolyte of 1.0 M LiTFSA/PP1MEM-TFSA is still unclear. Understanding this phenomenon will contribute to the development of high-performance electrode materials and electrolytes.

Raman spectroscopy is a powerful tool for identifying the crystallinity of an active material. Crystalline Si (*c*-Si) electrochemically reacts with Li to form *c*-$Li_{15}Si_4$ phase at room temperature.[1,2] The *c*-Si then undergoes amorphization after the Li-extraction process to transform into amorphous Si (*a*-Si), when the band position of 520 cm^{-1} in a Raman spectrum showing *c*-Si typically shifts to 490 cm^{-1} indicating *a*-Si.[106–108] By taking advantage of this nature obtained by the Raman scattering, Si that reacted with Li can be distinguished from unreacted Si, which enables us to clarify the Li-insertion distribution in Si electrode surface. A gas-deposition method is a suitable technique to form thick films, and does not require any binder and conductive additive to prepare thick-film electrodes. The advantages of this method are as follows: (1) the strong adhesion between the active material particles as well as between the particles and the substrate, and (2) the nearly unchanged composition in a thick film formed without atomization (e.g., vaporization) of the particles.[65] It is thus possible to directly observe an electrochemical reaction between pure Si and electrolytes. This is first report that addresses

the elucidation of deterioration mechanism for Si electrode by Raman imaging analysis to the best of the author's knowledge.

In this chapter, the author investigated the origin of the improved cycling performance of the Si electrode in the ionic liquid electrolyte using PP1MEM-TFSA by analyzing the deterioration mechanisms for Si electrodes in organic and ionic liquid electrolytes from the viewpoint of the Li-insertion distributions.

4.2 Experimental Details

Preparation of Si thick-film electrodes

Si thick-film electrodes were prepared by a gas-deposition method using a commercial Si powder (99.9%, Wako Pure Chemical Industries, Ltd.) and an argon carrier gas (chapter 1).

Characterization of Si thick-film electrodes and Electrochemical measurement

The crystal structure of the film deposited on the Cu substrate was identified by X-ray diffraction (XRD, Ultima IV, Rigaku) and Raman microscopy (NanofinderFLEX, Tokyo Instruments, Inc.) with 532 nm line of Nd:YAG laser at room temperature. The thickness of the Si film prepared by gas-deposition was investigated through the use of a confocal laser scanning microscope (CLSM, VK-9700, Keyence). The difference in the level between the substrate and Si film formed by using a mask was measured by laser scanning.

The author fabricated 2032-type coin cells consisted of a Si thick-film electrode as the working electrode, Li foil (Rare Metallic, 99.90%, thickness: 1.0 mm) as the counter electrode, electrolyte, and propylene-based separator. The areas of the Si thick-film and Li sheet in the cell are 0.5 cm^2 and 1.90 cm^2, respectively. Galvanostatic charge−discharge tests were carried out using an electrochemical measurement system (HJ-1001 SM8A, Hokuto Denko Co., Ltd.) in the potential range between 0.005 and 2.000 V vs. Li/Li^+ at 303 K. The current density was set to be 420 mA g^{-1}, corresponding to a *C*-rate of 0.12 *C*. Cyclic voltammetry measurement

was conducted at a sweep rate of 0.1 mV s^{-1} to investigate the electrochemical behavior of the Si thick-film electrode as Li-ion battery anode.

The surface morphologies of the Si thick-film electrodes after cycling were observed by a field-emission scanning electron microscope (FE-SEM, JSM-6701F JEOL Co., Ltd.).

Analysis of two-dimensional Li-insertion distribution on Si electrode surface

To visualize the regions in which the Si reacted with Li in the electrodes after cycling in the organic and ionic liquid electrolytes, Raman mapping analyses were conducted. After the 10th charge−discharge cycle, the Si thick-film electrodes were separated from coin cell and washed with dimethyl carbonate (DMC; Kishida Chemical Co., Ltd.) for removal of the residual electrolyte followed by drying in the glove box at room temperature. The mapping area was 7 × 7 μm^2, and the Raman spectra of 400 points (20-by-20 points) were recorded. Surface Raman images were then made by plotting of the band position with the maximum intensity in the frequency range from 490 to 520 cm^{-1}. For comparison, Raman microscopic measurement with respect to the Si thick-film electrode before cycling was also performed.

4.3 Results and Discussion

To identify the phase of the Si film formed on the Cu substrate prepared by gas-deposition, XRD measurement and Raman spectroscopic analysis were conducted. Crystalline Si with cubic structure (Inorganic Crystal Structure Database, ICSD No. 00-027-1402) was detected by XRD as shown in Figure 4-1a. The peak located in 520 cm^{-1} on the Raman spectrum indicates phonon band in bulk Si corresponding to the presence of crystalline Si (Figure 4-1b), which agrees with our results of XRD measurement and Raman spectra reported by other researchers.[106−108] It was established that the film prepared by gas-deposition is composed of pure crystalline Si without any impurity. The author can directly observe the electrochemical reactions between the Si electrode and electrolyte since the electrode does not contain any

binder and conductive additive. Figure 4-2 shows a photograph of the Si thick-film electrode and a cross-sectional height profile in the distance from A to B in the photograph, corresponding to the thickness of the deposited Si film on the Cu substrate. Observation by a confocal laser scanning microscope revealed that the thickness of the Si film is *ca*. 2.3 μm.

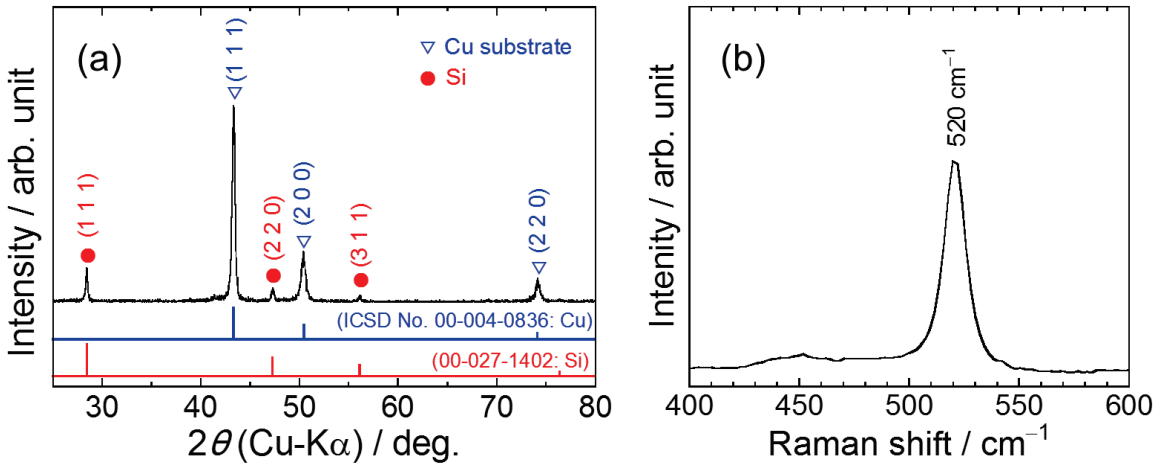

Figure 4-1. (a) XRD pattern and (b) Raman spectrum of Si thick-film electrode prepared by gas-deposition.

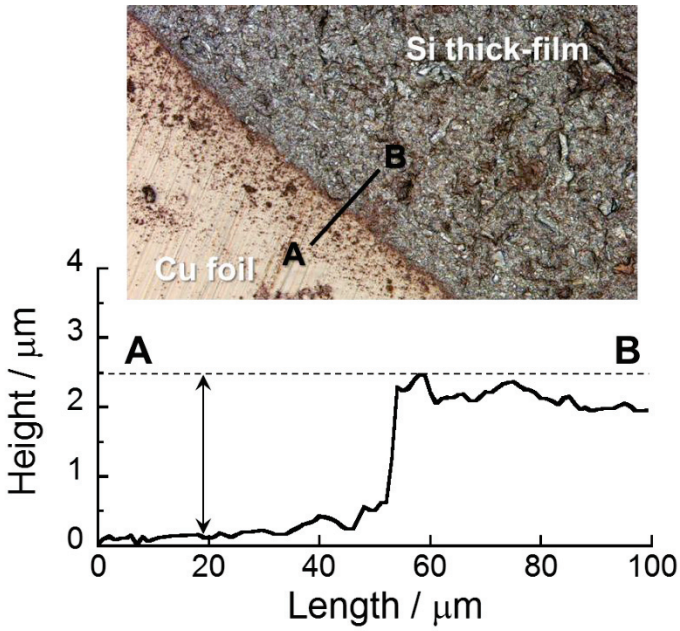

Figure 4-2. (upper) CLSM image of Si thick-film prepared by a gas-deposition method using commercial Si powder and Ar carrier gas. (lower) Height profile in the distance from A to B, corresponding to the thickness of the Si film deposited on the Cu foil.

Figure 4-3a compares initial charge−discharge (Li insertion−extraction) curves of the Si thick-film electrodes in 1.0 M LiTFSA-dissolved in PC and PP1MEM-TFSA. In every case, potential plateaus were observed at around 0.1 and 0.4 V vs. Li/Li^+ on the charge and discharge curves, which indicates alloying and dealloying reactions of Si with Li. For the organic electrolyte using PC, the first charge and discharge capacities were 3640 and 3040 mA h g^{-1}, respectively, with the first coulombic efficiency of 84%. On the other hand, the Si electrode in the ionic liquid electrolyte showed the initial discharge capacity of 2670 mA h g^{-1} and the coulombic efficiency of 83%. For each electrolyte, the irreversible capacities are attributed to the formation of a surface layer on the Si electrode induced by the reductive decomposition of the electrolyte, such as the solvent and LiTFSA salt.

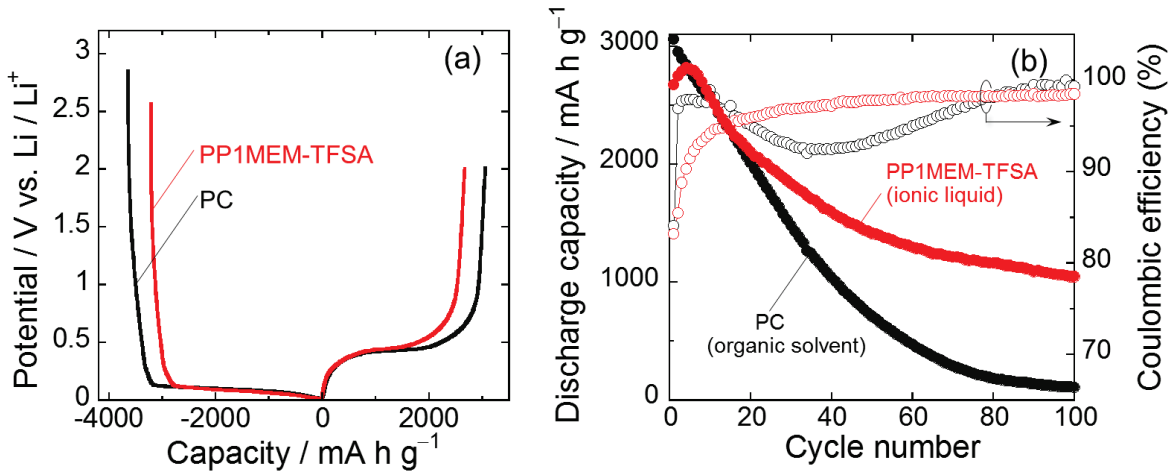

Figure 4-3. (a) Initial charge−discharge curves of Si electrodes in 1.0 M LiTFSA-dissolved in PC and PP1MEM-TFSA. (b) Dependence of discharge (Li-extraction) capacities and coulombic efficiencies on cycle number for Si electrodes in the electrolytes using PC (organic solvent) and PP1MEM-TFSA (ionic liquid).

Figure 4-3b represents dependence of the discharge (Li-extraction) capacities and coulombic efficiencies on cycle number for the Si electrodes in PC and PP1MEM-TFSA.

Although the Si electrode in PC showed the high discharge capacity of 3060 mA h g^{-1} at the first cycle, the capacity quickly decreased to 110 mA h g^{-1} by the 100th cycle, resulting in a very poor cycling performance. This significant capacity decay originates from disintegration of the Si electrode caused by stresses generated during the alloying and dealloying reactions of Si with Li. In contrast to the cycling performance obtained from the organic electrolyte, PP1MEM-TFSA delivered an excellent cyclability; the reversible capacity of over 1000 mA h g^{-1} was maintained even after the 100th cycle. The decline of the coulombic efficiency at around the 30th cycle in PC mainly indicates disintegration such as the peeling of the active material from the current collector. In the PP1MEM-TFSA, the efficiency was gradually improved with increasing the number of cycles, and it reached 95% at the 10th cycle and maintained higher than this value in the subsequent cycles. This behavior indicates that the disintegration degree of the electrode was relatively small in comparison with that in PC. Note that the electrode performance was significantly enhanced just by changing the electrolyte solvent from an organic solvent to the ionic liquid despite using the same Si as the active material.

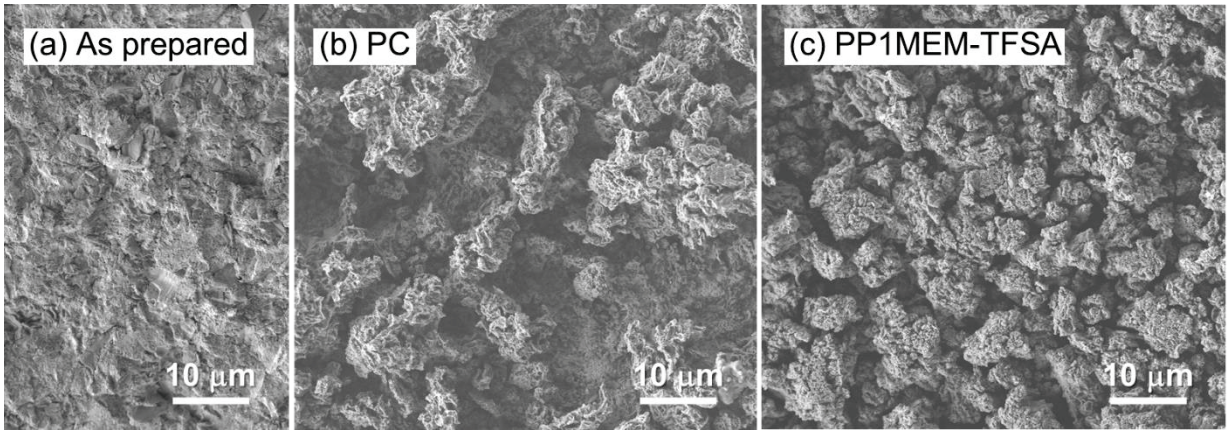

Figure 4-4. FE-SEM images of Si thick-film electrodes (a) as prepared and after 100th charge–discharge cycling in (b) PC and (c) PP1MEM-TFSA.

To investigate the surface morphologies of the Si electrodes before and after the 100th charge−discharge cycling in the organic and ionic liquid electrolytes, SEM observations were performed (Figure 4-4). The as-prepared Si electrode showed a comparatively smooth surface as shown in Figure 4-4a. After cycling in PC, the author can clearly observe disintegration of the Si electrode related to the rapid capacity fading (Figure 4-4b). In addition, the regions in which the disintegration occurred were localized. Meanwhile, the disintegration of the Si electrode was relatively suppressed in PP1MEM-TFSA though there were changes in the surface morphology such as a partial breakup and formation of cracks (Figure 4-4c). It appears that the breakup is uniformly generated over the entire electrode in comparison to the organic electrolyte system. Based on these results, it is inferred that disintegration of the Si electrodes in the respective electrolytes proceeded by different mechanisms.

Figure 4-5a shows the cyclic voltammogram of the Si electrode in the ionic liquid electrolyte of 1.0 M LiTFSA-dissolved in PP1MEM-TFSA. In the cathodic profile, two peaks at 1.5 V and 1.1 V vs. Li/Li^+ were observed at the first cycle. These peaks are attributed to the reductive decomposition of the TFSA anion to form surface layers on the Si electrode.[77,101] A sharp peak below 0.15 V vs. Li/Li^+ is assigned to an alloying reaction of Si with Li, which proceeds according to the following equations:[1,2,34]

$$c\text{-Si} + x\text{Li}^+ + x\text{e}^- \rightarrow a\text{-Li}_x\text{Si} \qquad (1)$$

$$a\text{-Li}_x\text{Si} + y\text{Li}^+ + y\text{e}^- \rightarrow c\text{-Li}_{15}\text{Si}_4 \qquad (2)$$

In the anodic profile corresponding to the delithiation process, the author confirmed two peaks at 0.34 V and 0.48 V vs. Li/Li^+ at the first cycle. These peaks indicate the following Li-extraction reactions of the Li−Si alloy phases:[1,2,34]

$$c\text{-Li}_{15}\text{Si}_4 \rightarrow a\text{-Li}_x\text{Si} + y\text{Li}^+ + y\text{e}^- \qquad (3)$$

$$a\text{-Li}_x\text{Si} \rightarrow a\text{-Si} + x\text{Li}^+ + x\text{e}^- \qquad (4)$$

At the second cycle, a cathodic peak appeared at 0.18 V vs. Li/Li^+, which originates from the electrochemical lithiation of *a*-Si. Incidentally, a broad and small peak appeared between 0.15 and 0.30 V vs. Li/Li^+ at the first cycle is not the same as the alloying reaction of *a*-Si with Li. This reduction wave is probably attributed to a lithiation of Si with small crystallite size inside its electrode (Figure 4-5a).[109,110] The author conducted cyclic voltammetry measurement for an electrode prepared by using nano-Si powder with smaller crystallite size. The size calculated from XRD peak of Si (1 1 1) plane is 22 nm whereas that of the commercial Si powder used in this paper is 84 nm. Figure 4-6 shows XRD patterns of these powders and cyclic voltammograms of the Si electrodes at the first cycle in 1.0 M LiTFSA/PP1MEM-TFSA. As evidenced by these profiles, the wave reduction was larger in the electrode prepared by using nano-Si powder. Therefore, the author concluded that the wave reduction is attributed to a lithiation of Si with small crystallite size inside the electrode. An important point is that *c*-Si undergoes amorphization, being converted to *a*-Si by the alloying and dealloying reactions with Li, and its amorphous phase remains after the first cycle, as observed in the inset of Figure 4-5a.[111] In addition, the peak intensity for the electrochemical lithiation of *a*-Si increased with cycling, and it suggests that an amorphization of *c*-Si gradually proceeded. Figure 4-5b depicts Raman spectra at arbitrary points on the Si electrode before and after cycling. The as-prepared Si electrode showed a peak at 520 cm^{-1} indicating *c*-Si. The author confirmed that the peak at 520 cm^{-1} shifted to 490 cm^{-1} at an arbitrary point on the electrode after the charge−discharge cycling, which means that *c*-Si is transformed into *a*-Si, and agrees with the cyclic voltammetry measurement results. At another point on the electrode, however, a peak located intermediate between 490 and 520 cm^{-1} was also observed. The peak at around 500 cm^{-1} originates from the polycrystalline Si (*poly*-Si) that is an aggregation of small silicon crystals.[112,113] Obrovac and Krause *et al*. investigated the reaction mechanisms of *c*-Si as Li-ion battery anode by various electrochemical tests, and demonstrated that *c*-Si is partially maintained in the potential

above 170 mV vs. Li/Li^+ whereas an excess lithiation below this potential causes transformation into amorphization.[109] In addition, Grey *et al*. reported that the formation of Li−Si alloys requires Si−Si bond-breaking with a high activation barrier.[114] While the author employed the potential of 0.005 V vs. Li/Li^+ as a lower cutoff voltage, the presence of *poly*-Si implies that a sufficient alloying reaction in partial regions of the Si electrode did not occur (*e.g.*, lithiation of Si up to LiSi and $Li_{12}Si_7$ phases having only a low Li content). Thus, the crystallinity of Si in the electrode after cycling can be identified from the Raman shift. It can be clarified which part on the surface of Si electrode reacted with Li.

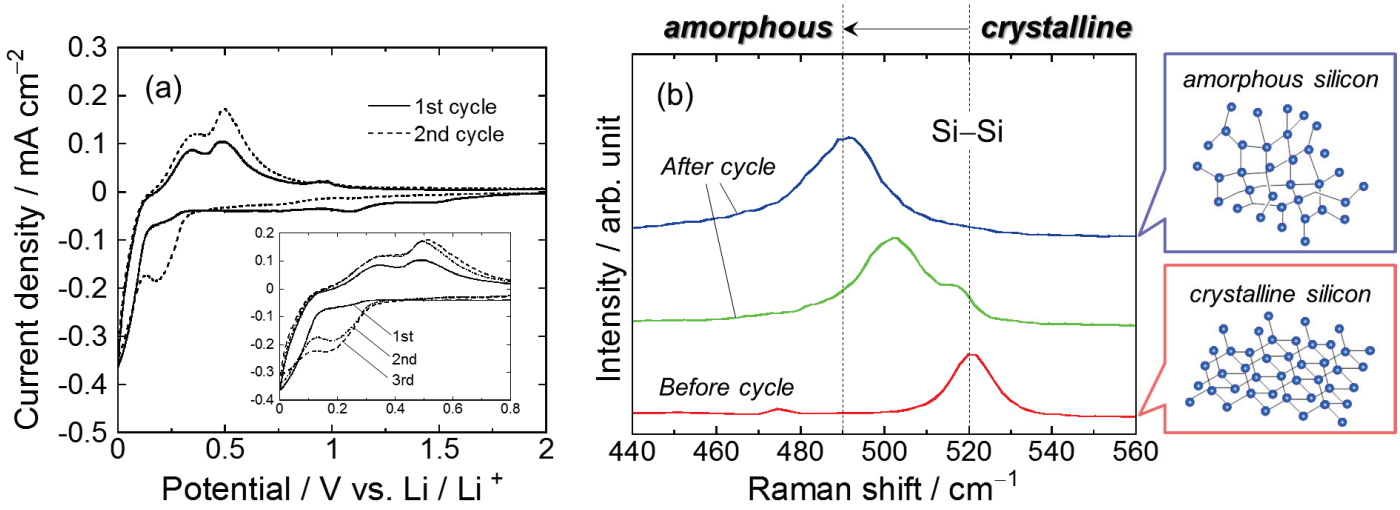

Figure 4-5. (a) Cyclic voltammogram of Si thick-film electrodes at the first cycle and second cycle in 1.0 M LiTFSA/PP1MEM-TFSA. (b) Raman spectra of Si thick-film electrodes before and after cycling.

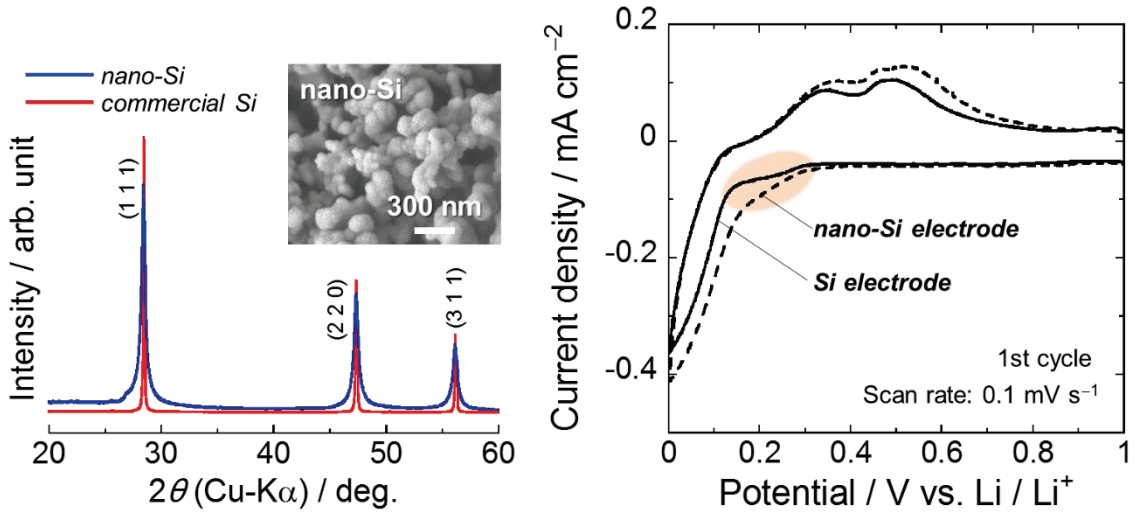

Figure 4-6. (left) XRD patterns of nano-Si and commercial Si powders used in this study. Inset SEM image is the nano-Si powder. (right) Cyclic voltammograms of Si electrodes at the first cycle in 1.0 M LiTFSA/PP1MEM-TFSA. The Si electrodes were prepared by using the commercial Si and nano-Si powders.

To visualize the regions that Si reacted with Li on the electrode in the electrolyte using PC or PP1MEM-TFSA, Raman mapping analyses of the Si electrodes at a state of Li-extraction after the 10th cycle were conducted (Figure 4-7). Raman images were made by plotting the band position with the maximum intensity in the frequency range from 490 to 520 cm^{-1}. The mapping area was set at 7 × 7 μm^2, and the Raman spectra of 400 points (20-by-20 points) were recorded. For comparison, the analysis of the Si electrode before cycling was also performed, and the author confirmed that all of the analyzed areas are composed only of *c*-Si without *a*-Si and *poly*-Si (Figure 4-8).

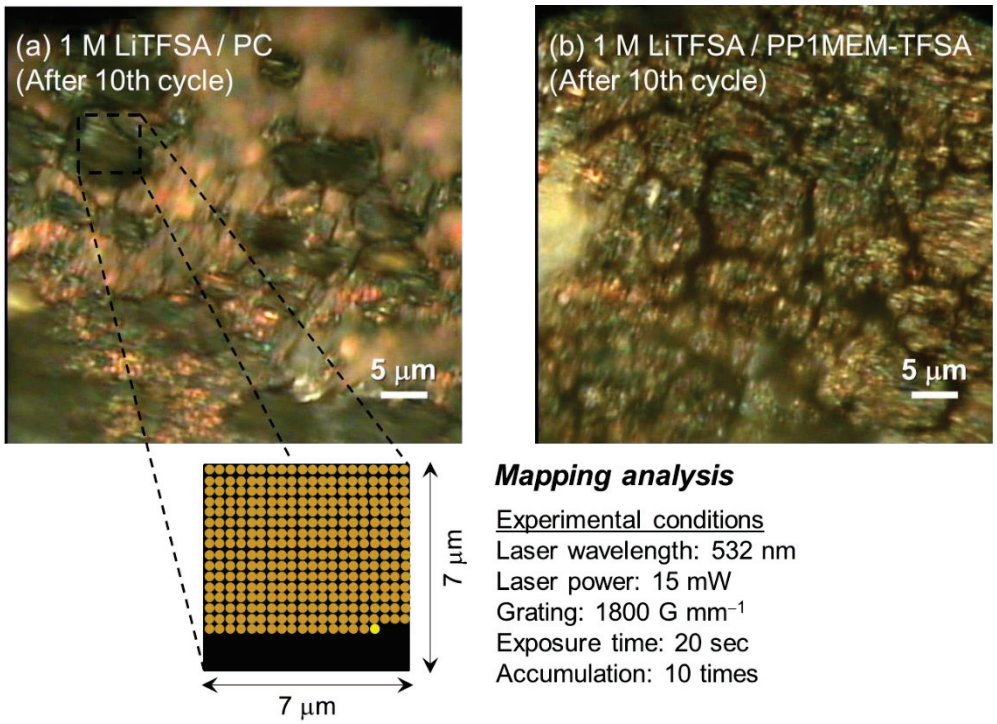

Figure 4-7. Optical images for surface morphology of Si thick-film electrodes after cycling in 1 M LiTFSA-dissolved in (a) PC and (b) PP1MEM-TFSA.

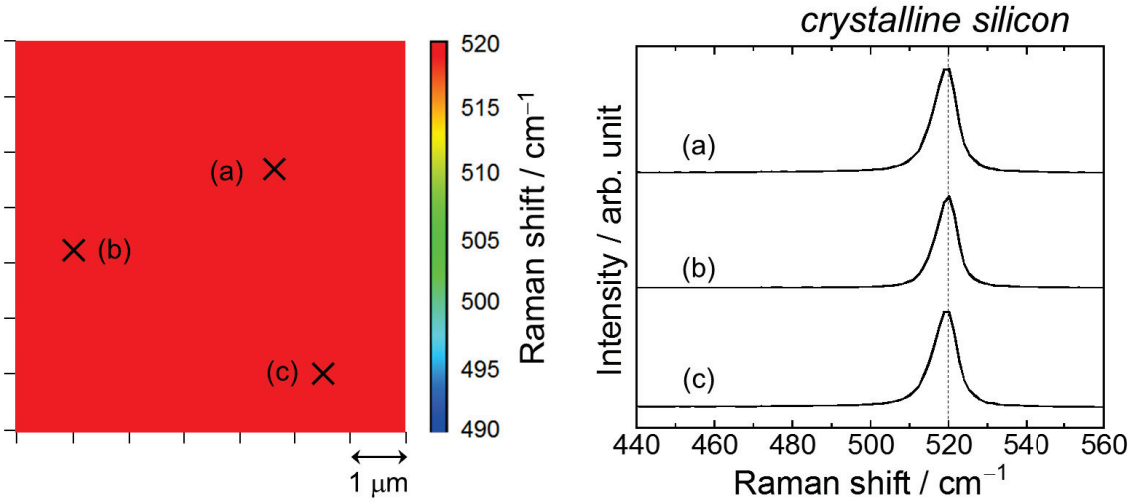

Figure 4-8. (left) Surface Raman images of Si thick-film electrode before electrochemical test, and (right) Raman spectra at several point in the Raman image.

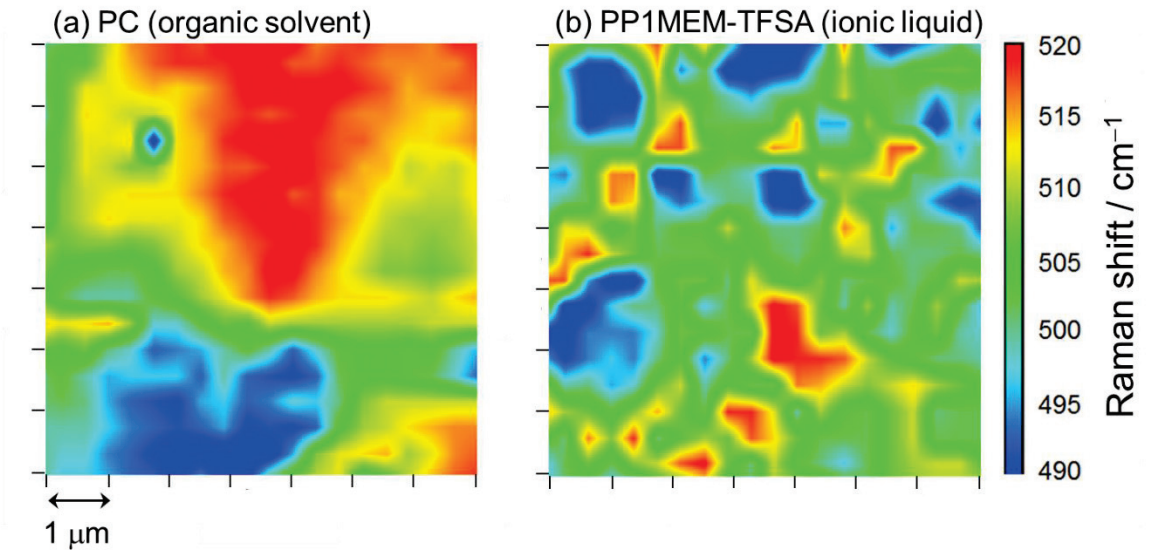

Figure 4-9. Raman images of Si electrode surface after the 10th cycle in the electrolytes using (a) PC and (b) PP1MEM-TFSA. Raman map was made by plotting the band position with maximum intensity in the frequency range from 490 to 520 cm^{-1}. The mapping area is 7×7 mm^2. Red-colored regions indicate the presence of crystalline Si (unreacted Si with Li).

Figure 4-9 displays the Raman images of the Si electrode after cycling in PC and PP1MEM-TFSA, which provides an insight into the deterioration mechanism of the Si electrode. In the Si electrode after cycling in PC (Figure 4-9a), *c*-Si corresponding to the red regions in the image, unreacted Si with Li, were unevenly distributed on the electrode. In other words, Li-insertion into the Si electrode locally took place in the limited area. This is considered to be due to a nonhomogeneous surface layer on the electrode. PC-based organic electrolytes are generally decomposed to inhomogeneously form a surface layer on a negative electrode. The surface layer consists of organic and inorganic compounds such as lithium alkyl carbonates ($ROCO_2Li$) and lithium carbonate (Li_2CO_3), and have uneven thicknesses.[103,109]

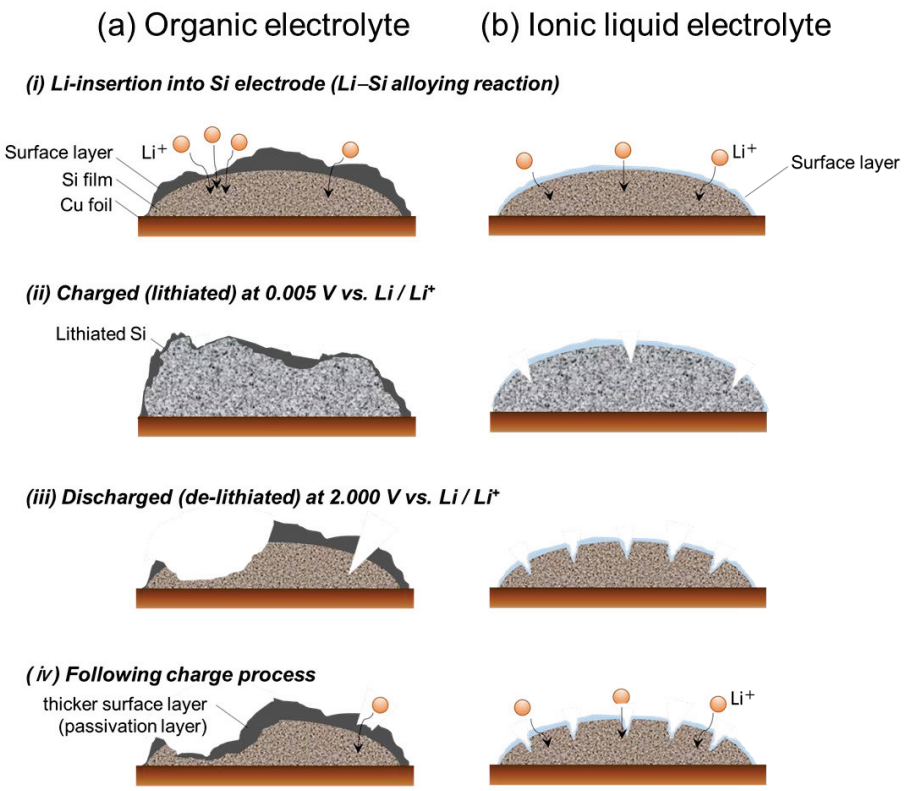

Figure 4-10. Schematic illustrations for proposed deterioration mechanism of Si electrodes in (a) organic electrolyte and (b) ionic electrolyte system.

It is believed that Li ions were preferentially and intensively inserted into the electrode through not thicker parts but thinner parts of the surface layer because thicker parts impede the Li-insertion reactions. Therefore, the author can speculate that the deterioration of the Si electrode in PC progresses as described below (Figure 4-10). For the uneven Li-insertion, extreme volume expansion and contraction occur in the specifically localized regions of the Si electrode, which intensively generates an accumulated stress in the regions. This leads to severe disintegration of the Si electrode which then results in the poor cycle stability. In addition to

this, the extreme volume changes occurring in the case of using the Si-based electrode bring about the formation of cracks, as shown in Figure 4-11.

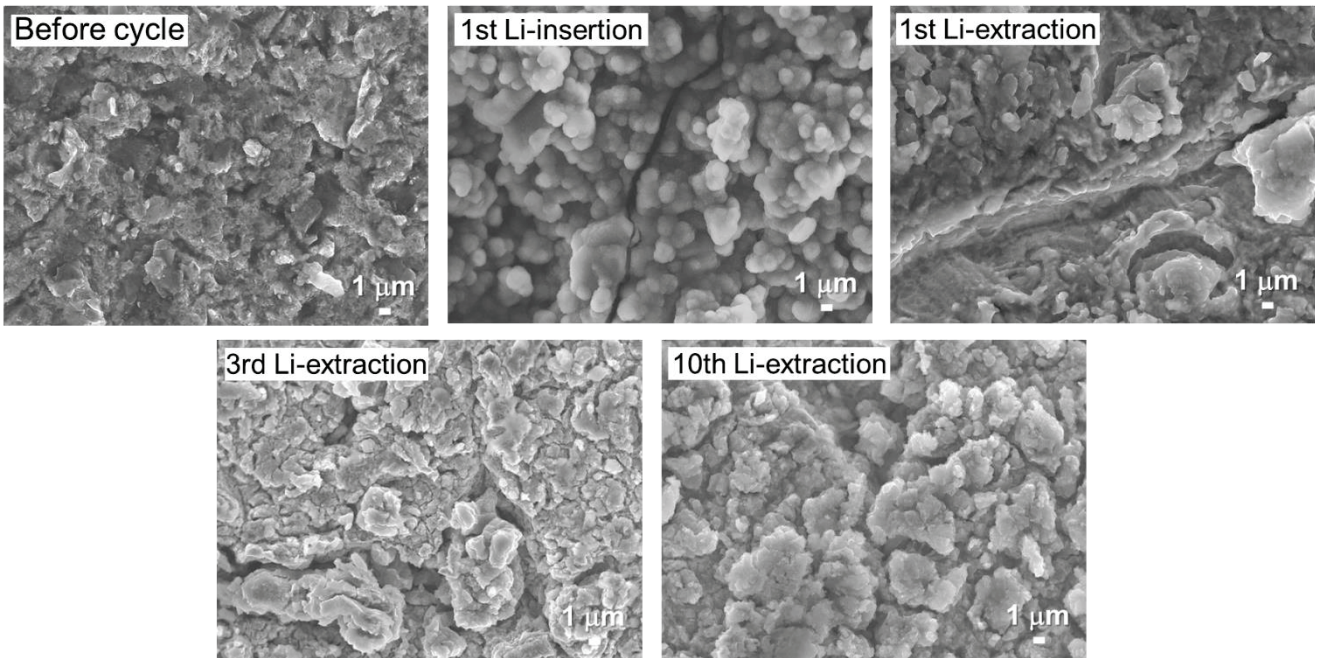

Figure 4-11. FE-SEM images for surface morphology of Si thick-film electrodes before cycling test, after charge (lithiation) at 0.005 V vs. Li/Li^+, after discharge (de-lithiation) in the first cycle, after 3rd Li-extraction, and 10th Li-extraction states. The electrolyte used in this work is 1 M LiTFSA/PC.

After Li-extraction from the Si electrode, the crack becomes larger, and a partial breakup of the electrode occurs. These repeated phenomena induced by the charge−discharge cycling breaks the surface layer on the electrode and thereby exposes the fresh Si electrode surface to electrolyte, where the surface layer is reconstructed by decomposition of the electrolyte. The continuous growth of surface layer makes itself thicker, and leads to a further increase in the resistance for Li-insertion into the Si, which partially passivates the Si electrode surface.[115] In fact, the Raman image obtained in PC clearly shows that a large part of *c*-Si remained even

after the 10th cycle. The passivation reduces utilization of the active material, which is also responsible for the poor cycle performance of the Si electrode in the organic electrolyte. Here, the following question arises; “Since the reversible capacity at the first cycle reached 3060 mA h g^{-1} in PC, almost all parts of the original *c*-Si must undergo amorphization by Li−Si alloying reaction to transform into *a*-Si or *poly*-Si. However, there are the large part of *c*-Si in Figure 4-9a in spite of its large capacity. Does the capacity support the Raman imaging data?” As an answer for the question, the author considers that the peeling from the current collector takes place by the 10th cycle due to the intensive Li-insertion because the author has confirmed large cracks (Figure 4-11) and a resulting exposed Cu foil (Figure 4-7) after the charge−discharge cycling. It is suggested that the large capacity was mainly contributed by the reaction of the Si peeled from the Cu current collector. In contrast to the organic electrolyte system, the Raman image of the Si electrode cycled in PP1MEM-TFSA reveals that the domains of *a*-Si and *poly*-Si were homogeneously distributed on the electrode surface (Figure 4-9b). This result reflects the fact that Li ions were uniformly inserted into the entire Si electrode in comparison to that in PC. This is probably because ionic liquid-derived surface layers are thin and stable as reported by some researchers.[77,101] By the uniform Li-insertion into the Si electrode over the entire surface, the Si electrode in PP1MEM-TFSA can relatively avoid the stress accumulation in localized regions, which suppresses the severe disintegration of the Si electrode leading to a rapid capacity fading. This is considered to be the reason why the cycle performance of the Si electrode was significantly improved by applying the ionic liquid instead of the conventional electrolytes. In addition, results of the new Raman analysis revealed that a surface layer induced by the decomposition of the electrolyte plays a key role in the improvement of the cycle performance of the Si electrode. The author will investigate the characteristics of their surface layer such as the chemical composition and thickness in a future study.

Even though the electrode performance was improved by employing the ionic liquid electrolyte, a capacity decline inevitably induced by the large volume changes of Si remains a challenge to be solved. This unfavorable phenomenon originates from an intrinsic property of Si as Li-ion battery anode. The author considered that if we suppress the large volume changes of Si by controlling the amounts of Li insertion and extraction in moderation,[116,117] a significant enhancement of its cycle performance could be attained by the effect of uniform Li-insertion into Si that comes from the ionic liquid electrolyte. Figure 4-12a shows variation in discharge capacity versus cycle number for Si electrodes at the constant discharge capacity of 1000 mA h g^{-1}. Although the Si electrode in PC showed a stable capacity retention up to the 166th cycle, the capacity then declined. On the other hand, the electrode performance in PP1MEM-TFSA was noticeably improved as expected; a high capacity of 1000 mA h g^{-1} was achieved even at the 790th cycle.

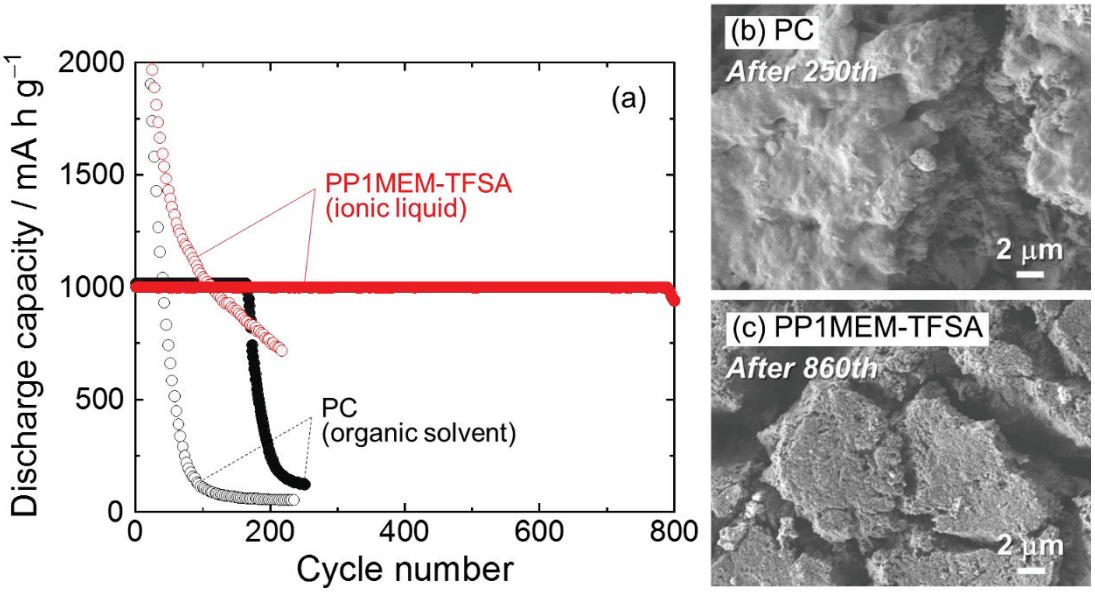

Figure 4-12. (a) Variation in discharge (Li-extraction) capacity of Si electrodes in 1.0 M LiTFSA-dissolved in PP1MEM-TFSA and PC versus cycle number for Li-extraction level fixed at 1000 mA h g^{-1}. For comparison, performances without a capacity limit are also plotted. FE-SEM images of Si electrodes after charge-discharge cycling test in (b) PC and (c) PP1MEM-TFSA.

Panels of 12a and 12b of Figure 4 compare FE-SEM images of the Si electrode surface after a capacity decline in both electrolytes. The author has conducted the SEM observation of the electrodes at the 250th cycle for PC and the 860th cycle for PP1MEM-TFSA. When using PC, it is apparent that the electrode surface is covered with a thick precipitate layer due to an accumulation of decomposition products. The thick surface layer is responsible for inhibiting the Li-insertion into the interior portion of the electrode. In particular, it prevents Li ion diffusion to the bottom of the electrode film that is associated with a decrease in the utilization of the active material. This is probably the reason for the capacity decline at the relatively early cycle. No visible precipitate layer on the Si electrode cycled in PP1MEM-TFSA was observed in sharp contrast to that in the organic electrolyte system, which strongly suggests that the surface layer formed on the electrode in the ionic liquid electrolyte is thinner and more stable. These characteristics can allow Li ions to diffuse through the surface layer to sufficiently and homogeneously lithiate the whole Si in the electrode for a long period. Therefore, the author considers that the Si electrode in PP1MEM-TFSA exhibited the good cycle stability with a reversible capacity of 1000 mA h g^{-1} up to the 790th cycle when the extent of the electrode collapse reached its capacity decline. An application of PP1MEM-TFSA to Si-based composite electrodes that the author has demonstrated its superiority, thus it is expected that the electrode performance can be further improved.

3.4 Summary

The Si thick-film electrodes were prepared by a gas-deposition method, and the deterioration mechanisms of Si electrodes in organic and ionic liquid electrolytes were investigated by Raman mapping analysis. Although the Si electrode in the electrolyte of using PC showed the comparatively high discharge capacity of 3060 mA h g^{-1} at the first cycle, the capacity was quickly decreased to 110 mA h g^{-1} by the 100th cycle. In contrast to the organic electrolyte system, the remarkably improved performance was obtained in the ionic liquid

electrolyte based on PP1MEM-TFSA; the capacity of 1050 mA h g^{-1} was achieved even at the 100th cycle. Raman mapping analyses of the Si electrodes after the 10th cycle revealed the following. In PC, Li−Si alloying and dealloying reactions, Li insertion and extraction, occurred in specific localized regions in the Si electrode. Hence, the stress accumulations were intensively generated in these regions, which led to severe disintegration of the Si electrode causing the rapid capacity attenuation. On the other hand, in PP1MEM-TFSA, Li ions were uniformly inserted into the electrode, so that the volume expansion and contraction of the electrode would only moderately occur. Furthermore, the high discharge capacity of 1000 mA h g^{-1} was attained even at the 790th cycle by controlling the amount of Li insertion and extraction.

Chapter 5

Novel Negative-Electrode Materials for Na-ion Batteries 1: Electrochemical Na-insertion/extraction Properties of Tin Monoxide (SnO)

5.1 Introduction

Na-ion battery has received interest in large-scale battery system due to its low cost and widespread availability of sodium resources.[24,25] It is, however, difficult to develop the suitable anode and cathode material for reversible Na-insertion/extraction because Na-ion has larger ionic radius than Li-ion. Although carbon-based materials enable to absorb Na ions which are comparable to a capacity of *ca*. 250−300 mA h g^{-1} and good capacity retention[27−32], high capacity Na-storage anodes are required to further increase the energy density of Na-ion battery. Sn is one of promising candidates of anode materials due to its high theoretical capacity of 847 mA h g^{-1} compared with carbonaceous anodes.[118−121] The large capacity originates from an alloying reaction of Na−Sn in the composition range from Sn to $Na_{15}Sn_4$. The volume of Sn is, however, significantly changed during charge–discharge cycle, which leads to disintegration of Sn anode and poor cycle performance. Komaba *et al.* have demonstrated an improved cyclability of Sn electrode by employing both polyacrylate binder and electrolyte additive.[122] On the other hand, SnO anodes for Li-ion battery show superior cycle performance. It has been reported that Li_2O formed in the first cycle plays a role as buffer to alleviate a stress induced by volumetric changes during Li-insertion/extraction[123−125], and that the aggregation of Sn particle is suppressed by Li_2O.[126] As for Na-ion battery anodes, no study has been, however, reported for SnO to the author's knowledge. The author is here suggesting for the first time that SnO has a potential as anode for Na-ion battery with a good electrode performance.

Gas-deposition (GD) method is very favorable for evaluating electrode performance of active material, which has been recently demonstrated by the author.[54,83,127] This method does not require any binder or conductive additive to prepare thick-film electrodes. The feature is a

unique advantage to clarify an original anode performance of pure SnO anode. In this chapter, the author prepared SnO thick-film electrodes by the GD method, and report their electrochemical Na-insertion/extraction properties at the first time. In addition, the author tried to improve their cycle performances by applying fluoroethylene carbonate (FEC) to an electrolyte additive on the basis of the knowledge obtained in chapter 1.

5.2 Experimental Details

SnO powder (99.9%, Wako Pure Chemical Industries, Ltd.) was used as an active material. For comparison, the author used Sn powder (Kojundo Chemical Lab. Co., Ltd. 325 mesh, 99.99%) also. Thick-film electrodes were prepared by a gas-deposition method. The weight of the deposited active materials on the substrate and the deposition area were 80−100 μg and 0.80 cm^2, respectively. The author assembled 2032-type coin cells consisted of a thick-film electrode as the working electrode, Na foil as the counter electrode, electrolyte, and propylene-based separator. The electrolytes used in this study were 1.0 M $NaClO_4$-disssolved in propylene carbonate (PC, $C_4H_6O_3$; Kishida Chemical Co., Ltd.) without and with addition of 20 vol.% fluoroethylene carbonate (FEC, $C_3H_3FO_3$; Kanto Denka Kogyo Co., Ltd.). The gas-deposition and the cell assembly were performed throughout in a purge-type glove box (Miwa MFG, DBO-2.5LNKP-TS) filled with an argon atmosphere in which oxygen and water had been removed completely. In the glove box, a dew point and oxygen content were maintained below –100°C and below 1 ppm, respectively. Constant current charge−discharge tests were carried out using an electrochemical measurement system (HJ-1001 SM8A, Hokuto Denko Co., Ltd.) in the potential range between 0.005 and 2.000 V vs. Na/Na^+ at 303 K under the constant current density of 50 mA g^{-1} (0.07 *C*). The surface morphologies of the thick-film electrodes were observed by using a field-emission scanning electron microscope (FE-SEM, JSM-6701F JEOL Co., Ltd.). A crystal structure of active materials was investigated using X-ray diffractometer (Ultima IV Rigaku Co., Ltd.) with CuKα radiation. Raman spectra of the powder

were measured through the use of a Raman microscopy system (NanofinderFLEX, Tokyo Instruments, Inc.) at room temperature. As a reference sample, SnO_2 (99.9%, Wako Pure Chemical Industries, Ltd.) was also investigated.

5.3 Results and Discussion

Figure 5-1 shows the first charge–discharge (Na insertion–extraction) curves for SnO and Sn thick-film electrodes. In the Sn electrode, the initial charge and discharge capacities were 740 and 560 mA h g^{-1}, respectively, with the first coulombic efficiency of 76%. The irreversible capacity is attributed to reductive decomposition of electrolyte. Four plateaus were observed in a potential range between 0.15 and 0.85 V vs. Na/Na^+ on the discharge curve. These plateaus indicate that Sn and Na formed binary alloy phases, $NaSn_3$, α-NaSn, Na_9Sn_4, and $Na_{15}Sn_4$, as reported by Obrovac *et al.*[118] On the other hand, SnO electrode delivered the initial discharge capacity of 580 mA h g^{-1}, which is approximately two times larger than that obtained from carbon-based anode.[27–32] The initial charge capacity and coulombic efficiency were 1040 mA h g^{-1} and 56%, respectively. It is considered that the low coulombic efficiency was caused by an irreversible reaction of SnO with Na in the first charge process.

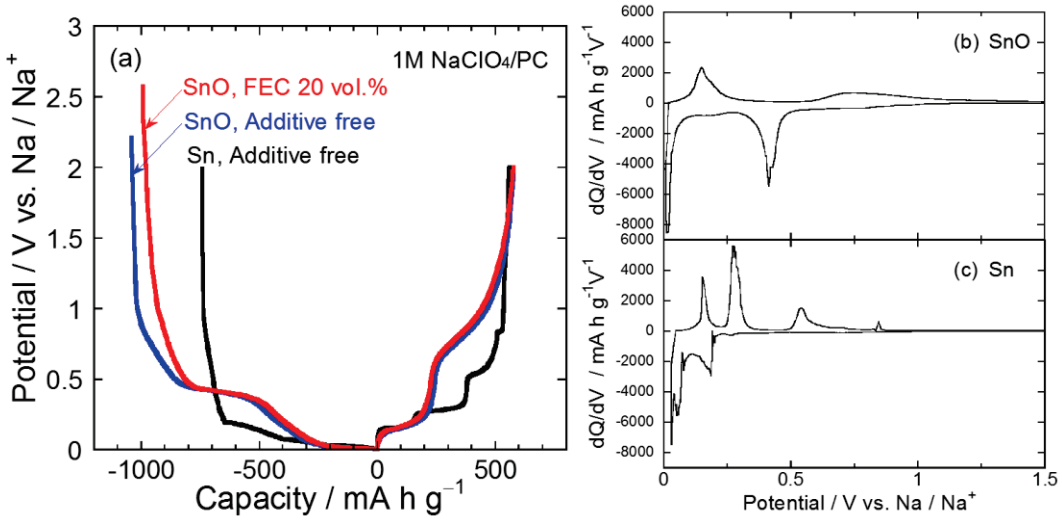

Figure 5-1. (a) Initial charge-discharge curves of SnO and Sn thick-film electrodes in 1.0 M $NaClO_4$/PC without and with 20 vol.% FEC, and differential capacity versus potential (dQ/dV) curves at the first cycle for (b) SnO and (c) Sn thick-film electrodes in 1 M $NaClO_4$/PC.

Figure 5-1(b) and 1(c) give differential capacity (dQ/dV) curves at the first cycle for the SnO and Sn electrodes to discuss the charge−discharge reaction. In the cathodic profile, the SnO electrode showed two sharp peaks at 0.41 V and 0.015 V and a broad peak at 0.18 V vs. Na/Na^+. The peak at 0.41 V is attributed to a reductive reaction of SnO to form metallic Sn and Na_2O. The author did not confirm the peak at 0.41 V in the subsequent charge–discharge cycles, indicating that the reductive reaction is irreversible. The broad peak at around 0.18 V and the sharp peak at 0.015 V vs. Na/Na^+ are assigned to alloying reactions of Sn with Na such as a crystalline $Na_{15}Sn_4$ phase, which corresponds to the dQ/dV profiles of not only our Sn electrode but also those of other Sn-based electrode.[118] In the anodic profile, the author observed a sharp peak at 0.14 V and a very broad peak at a region from 1.5 to 0.6 V vs. Na/Na^+. These peaks are related to Na-extraction from each Na–Sn phase.[118,119,128] Consequently, SnO appears to react with Na as shown in the following equations:

$$SnO + 2Na^+ + 2e^- \rightarrow Sn + Na_2O \qquad (1)$$

$$4Sn + 15Na^+ + 15e^- \rightleftarrows Na_{15}Sn_4 \qquad (2)$$

From the calculation based on the reaction mechanism mentioned above, the SnO provides the theoretical capacity of 746 mA h g^{-1}. In this study, the reversible capacity was 580 mA h g^{-1}, which was smaller than the theoretical capacity. The relatively small capacity was caused by a decrease in utilization of active material due to poor electrical conductivity of oxide. Raman spectrum of SnO powder used in this study showed SnO_2 being, though the author could not recognize SnO_2 in XRD pattern of the SnO powder, (Figure 5-2a and 2b). The result indicates that relative content of Sn in the active material is smaller than that in a pure SnO, which also restricts reversible capacity obtained from Na−Sn alloying reaction.

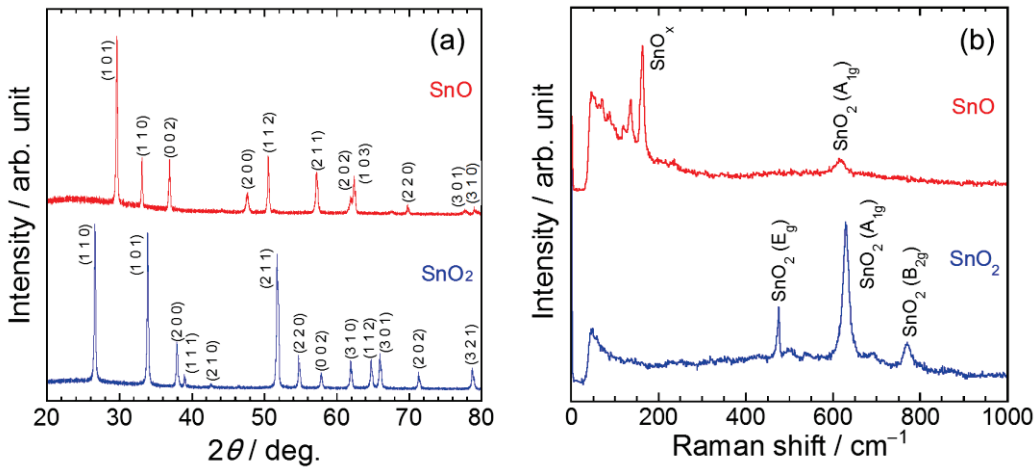

Figure 5-2. (a) XRD pattern and (b) Raman spectra of SnO powder used in this study. As a reference, data of SnO_2 powder is also shown.

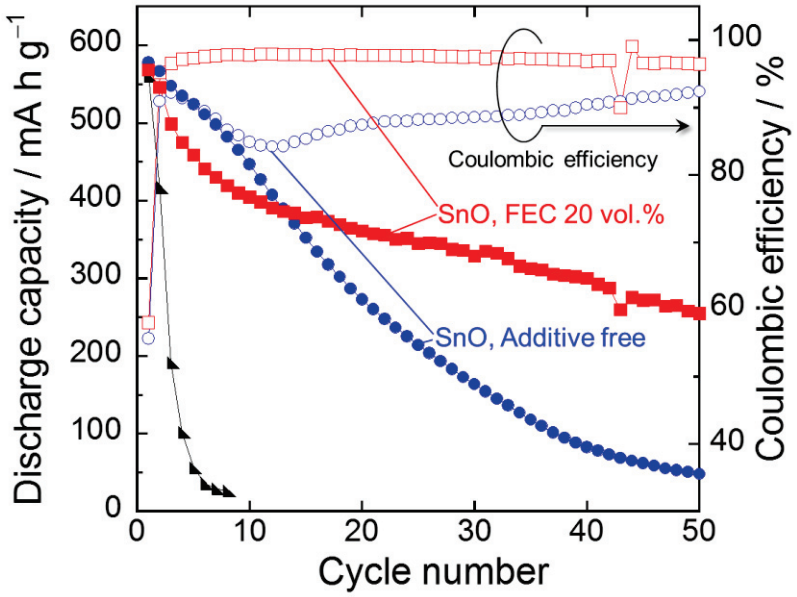

Figure 5-3. Cycling performances and coulombic efficiencies of SnO and Sn thick-film electrodes.

Figure 5-3 represents cycling performances and coulombic efficiencies of the SnO and Sn electrodes in 1.0 M $NaClO_4$/PC without and with 20 vol.% FEC. Although the Sn electrode showed a comparatively high discharge capacity of 560 mA h g^{-1} at the first cycle, the capacity was quickly decreased to 30 mA h g^{-1} by the sixth cycle, resulting in a very poor cycle performance. The reason for the capacity decay is probably the disintegration of Sn electrode caused by the stress. The volume of Sn is significantly changed during Na-insertion/extraction process, and the expansion ratio of the specific volume from β-Sn to $Na_{15}Sn_4$ reaches approximately 530%. The mechanical stress induced by repeating charge−discharge cycle leads to the deterioration of Sn electrode.[118,119] The author confirmed that the Sn electrode showed low coulombic efficiencies of less than 90% for initial sixth cycles (not shown here). It is considered that the low reversibility also results from the disintegration of the Sn electrode. In contrast, the SnO electrode in the additive-free electrolyte maintained the discharge capacity of 260 mA h g^{-1} at the 20th cycle, which was superior cycle performance to that of the Sn electrode. This better cyclability is possibly attributed to structural feature. The author is here suggesting that Na_2O formed in the first cycle plays a role as a matrix to release the stress, leading to the better cyclability of SnO electrode as similar to Li−SnO system.[123−125] The capacity decay was, nevertheless, observed in the subsequent cycles, and the discharge capacity decreased to only about 50 mA h g^{-1} by the 50th cycle. This phenomenon was presumably arisen from two reasons. One is the disintegration of SnO electrode. The other reason is a deterioration of transport property of Na-ion in a surface layer formed between the electrode and the electrolyte. In the first cycle, electrolytes based on PC solvent are decomposed to form the surface layer consisted of organic and/or inorganic compounds on the anode.[129] In the case of Sn-based material as an anode, the drastic volume expansion and contraction occur by alloying and dealloying reactions of Sn with Na, which causes the partial damages of the surface layer to expose new surfaces of active material layer. The surface layers are

reconstructed by decomposition of the electrolyte at the next charge process.[130] The author considered that the continuous formation of surface layer makes itself thicker and prevents the Na-ion transfer through it, leading to the decrease in utilization of active material.[131,132] It is widely known that FEC is an effective electrolyte additive for improving cycle performance by passivating surface of Sn-based anodes.[122,133] In order to improve the cycle performance of the SnO electrode, the author used FEC-added electrolyte to modify the surface of SnO electrode. As shown in Figure 5-1(a), the SnO electrode in the electrolyte containing FEC exhibited the initial capacity of 570 mA h g^{-1} and similar potential profile to that in the electrolyte without FEC. The first coulombic efficiency of 58% was observed. There was no significant difference in the first coulombic efficiencies between each SnO electrode in both the electrolytes. Although the coulombic efficiency of SnO electrode in the additive-free electrolyte was temporarily increased to 92% at the third cycle, the coulombic efficiency was decreased to 84% at the tenth cycle and was remained below 90% until 40th cycle. The author considers that these behaviors indicate not only the disintegration of the SnO electrode but also the continuous decomposition of electrolyte. In contrast, the SnO electrode in the electrolyte with FEC constantly exhibited higher coulombic efficiencies than those obtained in the additive-free electrolyte, and the coulombic efficiency was improved to 98% after the sixth cycle. This enhanced reversibility means that the further decomposition of electrolyte was suppressed by introducing FEC additive. It was noteworthy that the SnO electrode achieved a high capacity of 250 mA h g^{-1} even at the 50th cycle. As a result, the capacity retention was remarkably improved to 44%, which was five times higher than that in the electrolyte without FEC.

Figure 5-4 displays FE-SEM images of the SnO and Sn electrodes as prepared and after charge–discharge cycling, respectively, in the electrolytes without and with 20 vol.% FEC. The Sn and SnO electrodes before cycling showed smooth surface, respectively, as shown in Figure

5-4a and 4c. In Figure 5-4b, the author can clearly observe the disintegration of the Sn electrode related to the rapid capacity fading. In both the SnO electrodes after cycling, the author confirmed changes in surface morphology such as the formation of cracks. It is notable point that degrees of disintegration for both the SnO electrodes after cycling in the electrolytes without and with FEC additive were mostly similar (Figure 5-4d and 4e). These results indicate that the capacity decay originates from not only disintegration of SnO electrodes but also deteriorated Na-ion transfer between the electrode and the electrolyte.[134] It was demonstrated that SnO electrode exhibited the initial high discharge capacity and the good cycle performance because FEC additive effectively enhanced the utilization of active material by suppressing deterioration of the Na-ion transfer.

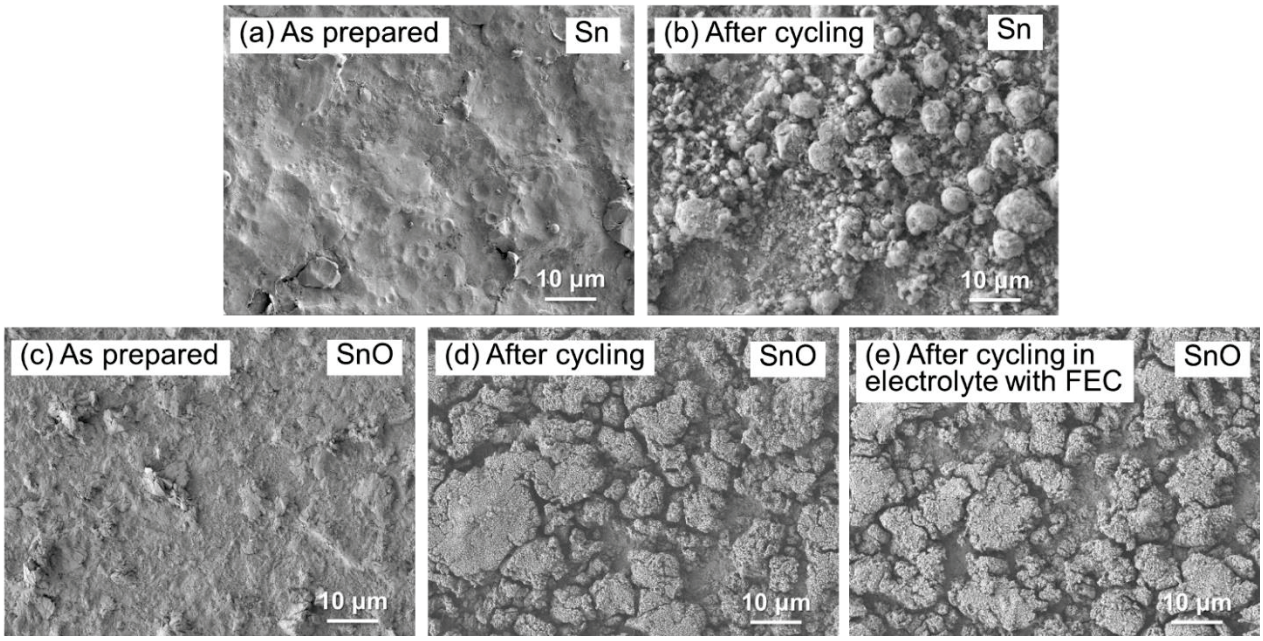

Figure 5-4. FE-SEM images of (a) Sn and (b) SnO thick-film electrodes as prepared and after charge–discharge cycling in (c), (d) 1.0 M $NaClO_4$/PC without additive and (e) with 20 vol.%

The improved Na-ion transfer is expected to upgrade an anode performance of SnO electrode at high-rate charge–discharge condition. Figure 5-5 displays the rate performance of SnO electrodes in the electrolytes of 1.0 M $NaClO_4$/PC without and with 20 vol.% FEC. The rate capability was evaluated at various current densities from 50 mA g^{-1} to 1000 mA g^{-1}. These current densities correspond to a current rate of 0.07 *C* to 1.3 *C* because the author defined 746 mA g^{-1} as 1.0 *C* from the reaction of SnO with Na. The SnO electrode in the additive-free electrolyte showed a rapid capacity fading with increasing current density, suggesting the deterioration of transport property of Na-ion in the surface layer formed between the electrode and the electrolyte. On the other hand, the SnO electrode in FEC-added electrolyte achieved a comparatively high capacity of *ca*. 200 mA h g^{-1} even at a high current density of 500 mA g^{-1} (0.67 *C*). Moreover, when the current density returns to 50 mA g^{-1} (0.07 *C*), the discharge capacity can be recovered, which indicates that FEC additive keeps good Na-ion transfer for long-term charge–discharge cycling.

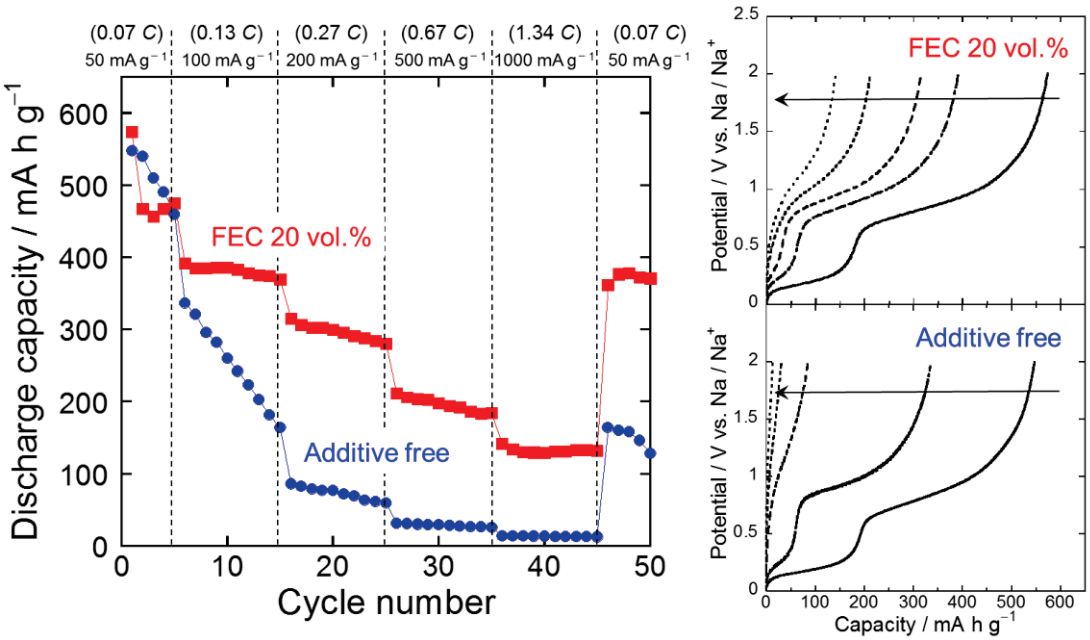

Figure 5-5. Rate capability of the SnO thick-film electrodes in 1 M $NaClO_4$/PC without and with 20 vol.% FEC at various current rates from 50 to 1000 mA g^{-1}.

5.4 Summary

The SnO thick-film electrodes were prepared by a GD method, and their anode performances for Na-ion battery were investigated. When the author used FEC additive, the SnO electrode exhibited the initial high discharge capacity of 570 mA h g^{-1} and achieved 250 mA h g^{-1} at the 50th cycle. In addition to these, the SnO electrode showed a high-rate performance with the capacity of *ca*. 200 mA h g^{-1} at the high current density of 500 mA g^{-1}. From the results of FE-SEM observation, it was revealed that these excellent electrode performances result from structural integrity of SnO and improved the Na-ion transfer by introducing FEC additive.

Chapter 6

Novel Negative-Electrode Materials for Na-ion Batteries 2: Electrochemical behavior of Silicon monoxide (SiO)

6.1 Introduction

A next-generation energy storage device that use Na-ion as the charge carrier, Na-ion battery (NIB), has attracted more and more attention because of its low cost and natural abundance of sodium.[24,25] Development of host materials which can absorb much Na per its formula weight has been needed to realize NIB with a higher energy density. From the perspective, most recent studies of negative electrodes have been focused on alloy-based materials. Germanium (Ge)[135], tin (Sn)[118], and antimony (Sb)[130] react with Na to form binary alloys, which provides high theoretical capacities of 369 mA h g^{-1} (NaGe), 847 mA h g^{-1} ($Na_{3.75}Sn$), and 660 mA h g^{-1} (Na_3Sb). It has been recognized that the group 14 elements with the exception of silicon (Si) are electrochemically active against Na. Despite the existence of NaSi and $NaSi_2$ phases[136,137], there has been no report on electrochemical reactions of Si with Na. If the formation of the NaSi alloy occurs electrochemically, a specific capacity of 954 mA h g^{-1} could be achieved, and its specific capacity is more than three times as large as that of carbon-based materials.[27] In addition, the volumetric change ratio of 244% from Si to fully sodiated Si is relatively small compared with those of Sn (530%)[118] and Sb (390%)[130], which reduces a mechanical stress causing capacity fading. The author guessed that the reason why the Na–Si alloying reaction does not electrochemically occur is due to the bulk-stated Si. Our group has previously demonstrated that SiO being an amorphous material is composed of three-dimensional SiO_4 tetrahedral network similar to silica (SiO_2) glass and metallic Si clusters, and that the Si clusters are finely dispersed in the SiO_4 matrices.[138] The author anticipated that the Si cluster with a high surface energy is electroactive against Na to show a reversible capacity by the formation of the Na−Si alloy. In this chapter, the author investigated fundamental

electrode properties of SiO as a Na-ion battery anode by using thick-film electrodes without any binder or conductive additive. To the best of our knowledge, this is the first report on an anode property of Si-based material.

6.2 Experimental Details

Granular silicon monoxide (SiO, Wako Pure Chemical Industries, Ltd., 99.9%) powder was pulverized by using a high-energy planetary ball mill (Classic Line P-6, FRITSCH) at 380 rpm to prepare an active material powder. The weight ratio of the balls to the powder was set to be 65:1, and the mechanical milling (MM) times were 10 min, 20 min, and 60 min. Crystal structures of these powders were investigated by an X-ray diffractometer (Ultima IV, Rigaku Co., Ltd.) with CuKα radiation and a Raman microscopy system (NanofinderFLEX, Tokyo Instruments, Inc.) with 532 nm line of Nd:YAG laser. The morphologies and particle sizes of the powders were observed by a field emission scanning electron microscope (FE-SEM, JSM-6701F, JEOL Ltd.).

SiO thick-film electrodes were prepared by a gas-deposition method through the use of a helium carrier gas. The deposition area is *ca*. 0.5 cm^2, and the weight of the deposited active material on the substrate was measured to an accuracy of 1 μg by ultra-microbalance (XP6, METTLER TOLEDO) equipped with an anti-vibration table. A typical film thickness was confirmed to be *ca*. 8.0 μm by observation using a confocal scanning laser microscope (CSLM, VK-9700, Keyence). 2032-type coin cells were fabricated from SiO thick-film electrode as working electrode, Na foil as counter electrode, electrolyte of 1.0 M sodium bis(trifluoromethanesulfonyl)amide (NaTFSA)-dissolved in propylene carbonate (PC) (Kishida Chemical Co., Ltd.), and propylene-based separator. To evaluate electrochemical Na-insertion/extraction properties of SiO electrode, galvanostatic charge−discharge cycling tests were performed using an electrochemical measurement system (HJ-1001 SD8, Hokuto Denko

Co., Ltd.) in the potential range between 0.005 and 3.000 V vs. Na/Na^+ at 303 K. The current density was set to 50 mA g^{-1}.

6.3 Results and Discussion

SiO powders underwent pulverization of an agglomeration (Figure 6-1 and 6-2) by a high-energy ball milling to prepare active material powders. In the milled SiO samples for 10 min and 20 min, their particles have similar morphologies with the range from submicrometer to 5 μm. On the other hand, the size in SiO powder for 60 min-milling is much smaller with several hundred nanometer. Although a broad peak indicating SiO was only detected in a pristine sample (not shown here), a diffraction peak originated from Si began appearing at 47.3° in 10 min-milling SiO sample (Figure 6-3), and its peak intensity significantly increased with milling time. In the 60 min-milling sample, the existence of Si is apparent, which means a disproportional reaction of SiO to Si and amorphous SiO_x/SiO_2.[139,140]

Figure 6-1. Photographs of various silicon monoxide (SiO) powders. A granular SiO with a diameter of 2−3 mm (Wako Pure Chemical Industries, Ltd.) was pulverized by using a high-energy planetary ball mill (Classic Line P-6, FRITSCH) at 380 rpm to prepare an active material powder. The weight ratio of the balls to the powder was set to be 65:1, and the mechanical milling (MM) times were 10 min, 20 min, 30 min, 40 min, 50 min, and 60 min, respectively.

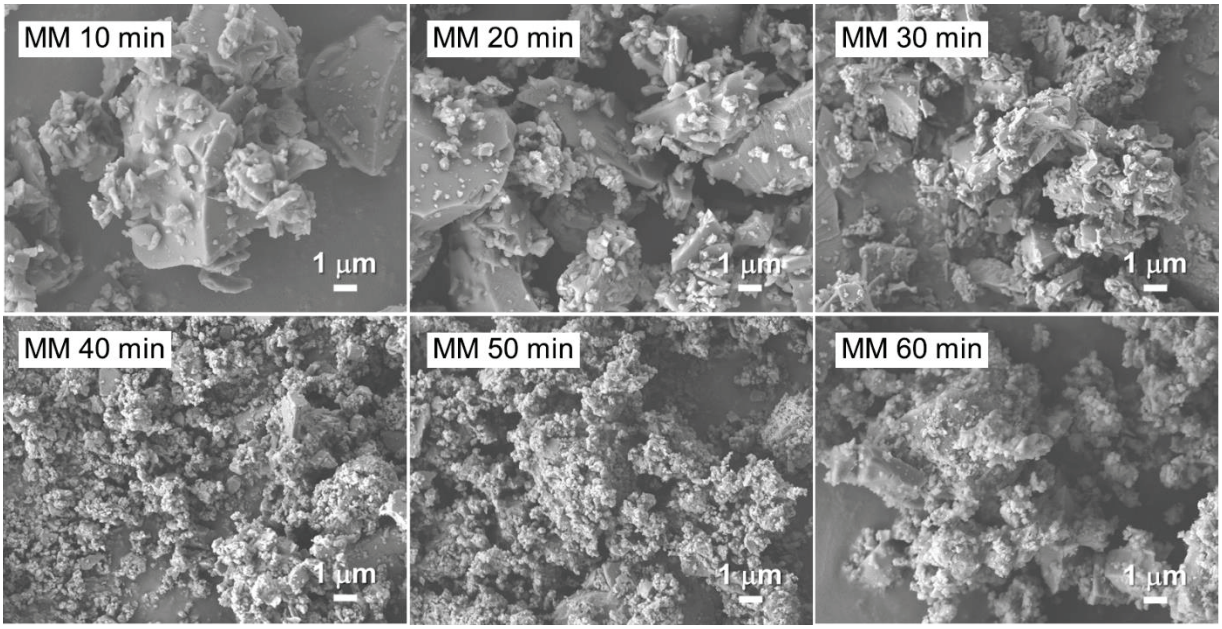

Figure 6-2. FE-SEM images of milled SiO powders at different mechanical milling times. SiO thick-film electrodes were prepared by a gas-deposition method through the use of these powders and helium carrier gas.

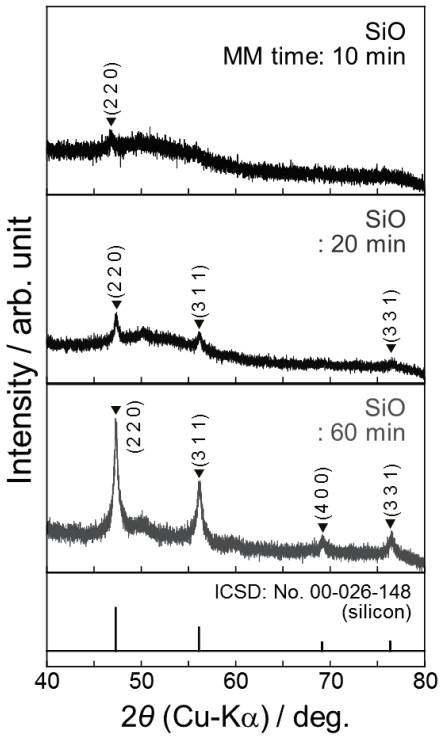

Figure 6-3. XRD patterns of SiO powders prepared by mechanical milling for 10 min, 20 min, and 60 min.

Figure 6-4a compares Raman spectra of pure Si and SiO electrodes. In the Raman spectrum of as-prepared Si electrode, a relatively sharp peak was observed at 520 cm^{-1}. This result indicates that the electrode is composed only of crystalline Si. Meanwhile the electrode consisted of 10 min-milling SiO powder showed a peak at 498 cm^{-1}. This is attributed to transverse optical (TO) mode from microcrystalline (μc)-Si which typically consists of small grains with 20−30 nm in size.[141,142] As is clear from Figure 6-4b, the peak position of TO mode corresponding to μc-Si shifted from 498 cm^{-1} to 505 cm^{-1} with increasing the milling time, which suggests that crystal growth of μc-Si grains, disproportional reaction of SiO, occurred during ball-milling. This agrees with the result obtained from the XRD measurements.

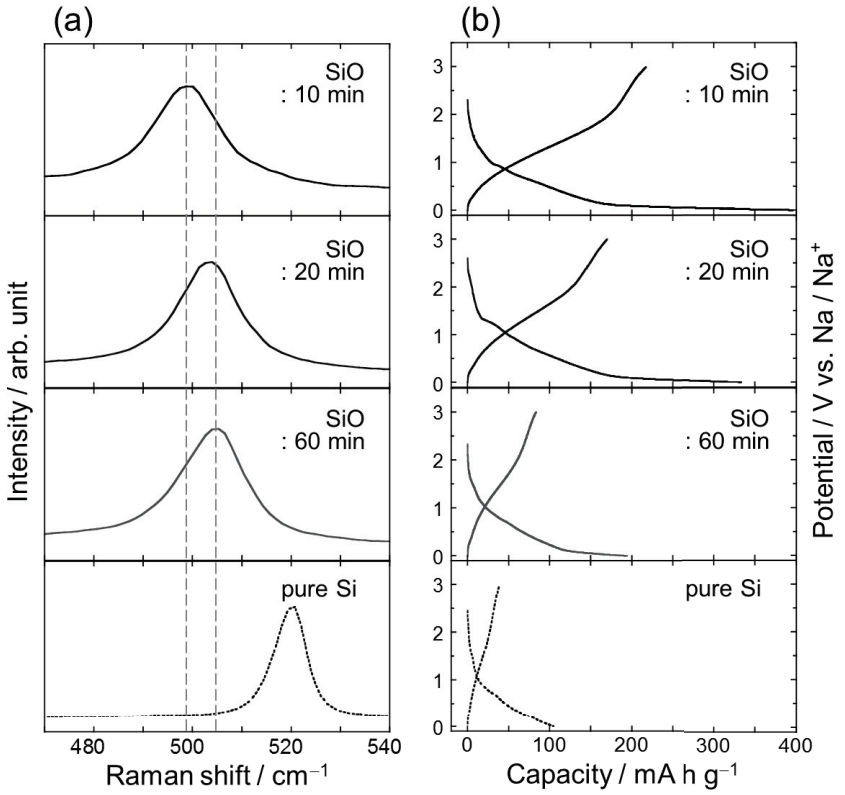

Figure 6-4. (a) Raman spectra and (b) initial charge-discharge (Na insertion−extraction) behaviors of SiO and Si electrodes.

Figure 6-4b represents initial charge−discharge (Na insertion−extraction) curves of the Si electrode and the SiO electrodes. The Si electrode brought no potential plateau and showed only a little reversible capacity. Furthermore, no capacity increasing was found even when using an electrode consisted of a nano-sized Si powder (Figure 6-5). The charge and discharge capacities are due to an electrolyte decomposition. From these result, it is implied that sodiation of crystalline Si (*c*-Si) is an electrochemically-unfavorable reaction at room temperature if not inactive.

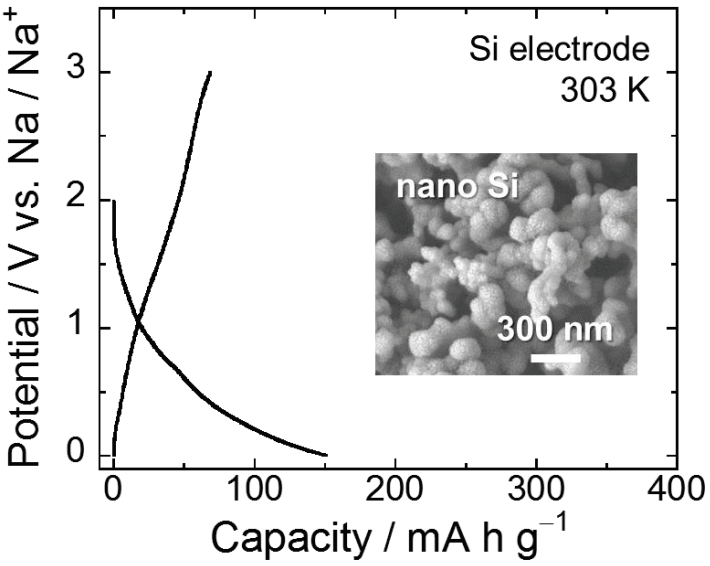

Figure 6-5. Initial charge-discharge profile of electrode composed of nano-Si powder.
Particle size of nano-Si powder: < 300 nm (The FE-SEM image is inserted.)
Electrolyte: 1.0 M NaTFSA/PC, Potential: 0.005−3.000 vs. Na/Na^+, Current density: 50 mA g^{-1}

Komaba *et al*. have reported that an alloying reaction of *c*-Si with Na hardly occurs[122], and Obrovac *et al*. have demonstrated that XRD patterns of Si electrodes did not change during electrochemical tests at 333 K.[143] In contrast to these Si electrodes, potential plateaus at around 0.1 V vs. Na/Na^+ can be confirmed on the Na-insertion curves in all of the SiO electrodes in this study. Their initial discharge (Na-extraction) capacities in the 10 min, 20 min, and 60 min-

milling electrodes were 220 mA h g^{-1}, 170 mA h g^{-1}, and 80 mA h g^{-1}, respectively. Note that the reversible capacity decreased as the peak position in Raman spectra of SiO electrodes shifts to higher wavenumber side. In other words, a larger capacity were achieved when a degree of the disproportional reaction is smaller. From this tendency, it is expected that a highest capacity can be achieved from SiO which does not disproportionate. However, since pristine SiO granule is an improper size (diameter: 2−3 mm) for utilizing as an active material, the author pounded it in a mortar and prepared an electrodes composed of its ground SiO granule.

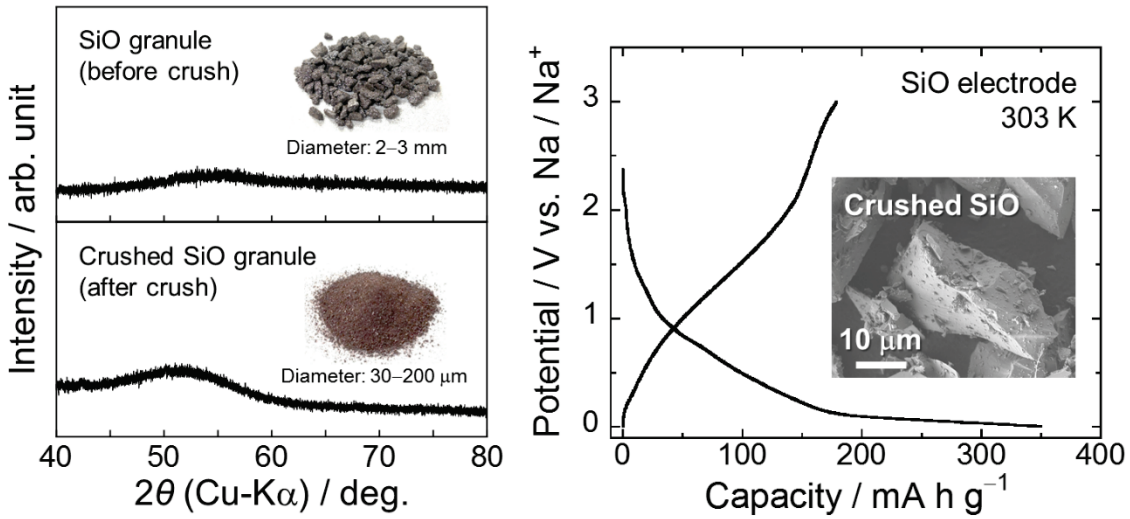

Figure 6-6. (a) XRD patterns of SiO granule before and after grinding treatment. The optical images are inserted. (b) Initial charge−discharge profile of electrode composed of ground SiO granule. (Electrolyte: 1.0 M NaTFSA/PC, Potential: 0.005−3.000 vs. Na/Na^+, Current density: 50 mA g^{-1})

The electrode showed a reversible capacity of 180 mA h g^{-1} at the first cycle (Figure 6-6), which was greater than any other electrode excluding the 10 min-milling electrode. The relatively small capacity is attributed mainly to its large particle size of ground SiO granule (diameter: 30−200 μm). Considering the experimental results and the characteristic of the SiO structure[138,144], possible reactions of SiO with Na are one or more of following: (i) conversion

reactions of sodium silicates such as Na_2SiO_3, Na_4SiO_4, $Na_2Si_2O_5$, and $Na_2Si_4O_9$, (ii) alloying and dealloying reactions between Na and Si finely dispersed in the SiO_4 matrix. In the case of SiO as a Li-ion battery anode, SiO_2 in its structure reacts with Li to irreversibly form Li_2O or/and Li_4SiO_4 compounds.[145] From the viewpoint of the monovalent alkali metal, the sodiation of SiO_2 is presumably an irreversible reaction as with the Li-ion battery system. On the other hand, Han *et al*. have performed an atom-level assessment of amorphous Si (*a*-Si) as a Na-ion battery anode using ab initio molecular dynamics simulations.[146] According to their calculations, *a*-Si can absorb 0.76 Na atoms per Si, and the $Na_{0.76}Si$ formed below 0.1 V vs. Na/Na^+ delivers a specific capacity of 725 mA h g^{-1}. The author therefore prepared an *a*-Si electrode by an electrochemical method, and experimentally investigated its charge−discharge behavior at a relatively high temperature (Figure 6-7).

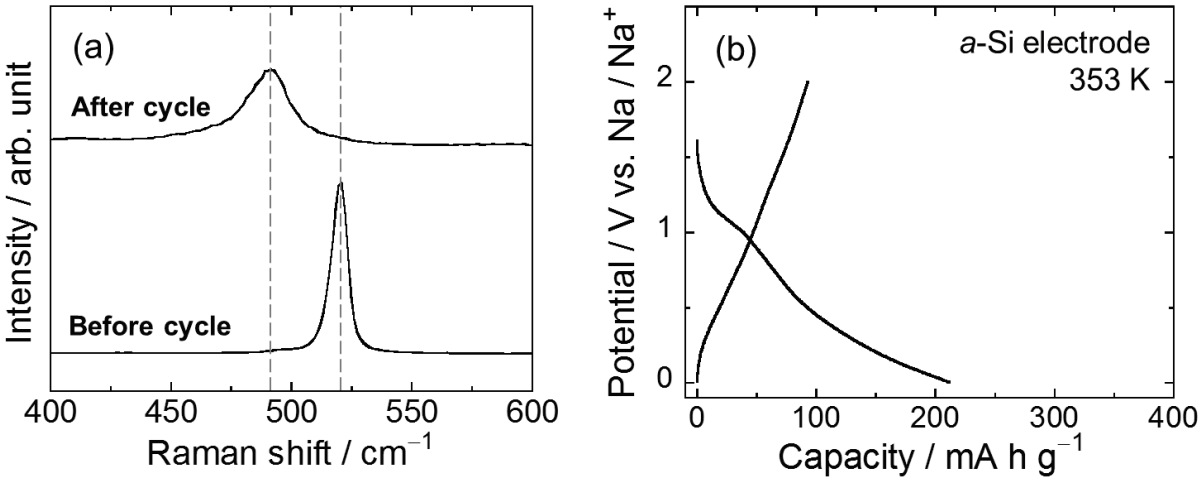

Figure 6-7. (a) Raman spectra of Si thick-film electrodes before and after two cycles in 1.0 mol dm^{-3} LiTFSA/PC at 0.12 C (420 mA g^{-1}) at 303 K. We can confirm a Raman shift from 520 to 490 cm^{-1} after Li−Si alloying and dealloying reactions, which means an amorphousization of crystalline Si. Since then, the Si electrode was separated in an argon-filled glove box, and we reassembled 2032-type coin cell consisted of the *a*-Si electrode, Na foil (counter electrode), 1.0 mol dm^{-3} NaTFSA/Py13-FSA, and propylene-based separator. (b) Initial charge−discharge (Na insertion−extraction) profiles of the *a*-Si electrode operated at 353 K. (cut-off voltage: 0.005−2.000 V vs. Na/Na^+, current density: 50 mA g^{-1})

Contrary to our expectation, the capacity of only 90 mA h g^{-1} was obtained, and it was far from the theoretical capacity calculated by Han *et al*. though the capacity is slightly larger than that of the *c*-Si electrode. This much lower utilization of the active material is probably due to the bulk property. As was mentioned before, Si in SiO structure exists as a cluster under the state of finely dispersing in SiO_4 matrix (Figure 6-8). From this, it is quite likely that the Si is activated and its reactivity to Na is enhanced.

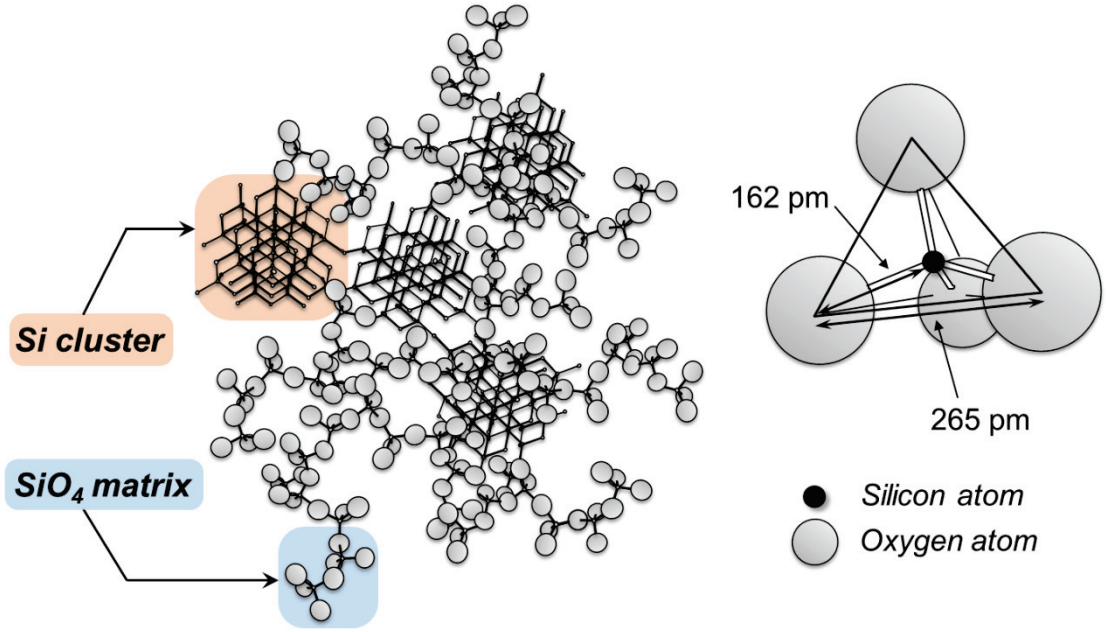

Figure 6-8. Schematic illustration of SiO with silicon clusters and SiO_2. Our group previously reported that SiO being an amorphous material is composed of three-dimensional SiO_4 tetrahedral network similar to silica (SiO_2) glass and metallic Si clusters, and that the Si clusters are finely dispersed in the SiO_4 matrices.

In order to investigate a correlation between crystallite sizes of Si and reversible capacities obtained from the SiO electrodes, the sizes of Si in SiO were calculated from respective peak width of (331) plane in XRD patterns measured at a scan rate of 0.2° min^{-1} (Figure 6-9). Figure 6-10 shows the correlation between initial capacities and MM times to SiO powder. The

reversible capacity tends to decrease with the MM processing times. An important point to be emphasized is that the capacities of the SiO electrodes become larger when the crystallite size of Si is smaller, as shown in Figure 6-4b, which indicates that dispersed Si in SiO_4 matrix reacts with Na to electrochemically form Na−Si binary alloy. At the same time, from the increase in the crystallite size of Si by the mechanical milling, the author considers that Si which existed as a cluster gradually agglutinated to become a bulk state and thereby reduced the activity against Na. Incidentally, the crystallite size of pure Si was 44 nm.

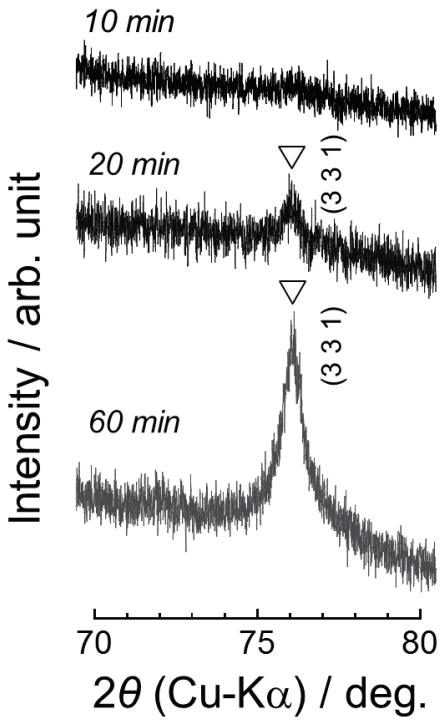

Figure 6-9. XRD patterns within the range of 70−80° of SiO powders prepared by mechanical milling for 10 min, 20 min, and 60 min. (scan rate: 0.2° min^{-1}) Because peak positions of Si in lower angle side are close to those of SiO_2, the crystallite sizes of Si in SiO were calculated from the respective peak widths of (331) plane.

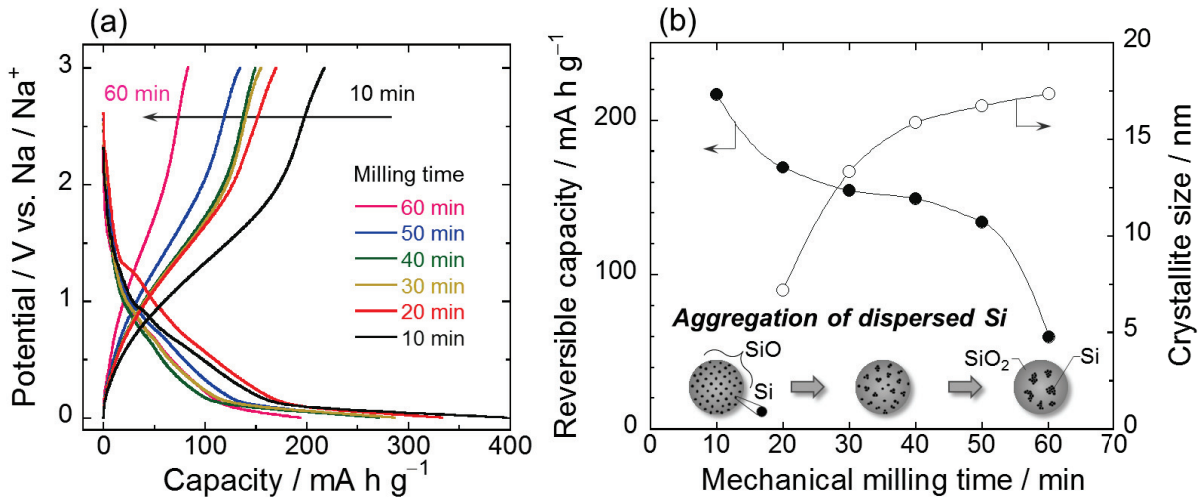

Figure 6-10. (a) Na-insertion/extraction profiles of thick-film electrodes consisted of milled SiO powders for various times. (b) Correlation between crystallite sizes of Si and reversible capacities obtained from the SiO electrodes at the first cycle. The crystallite sizes of Si were calculated from the Scherrer's equation using a peak width located at 76.4° (Si, (331) plane) in respective XRD patterns measured at a scan rate of 0.2° min^{-1}. The crystallite size of pure Si used in this study was 44 nm.

Since SiO material consists of an equimolar mixture of elemental Si and SiO_2, the weight ratio of Si to SiO_2 corresponds to 32/68 wt.%. If only the Si is assumed to be active against Na to form the $Na_{0.76}Si$ alloy, the calculated theoretical capacity of SiO is 232 mA h g^{-1} {= 725 mA h g^{-1} ($Na_{0.76}Si$) × 0.32 (weight ratio of Si in SiO)}. This value is agreement with the reversible capacity (220 mA h g^{-1}) obtained in 10 min-milling SiO electrode, which also suggests a possibility of Na−Si alloying and dealloying reactions. Although it is still unclear whether an irreversible capacity of SiO electrode during the first cycle classified into an electrolyte decomposition or an irreversible sodiation of SiO_2 such as the formation of sodium silicate, the author guesses that Si cluster in SiO reacted with Na to electrochemically form the binary alloy. The author is now working on elucidation of the reaction mechanism of SiO as a Na-ion battery anode by using XRD and Raman spectroscopy, and will report it in a future article.

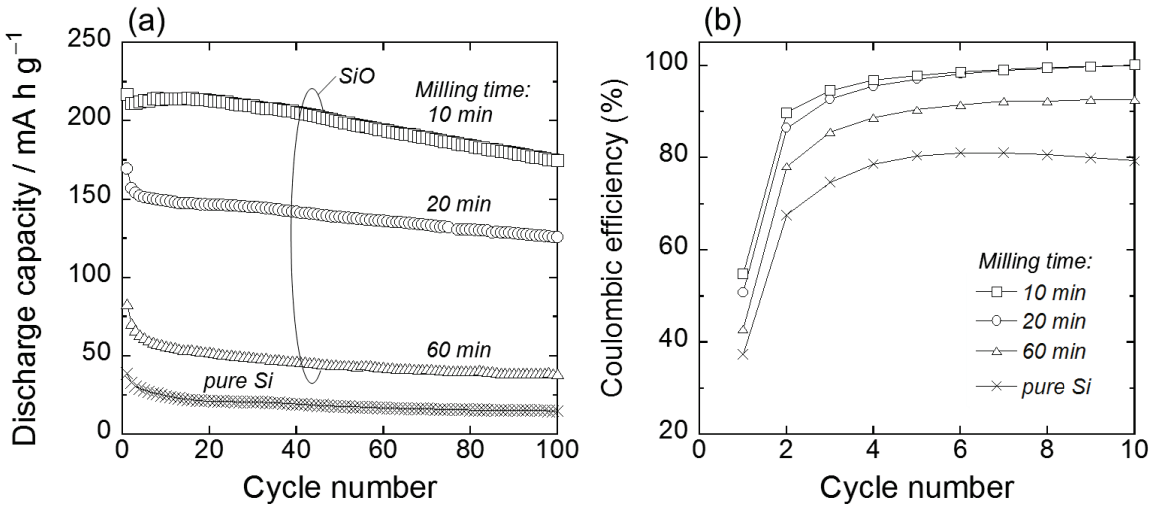

Figure 6-11. (a) Cycle performance of electrodes consisted of milled SiO powder at various times. For comparison, the performance of Si electrode was plotted. (b) Variation in coulombic efficiencies in the initial 10th cycle for their electrodes.

Figures 6-11a and 11b show dependence of discharge capacities and coulombic efficiencies on cycle number for the SiO electrodes and the Si electrode. The 10 min, 20 min, and 60 min-milling SiO electrodes exhibited discharge capacities of 170 mA h g^{-1}, 130 mA h g^{-1}, and 40 mA h g^{-1}, respectively, at the 100th cycle. In every case, the capacity retention was *ca*. 77%. These SiO electrodes showed low efficiencies within the range of 55−43% at the first cycle, but the efficiencies were improved to 100% after the ninth cycle with the exception of the 60-min milling SiO electrode. Meanwhile, the Si electrode had only ~20 mA h g^{-1} through charge−discharge cycling test. The electrodes composed of Si with a large crystallite size, 60 min-milling SiO electrode and Si electrode, showed low efficiencies below 93% and 80% until the initial tenth cycle. This behavior is assigned to continuous decomposition of electrolyte. In order to improve the cycling performance of the SiO electrode, the author searched for an optimized electrolyte from among commercially-available electrolyte products. As a result, the electrolyte consisting of NaTFSA and PC yielded the best anode property compared with those

in 1.0 M $NaPF_6$/EC:DMC (50:50 vol.%), 1.0 M NaFSA/PC, and 4.8 M NaTFSA/DME (Figure 6-12).

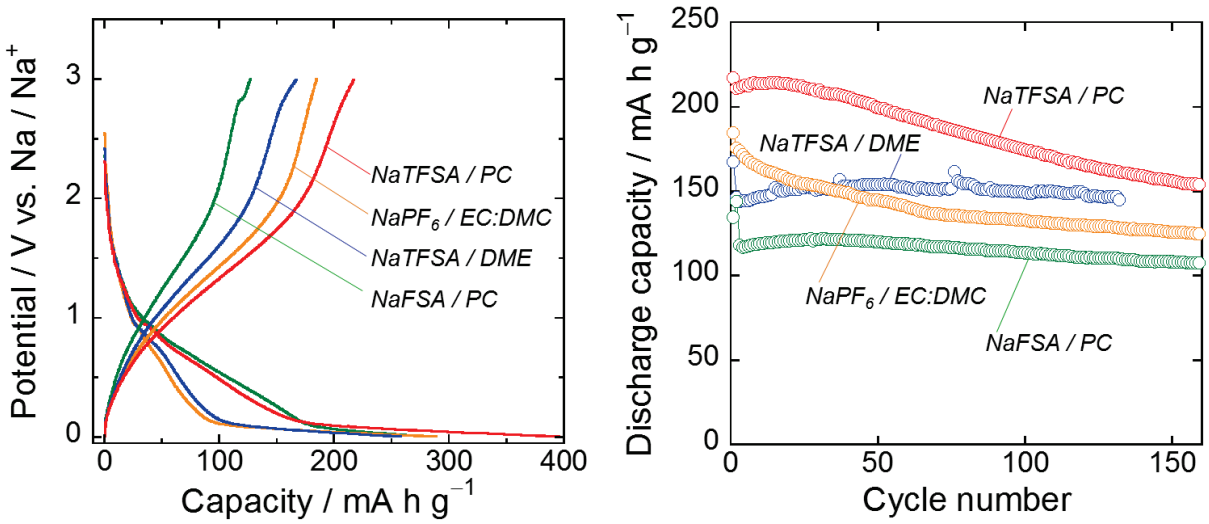

Figure 6-11. (a) Initial charge-discharge (Na insertion-extraction) profiles and (b) cycling performance of SiO thick-film electrodes in various electrolytes. The molar concentrations is 1.0 mol dm^{-3} for NaTFSA/PC, $NaPF_6$/EC:DMC (50:50 vol.%) and NaFSA/PC, and is 4.8 mol dm^{-3} for NaTFSA/DME. The cut-off voltage and current density are 0.005 to 3.000 V vs. Na/Na^+ and 50 mA g^{-1}, respectively.

6.4 Summary

The author investigated the electrochemical behavior of SiO as a Na-ion battery anode without any binder or conductive additive. It was found that SiO reacts with Na to reversibly show Na-insertion/extraction capacities. The electrode composed of SiO powder milled for 10 min exhibited the Na-extraction capacity of 220 mA h g^{-1} at the first cycle, whereas the Si electrode showed less capacity. The possible reaction mechanism of SiO with Na is following: finely dispersed Si in the SiO_4 matrix, the Si having high activity in comparison to bulk Si, absorbs Na to form Na−Si binary alloy. The 10 min-milling SiO electrode delivered the capacity of 170 mA h g^{-1} at the 100th cycle with the high capacity retention of 77%, which

indicates that SiO is a promising candidate as an active material for NIB. To realize a further increase in capacity of Si-based electrode, the use of an *a*-Si with a small grain would be effective.

Chapter 7

Novel Negative-Electrode Materials for Na-ion Batteries 3: Electrochemical Sodiation/Desodiation Properties of Tin Phosphide (Sn_4P_3, SnP_3)

7.1 Introduction

For a further high capacity, elemental phosphorous (P)[147] and tin (Sn)[118] are promising candidates of anode materials because these elements show high theoretical capacities (P, 2596 mA h g^{-1}; Sn, 847 mA h g^{-1}) based on alloying/dealloying reactions. Negative electrodes consisting of elemental P or Sn, however, generally show deterioration of an active material layer and a resulting capacity decay by several ten cycles because these elements exhibit significant volume increase in their Na-storage ($Na_{15}Sn_4$, 525%; Na_3P, 490%).

Some researchers have developed Sn_4P_3 anodes.[148–150] It has been recently reported that Sn_4P_3 showed a synergistic Na-storage reaction where Sn and P atoms can react with Na to form $Na_{15}Sn_4$ and Na_3P, and that the resulting $Na_{15}Sn_4$ alloy acts as a conducting pathway to activate the reversible Na-storage reaction of nonconductive Na_3P particles while the well-dispersed Na_3P phase provides a shield matrix to prevent the aggregation of the $Na_{15}Sn_4$/Sn nanoparticles.

As new Na-ion battery (NIB) negative-electrode materials, the author has developed SnO,[151] SiO,[152] and TiO_2(rutile)[153] ,as shown in chapter 5 and 6. On the other hand, the author has demonstrated a utility of an ionic liquid electrolyte for a high-capacity silicon negative-electrode in Li-ion batteris (LIB): the ionic liquid electrolyte offered a better cycling performance of the Si electrode by more homogeneous surface layer generated by its cathodic decomposition compared with that of a conventional organic-based electrolyte (chapter 4). In this chapter, the author investigated Na-insertion/extraction properties of Sn_4P_3 and SnP_3 electrodes in an organic electrolyte, and tried to improve the performance by applying the ionic liquid electrolyte.

7.2 Experimental Details

Active material powders of Sn_4P_3 and SnP_3 were prepared by a mechanical alloying (MA) method using commercially available tin (325 mesh, 99.99%, Kojundo Chemical Lab. Co., Ltd.) and amorphous red phosphorous (98.0%, Wako Pure Chemical Industries, Ltd.) with weight ratios of 4:3 and 1:3, respectively. The mixtures of tin and phosphorous powders were put in a stainless steel vessel together with balls so that the weight ratio of the active material and the balls was 1:30. The vessel used was sealed to keep an atmosphere of dry argon gas. The MA was carried out by using a high-energy planetary ball mill (P-6, Fritsch) for 10 h with a rotation speed of 380 rpm at room temperature to obtain Sn_4P_3 and SnP_3 powders. In this chapter, the author could not synthesized other binary alloys such as SnP and Sn_3P. For comparison, a black phosphorus powder was also prepared via MA from the red phosphorus powder. A commercial Sn powder (325 mesh, 99.99%, Kojundo Chemical Lab. Co., Ltd.) alone was also used as an active material. The crystal structure of the powders was confirmed by using X-ray diffraction (XRD, Ultima IV, Rigaku).

Thick-film electrodes were prepared by a gas-deposition (GD) method.

Na-insertion/extraction properties of electrodes consisted of Sn_4P_3 and SnP_3 were evaluated in 2032-type coin cells. The author assembled the electrodes as a working electrode, Na metal sheets (99.8%, Rare Metallic) as the counter electrode, and sodium bis(trifluoromethanesulfonyl)amide (NaTFSA, Kishida Chemical Co., Ltd.) dissolved in propylene carbonate (PC, $C_4H_6O_3$; Kishida Chemical Co., Ltd.) at a concentration of 1.0 M as the electrolyte. Galvanostatic charge−discharge tests were carried out using an electrochemical measurement system (HJ-1001 SM8A, Hokuto Denko Co., Ltd.) at 303 K with potential ranges of 0.005–2.000 V vs. Na/Na^+. The current densities were set to be 50 mA g^{-1}. In addition, the electrochemical properties of the Sn−P electrodes in ionic liquid electrolytes were also studied. The author used two kinds of ionic liquid electrolytes, 1.0 M NaTFSA-dissolved in *N*-methyl-

N-propylpyrrolidinium bis(fluorosulfonyl)amide (Py13-FSA) and 1-ethyl-3-methylimidazolium bis(fluorosulfonyl)amide (EMI-FSA).

The MA, the GD, and the cell assembly were performed throughout in a purge-type glove box (Miwa MFG, DBO-2.5LNKP-TS) filled with an argon atmosphere in which an oxygen concentration and a dew point have been maintained below 1 ppm and −100°C, respectively.

7.3 Results and Discussion

Figure 7-1 shows the galvanostatic charge (sodiation) and discharge (desodiation) potential profiles of the Sn_4P_3 and SnP_3 electrodes in the conventional organic electrolyte (NaTFSA/PC) at the first cycles. For comparison, the figure shows the results for the electrodes of black-P and Sn. The initial discharge capacity was increased with increasing the composition ratio of P in the active materials. The Sn_4P_3 and SnP_3 electrodes exhibited initial capacities larger than 250−300 mA h g^{-1}, typical capacities obtained for hard carbon-based electrodes.[27−32] Potential shoulders at 0.2−0.5 V and 0.5−1.2 V in the discharge profiles probably originate from desodiation reactions of Na−Sn and Na−P phases, respectively. It is suggested that the tin phosphides underwent a phase separation into Sn and P in the charge reaction at the first cycle.

To elucidate the mechanism, the author performed *ex-situ* XRD measurement for the Sn_4P_3 electrode during the first charge−discharge reactions (Figure 7-2). Sharp peaks at 21.6° and 31.5° were caused by an organic protective film covering the electrode surface. In the charge process, the diffraction peaks of Sn_4P_3 disappeared. New diffraction peaks, appeared at around 19.0° and 33.0°, can be possibly attributed to $Na_{15}Sn_4$ phase (Inorganic Crystal Structure Database, ICSD No.03-065-2166). At the fully discharged state at 2.0 V vs. Na/Na^+, the author could not observed Sn_4P_3, Sn, and P, indicating the amorphization of Sn and P. According to the reaction mechanism reported by Yang *et al.*,[148] the author considers that the Sn_4P_3 electrode probably showed charge−discharge reactions described as following equations:

(Sodiation at the first cycle) $Sn_4P_3 + 24Na^+ + 24e^- \rightarrow Na_{15}Sn_4 + 3Na_3P$ (1)

(Sodiation/desodiation at the subsequent cycles) $Na_{15}Sn_4 \rightleftarrows 4Sn + 15Na^+ + 15e^-$ (2)

$Na_3P \rightleftarrows P + 3Na^+ + 3e^-$ (3)

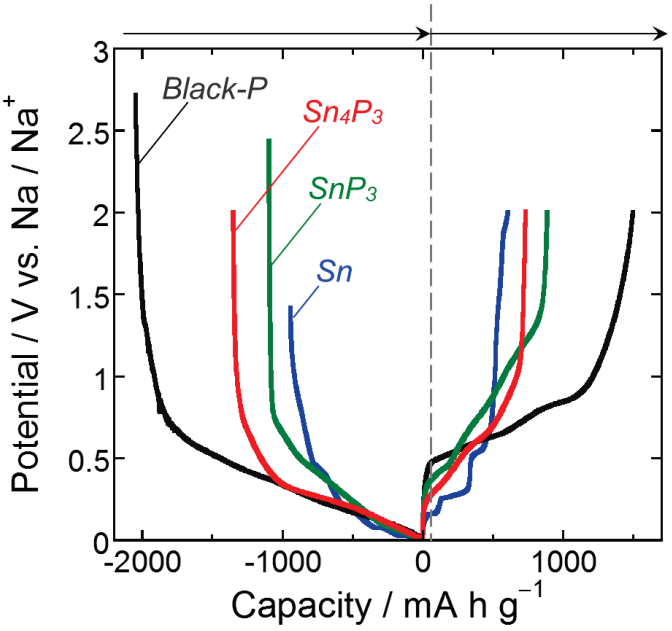

Figure 7-1. Galvanostatic charge (Na-insertion) and discharge (Na-extraction) profiles of Sn_4P_3 and SnP_3 electrodes at the first cycle under the current density of 50 mA g^{-1}.

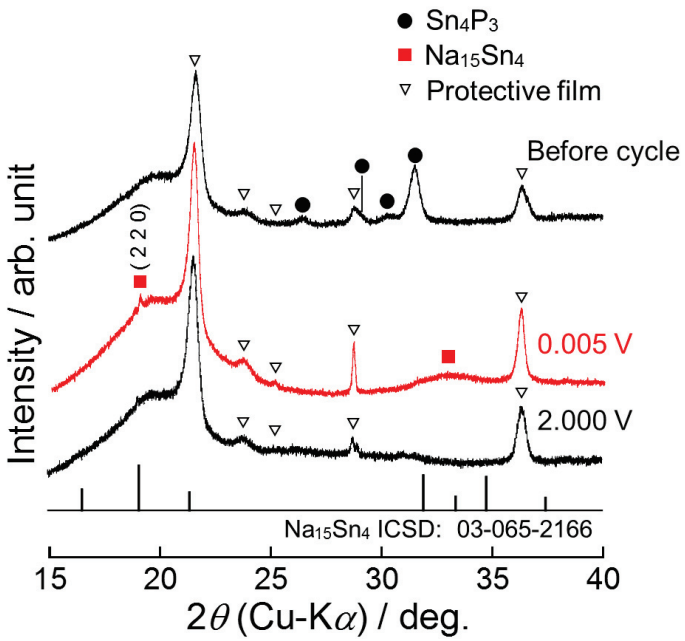

Figure 7-2. *Ex-situ* XRD patterns of the Sn_4P_3 electrode during the first cycle.

Figure 7-3 represents cycling performances of the Sn_4P_3 and SnP_3 electrodes as compared with those of electrodes using Sn alone and P alone. The discharge capacity of the Sn electrode rapidly decreased by the initial five cycles. This poor cyclability originates from the volume expansion during sodiation, the aggregation during desodiation, and the resulting deterioration of active material layer.[149] In contrast, the Sn_4P_3 and SnP_3 electrodes showed an improved cyclability. In particular, the Sn_4P_3 electrode exhibited a better performance: the capacities over 400 mA h g^{-1} was maintained until the 25th cycle. The reason for the improved cyclability is probably the complementary effects of Na-storage reactions of Sn and P in the Sn–P alloys.[148–150] $Na_{15}Sn_4$ alloy acts as a conducting pathway to activate the reversible Na storage reaction of nonconductive Na_3P particles. In addition, the well-dispersed Na_3P phase provides a shielding matrix to prevent the aggregation of Sn. Nevertheless, a capacity decay was observed after the 26th cycle, which is similar to that of the P electrode. These results were presumably caused by large volumetric changes of P during sodiation and desodiation.

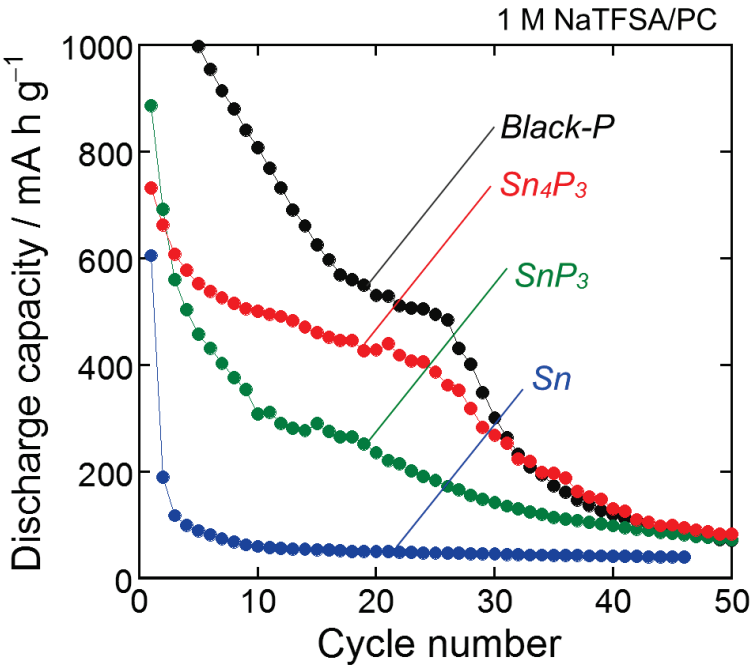

Figure 7-3. Cycling performances of the Sn_4P_3 and SnP_3 electrodes in conventional organic electrolyte (NaTFSA/PC). For comparison, the results of black-P and Sn electrodes were also shown in the figure.

For a Si negative-electrode for LIB having a high theoretical capacity and large volumetric changes during charge/discharge, in chapter 4, the author revealed that certain ionic liquid electrolyte is very effective to improve its cycling performance.[127] In a conventional organic electrolyte, a thick surface layer with inhomogeneous thickness was formed on the electrode. This leads to intensive Li-insertion/extraction reactions on specific regions coated with thinner layer and an accelerated deterioration of Si active material layer.[127] On the other hand, the intensive reactions and the deterioration were effectively suppressed in an ionic liquid electrolyte because a uniform-thickness surface layer was formed due to its high electrochemical stability.[127] Expecting similar improvement in the performance, the author applied two kinds of ionic liquid electrolytes to the Sn_4P_3 electrode.

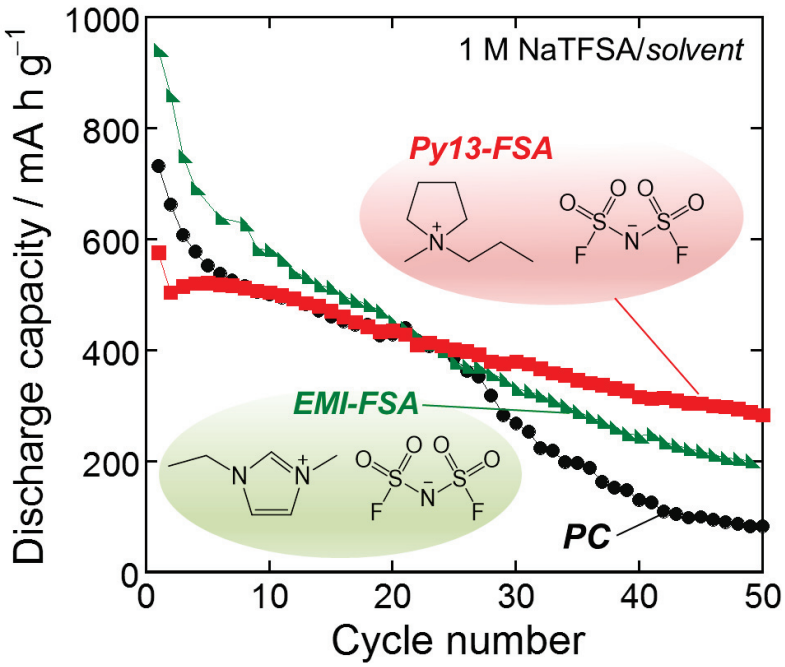

Figure 7-4. Cycling performances of the Sn_4P_3 and SnP_3 electrodes in conventional organic electrolyte (NaTFSA/PC). For comparison, the results of black-P and Sn electrodes are also shown in the figure.

Figure 7-4 shows dependence of discharge capacities on cycle numbers for the Sn_4P_3 electrodes in ionic liquid electrolytes using Py13-FSA and EMI-FSA. The capacity fading was relatively suppressed by using EMI-FSA. In case of Py13-FSA, the cyclability was further improved: the capacity of 280 mA h g^{-1} was attained at the 50th cycle. As the author expected, the ionic liquid electrolytes probably formed thin and uniform surface layers. This consideration is supported by higher initial Coulombic efficiencies of the ionic liquids (Py13-FSA: 78%, EMI-FSA: 75%) compared with the organic electrolyte (PC: 54%). With respect to EMI-FSA, it is suggested that the cathodic decomposition of EMI cation occurs by an initial attack on an acidic proton attached to the ring carbon between two nitrogen, which leads to a successive alkylation of the ring even after the second cycle and the resulting performance degradation. The superiority of Py13-based electrolyte to EMI-based electrolyte has been confirmed for Si-based LIB negative-electrodes.[54,55] In addition to this, Nohira and Hagiwara *et al.* have reported that Py13-FSA is useful for $NaCrO_2$ cathode.[154] These results indicate that Py13-FSA can improve the performance because it probably forms thin and uniform surface layer to allow uniform sodiation/desodiation reactions on the electrode.

7.4 Summary

The author prepared the Sn_4P_3 and SnP_3 electrodes by using the MA method and the following GD method, and investigated their Na-insertion/extraction properties as NIB anodes. These electrodes showed larger initial reversible capacities in the conventional organic electrolyte than the capacity of 250−300 mA h g^{-1} obtained for hard carbon-based electrodes. The formation of $Na_{15}Sn_4$ phase was suggested for the sodiation state of the Sn_4P_3 electrode. The Sn_4P_3 and SnP_3 electrodes showed better cycling performances compared with the electrode of Sn alone. The improvements in the performances are probably attributed to complementary effects of $Na_{15}Sn_4$ and Na_3P formed in the electrodes on sodiation/desodiation reactions of Sn and P: $Na_{15}Sn_4$ alloy acts as a conducting pathway to activate the reversible

sodiation of nonconductive Na_3P particles, while the well-dispersed Na3P phase provides a shield matrix preventing Sn aggregation. The performance of the Sn_4P_3 electrode was further improved by using the ionic liquid electrolytes because of the uniformly formed surface layer and the resulting uniform sodiation/desodiation reactions on the electrode.

Chapter 8

Application of Ionic Liquid Electrolyte to Phosphorus-based Negative-Electrodes for Na-ion Batteries toward Increasing in Energy Density and Ensuring of High Safety

8.1 Introduction

Despite the growing interests in NIB, an issue involving the development of high-capacity Na-storage anode materials to be solved remains to further increase the energy density of the battery. Black phosphorus has attracted much attention as an anode material because of its high theoretical capacity of 2596 mA h g^{-1}.[132,149] The theoretical capacity is about ten times larger than that of carbon-based materials[27], and is the highest value in previously-reported active materials such as Sn (847 mA h g^{-1})[118], Sb (660 mA h g^{-1})[130], and Pb (485 mA h g^{-1})[143]. Although phosphorus can absorb three sodium atoms by a formation of a binary Na−P compound, the volumetric change ratio per phosphorus atom from P to Na_3P (fully sodiated phosphorus) corresponds to 490%, which results in the generation of high stresses and large strains in the active material. The accumulated strains cause disintegration of the phosphorus electrode, leading to a rapid capacity fading. Dou *et al*. reported that the cycling stability of a phosphorus electrode was improved using a carbon nanotube composite; a reversible capacity of 750 mA h g^{-1} was maintained after the 20th charge−discharge cycling.[155]

In the previous chapter, the author has demonstrated that an electrolyte is one of the most important factors which significantly influences electrode performances. In other words, the choice of electrolyte determines the fate of battery performance. Room-temperature ionic liquids are being intensively investigated as an electrolyte solvent for rechargeable batteries and electrochemical capacitors.[12–23] These studies are motivated by their excellent physicochemical properties of high ionic conductivity, wide electrochemical window, and non-flammability. Among these properties, the nature of non-flammability is quite beneficial for the establishment of non-flammable batteries.[156] In the studies of Li-ion batteries (chapter 1−4),

the author has exhibited that the cycling performances of Si-based electrodes are significantly improved by applying an ionic liquid to an electrolyte solvent. Furthermore, it was found that the introduction of an ether functional group into cation structure of ionic liquid effectively allows the potential high-capacity of elemental Si.[127] There has been, however, no study that tried to improve cycling performances of phosphorus electrode by utilizing ionic liquid electrolytes to the best of the author's knowledge. In this chapter, therefore, the author investigated charge−discharge properties of phosphorus electrode in room-temperature ionic liquids through the use of a thick film prepared by a gas-deposition (GD) method. In order to exactly understand an electrochemical reaction of phosphorus with Na, it is essential to carry out the electrochemical evaluation without any conductive additive or binder typically used in the general preparation of electrodes. The GD method has several advantages as follows: (1) the strong adhesion between the active material particles, as well as between the particles and the substrate, and (2) the nearly unchanged composition in a thick film formed without atomization of the raw material powder. These characteristics assist in understanding the electrochemical behavior of phosphorus in ionic liquid electrolytes. The author herein reports the applicability of ionic liquid electrolytes to a phosphorus electrode for the first time.

8.2 Experimental Details

An organic solvent of propylene carbonate (PC, $C_4H_6O_3$; Kishida Chemical Co., Ltd.) and an ionic liquid of 1-ethyl-3-methylimidazolium bis(fluorosulfonyl)amide (EMI-FSA; KANTO CHEMICAL Co., Inc.) were purchased and used without further purification. 1-((2-methoxyethoxy)methyl)-1-methylpyrrolidinium bis(fluorosulfonyl)amide (Py1MEM-FSA) was synthesized by an organic method as previously reported.[66] Their chemical structures are shown in Figure 8-1. The ionic liquids were dried in a vacuum chamber at 363 K for 24 h for removing water in advance of use. The water content of the ionic liquid was confirmed to be less than 50 ppm using a Karl-Fisher moisture titrator (Labconco Corporation, FZ-Compact).

The electrolytes were prepared by dissolving a salt of sodium bis(trifluoromethanesulfonyl)amide (NaTFSA, Kishida Chemical Co., Ltd.) in each solvent at a concentration of 1.0 mol dm^{-3} (M). The electrical conductivities of the electrolytes were measured by an electrochemical impedance instrument (CompactStat, Ivium Technologies) through the use of a cell equipped with two Pt electrodes under an argon atmosphere at various temperatures from 293 to 353 K. Fire-resistance tests for the organic and ionic liquid electrolytes were conducted by using a flash point tester (Setaflash Series: 33000-0, STANHOPE SETA LTD.). These tests were performed in line with the prescribed conditions (*Rapid equilibrium closed cup method* / International Organization for Standardization: ISO 3679:2004 and Japanese Industrial Standards: JIS K2265-2) by ISO[157] and JIS[158] Committee. First, an electrolyte sample of 4 mL was injected into a cup then sealed by an O-ring to avoid volatilization. After the sample cup was heated to the set temperatures and kept at the constant temperatures for two minutes, a test jet flame with a diameter of 4 mm was dipped into the vapor space inside the sample cup from an aperture for a period of 2.5 seconds. At that moment, a flash detector distinguishes the presence or absence of an ignition to evaluate the fire resistance of the samples.

Black-phosphorus powder was simply prepared by a mechanical milling (MM) method using a high-energy planetary ball mill (Classic Line P-6, FRITSCH) in an argon atmosphere. Red-phosphorus powder (98.0%, Wako Pure Chemical Industries, Ltd.) as the starting material (2.4 g) was put in a stainless steel pot together with five stainless steel balls. The weight ratio of the balls to the red-phosphorus powder was 30:1. The MM time and rotation speed were 10 h and 380 rpm, respectively. The crystal structures and Raman spectra of the phosphorus powders were investigated using X-ray diffractometer (Ultima IV Rigaku Co., Ltd.) with CuKα radiation and Raman microscopy system (NanofinderFLEX, Tokyo Instruments, Inc.) with the 532 nm line of a Nd:YAG laser. Phosphorus thick-films were prepared on Cu foil substrates

by gas deposition using the resulting phosphorus powder (Figure 8-2) and a helium carrier gas. The author fabricated 2032-type coin cells consisting of a phosphorus thick-film electrode as the working electrode, Na foil as the counter electrode, electrolyte, and propylene-based separator. Galvanostatic charge−discharge tests were carried out using an electrochemical measurement system (HJ-1001 SD8, Hokuto Denko Co., Ltd.) in the potential range between 0.005 and 2.000 V vs. Na/Na^+ at 303 K. The current density was 50 mA g^{-1}, corresponding to a *C*-rate of 0.02 *C*. All operations including preparation of electrolytes, active material, thick-film electrodes and cell assembly were performed in a custom-made purge-type glove box (Miwa MFG, DBO-2.5LNKP-TS) filled with an argon atmosphere from which oxygen and water were completely removed. The glove box maintained a dew point below −100 ºC and oxygen content below 1 ppm. The surface morphologies of the phosphorus electrodes after the charge−discharge cycling were observed by a field-emission scanning electron microscope (FE-SEM, JSM-6701F JEOL Co., Ltd.).

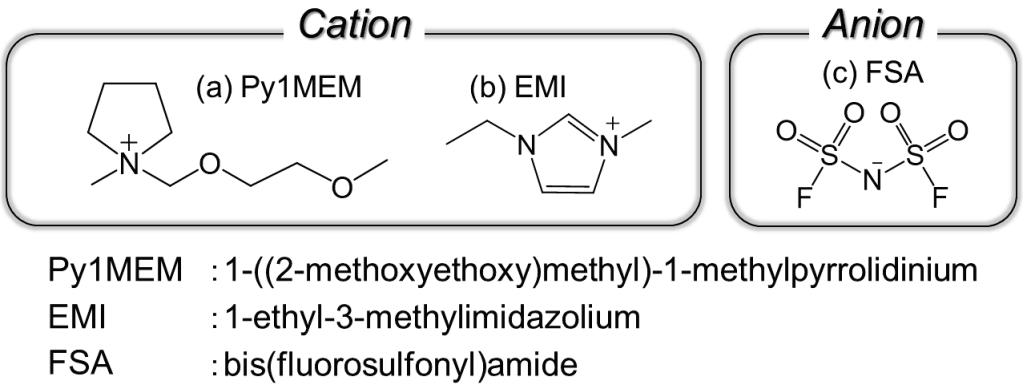

Figure 8-1. Cation and anion structures of ionic liquids used in this study. (a) 1-((2-methoxyethoxy)methyl)-1-methylpyrrolidinium (Py1MEM). (b) 1-ethyl-3-methylimidazolium (EMI). (c) bis(fluorosulfonyl)amide (FSA).

8.3 Results and Discussion

Figure 8-3 shows temperature dependence of conductivities for various electrolytes at a concentration of 1.0 M. The electrical conductivities of NaTFSA/PC, NaTFSA/Py1MEM-FSA, and NaTFSA/EMI-FSA at 303 K were 5.9, 3.4, and 10.3 mS cm^{-1}, respectively. The EMI-FSA electrolytes exhibited a higher conductivity than that in Py1MEM-FSA, which means the high ability of ionic transport in the electrolyte solution. As the positive charge in the EMI cation is non-localized, the electrostatic interaction between the EMI cation and FSA anion is weaker in comparison to that consisting of a quaternary ammonium cation and FSA anion. The charge delocalization consequently functions to reduce its lattice energy and further decreases the viscosity of the ionic liquid, which is the reason for the superior conductivity obtained from the EMI-FSA-based ionic liquid electrolyte.[16,59]

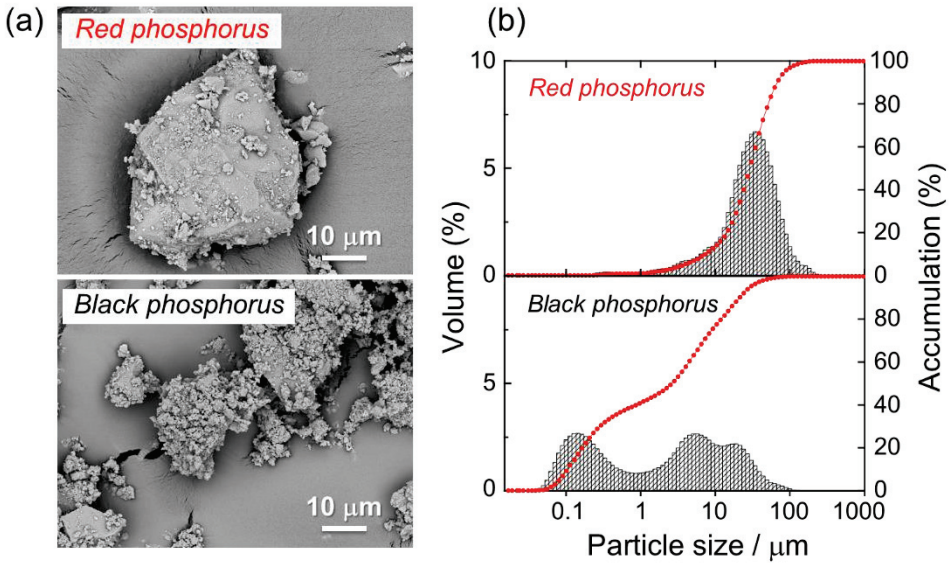

Figure 8-2. (a) FE-SEM images of red and black-phosphorus powder. (b) Particle size distributions of their powders.

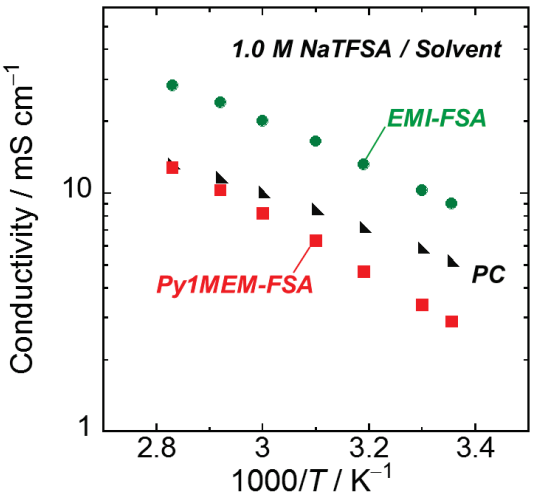

Figure 8-3. Temperature dependence of conductivity for electrolytes at a concentration of 1.0 M. The measurements were conducted in the range from 298 K to 353 K. The electrical conductivities in PC, Py1MEM-FSA, and EMI-FSA at 303 K are 5.9, 3.4, and 10.3 mS cm^{-1}, respectively.

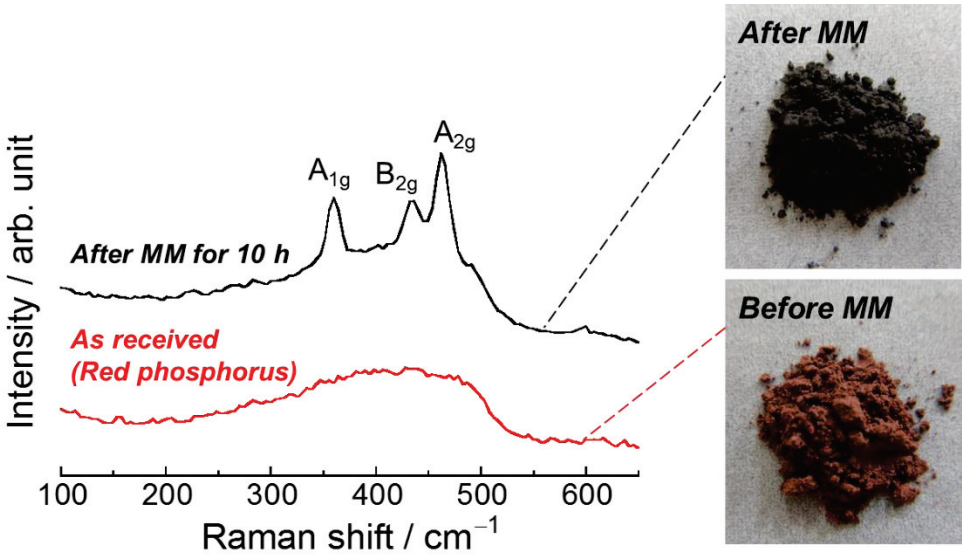

Figure 8-4. Raman spectra of red-phosphorus powder and ball-milled phosphorus powder, and their photographs.

Figure 8-4 displays Raman spectra of red-phosphorus powders before and after mechanical milling (MM) treatment for 10 h. The peaks located at 360, 434, and 461 cm^{-1} in the spectrum of the milled phosphorus are attributed to vibrations of crystalline lattice of black-phosphorus such as A_{1g}, B_{2g}, and A_{2g} phonon modes.[159] Furthermore, the black-phosphorus phase (Inorganic Crystal Structure Database, ICSD No. 01-073-1358) was detected in the milled red-phosphorus powder (Figure 8-5). Based on these results, it was clear that the target material was successfully synthesized. In addition, comparing the colors of these powders before and after the MM treatment, the author visually confirmed that the red-phosphorus had been transformed into black-phosphorus. The author employed the black-phosphorus as an active material powder because its activity against Na is higher than that of red-phosphorus.

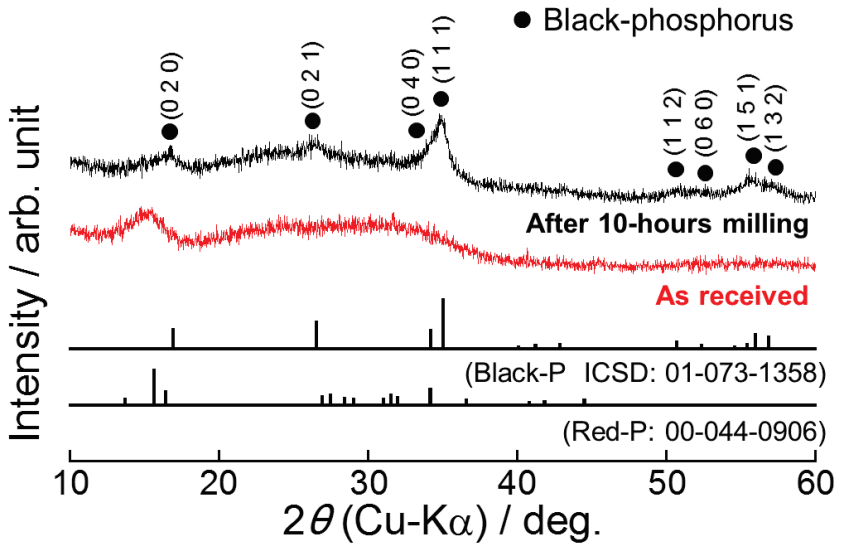

Figure 8-5. XRD patterns of red-phosphorus powder before and after mechanical milling (MM) treatment for 10 h. The milling time and rotating speed are 10 hours and 380 rpm, respectively.

Figure 8-6 shows initial charge−discharge (Na insertion−extraction) profiles of the phosphorus thick-film electrodes in 1.0 M NaTFSA-dissolved in Py1MEM-FSA or EMI-FSA. For comparison, a profile in an organic electrolyte of 1.0 M NaTFSA/PC is also shown. Among the three kinds of electrolytes, the largest discharge capacity of 1500 mA h g^{-1} was obtained when using PC. For the ionic liquid electrolytes, the capacities in Py1MEM-FSA and EMI-FSA were 800 mA h g^{-1} and 1030 mA h g^{-1}, respectively. The main reason for the relatively lower capacities in these ionic liquid electrolytes results from the strong electrostatic interaction between Na ion and FSA anions in the ionic liquid electrolytes. Since ionic liquids do not contain any neutral molecules, in the FSA-based ionic liquid electrolyte, Na ion is inevitably solvated by several FSA anions to form $[Na(FSA)_x]^{1-x}$ complex in which "x" is defined as a solvation number. With respect to ionic liquid electrolytes containing bis(trifluoromethanesulfonyl)amide (TFSA) anion, Monti *et al*. demonstrated that Na ion is solvated by three TFSA anions through oxygen atoms with two bindentate and one monodentate coordination.[160]

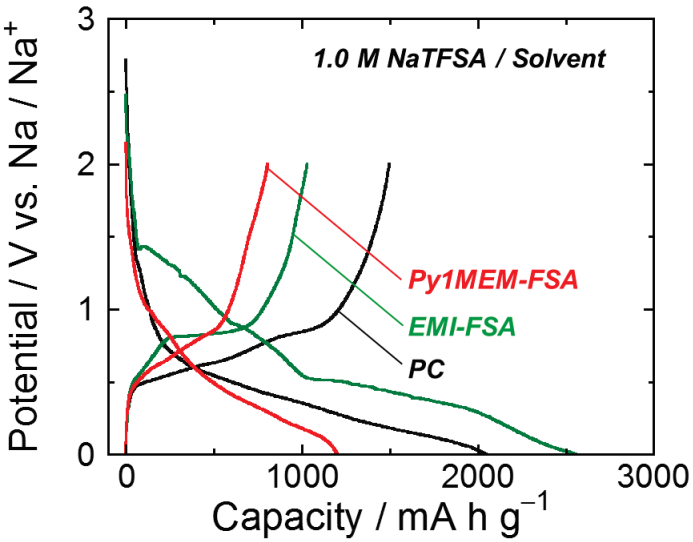

Figure 8-6. Charge−discharge (Na insertion−extraction) curves of black-phosphorus thick-film electrodes in 1.0 M NaTFSA-dissolved in EMI-FSA or Py1MEM-FSA. For comparison, the profile in PC is also shown. Current density: 50 mA g^{-1}.

Although the solvation number of the FSA anions per Na ion is not still clear, there is no doubt that the interaction between Na ion and FSA anions is much greater than that between Na ion and neutral molecules such as PC solvent. The electrostatic interaction impedes Na-insertion into a negative electrode, and as a result, the reversible capacity decreases compared to that in an organic electrolyte system with the exception of a high-temperature operation.[161] The slightly-higher reversible capacity obtained in EMI-FSA than Py1MEM-FSA originates from its higher ionic conductivity. EMI-FSA, however, delivered an extremely low coulombic efficiency of 40% at the first cycle. In the potential range from 1.43 V to 0.53 V vs. Na/Na^+ during the charge curve, the author confirmed a shoulder associated with an irreversible decomposition of the EMI cation and/or FSA anion. Due to the high activity of the hydrogen atom at the C2 position of the EMI cation, it is considered that EMI-FSA irreversibly underwent a reductive decomposition at a relatively high potential.[162] The large polarization observed in its discharge curve probably means that the Na-ion conduction through a surface layer induced by the decomposition of EMI-FSA was hard.

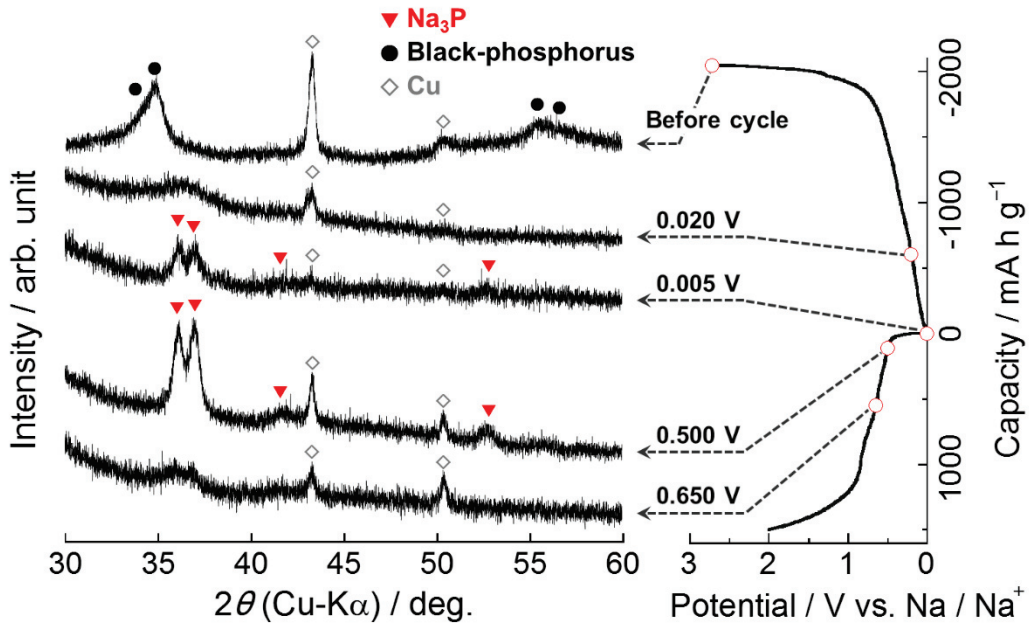

Figure 8-7. *Ex-situ* XRD patterns of phosphorus electrodes during the first charge−discharge cycle.

To investigate the reaction mechanism of phosphorus with Na during charge and discharge, the author performed *ex-situ* XRD measurements at each potential using a slurry electrode composed of black phosphorus powder (70 wt.%), acetylene carbon black (10 wt.%), and polyvinyl-alcohol binder (20 wt.%). Figure 8-7 compares the *ex-situ* XRD patterns of the phosphorus electrodes at various potentials vs. Na/Na^+. When the phosphorus electrode was electrochemically reduced to 0.200 V vs. Na/Na^+, peaks attributed to the black phosphorus disappeared, and a shoulder indicating the sodiation of phosphorus was detected at around 36.4°. Subsequently, peaks appeared at 36.1°, 37.0° and 52.7° in the fully sodiated state at 0.005 V. These peaks are attributed to the formation of hexagonal Na_3P (ICSD No. 01-073-3917). Intermediate phases, such as NaP and Na_2P, were not confirmed. This is probably because these intermediate alloy phases are amorphous as reported by other researchers.[147,163] During the electrochemical oxidation process, at the potential of 0.500 V, peaks corresponding the Na_3P phase still remained, which agrees with the charge−discharge profile obtained from the electrochemical tests. No obvious peak showing Na−P phases was confirmed at 0.65 V. In addition to this, no diffraction pattern of black phosphorus was observed after the fully desodiated state at 2.000 V (not shown here), which also indicates that phosphorus undergoes amorphization by the sodiation and desodiation processes. Based on the *ex-situ* XRD analysis, phosphorus appears to react with Na as shown in the following equations:

$$P + xNa^+ + xe^- \rightleftarrows Na_xP \qquad (1)$$

$$Na_xP + yNa^+ + ye^- \rightleftarrows Na_3P \qquad (2)$$

Figure 8-8 represents dependence of discharge (Na-extraction) capacities and coulombic efficiencies of the phosphorus electrodes in the ionic liquid and the organic electrolytes. Although the phosphorus electrode in PC showed the high discharge capacity of 1500 mA h g^{-1} for the first cycle, the capacity quickly decreased to 110 mA h g^{-1} by the 40th cycle, and thus resulted in a very poor cycling performance. The volume change ratio from P to Na_3P

phase is 490%, which is responsible for the generation of high stresses causing large strains in the active material.[132,163]

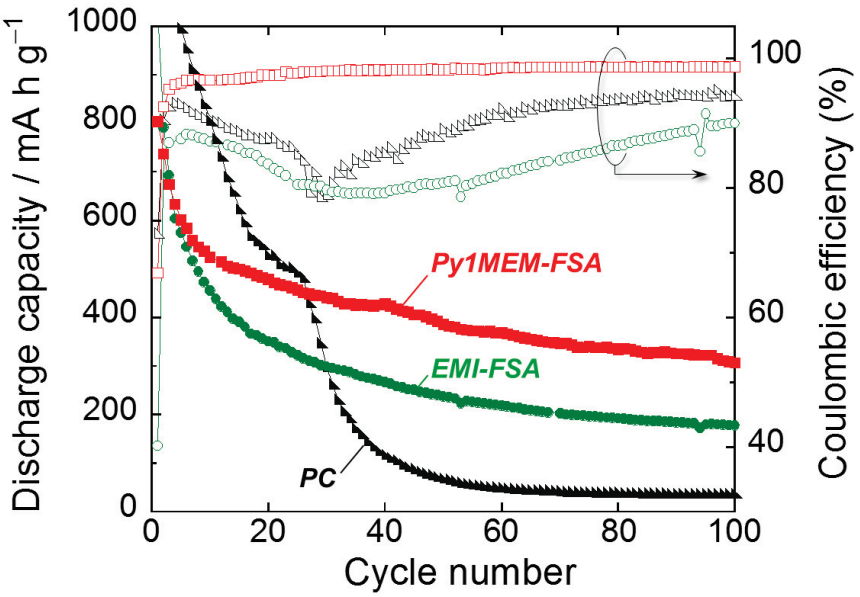

Figure 8-8. Dependence of discharge (Na-extraction) capacities and coulombic efficiencies on cycle number for black-phosphorus electrodes in various electrolytes. The initial discharge capacities in PC and EMI-FSA were 1500 and 1030 mA h g^{-1}, respectively.

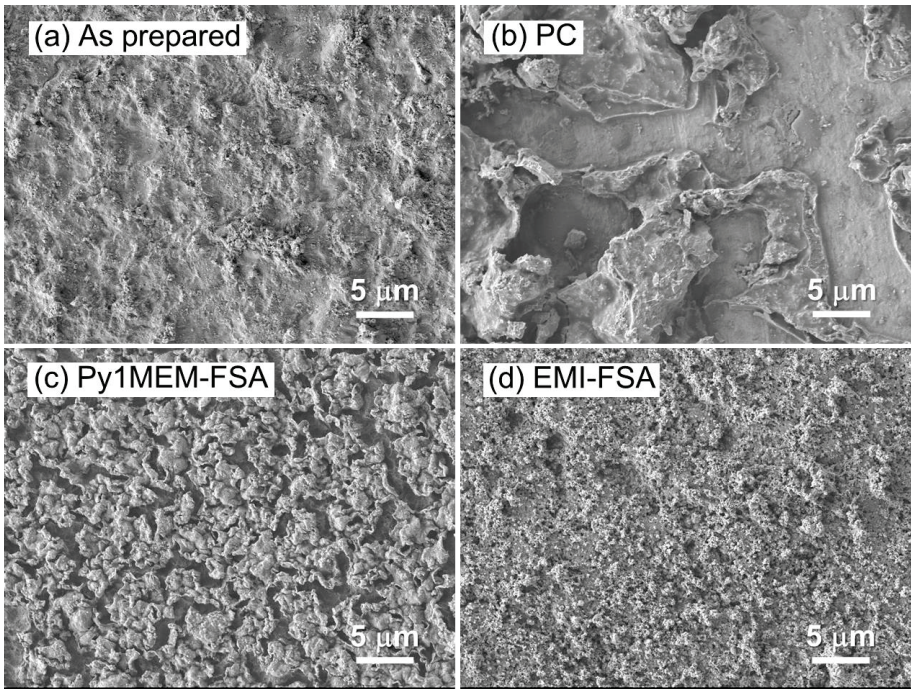

Figure 8-9. FE-SEM images of phosphorus electrodes (a) as prepared and after charge–discharge cycling in (b) PC, (c) Py1MEM-FSA, and (d) EMI-FSA.

The accumulated strains by repeated charge−discharge cycling lead to the disintegration of an electrode. In the PC-based electrolyte, the author could confirm noticeable changes in surface morphology of the phosphorus electrode and the resulting exposed Cu foil (Figure 8-9b). Organic electrolytes are generally decomposed during charge process to form a surface layer on a negative electrode. The decline in the coulombic efficiency during the initial 30th cycle in PC implies the continuous electrolyte decomposition which took place along with the disintegration of the phosphorus electrode.[132] The continuous growth of surface layer increases the resistance for Na-insertion into the phosphorus, and it reduces the reversibility and the activity for sodiation/desodiation reactions of phosphorus. The author controlled the volumetric changes in phosphorus during charge−discharge cycling tests by adjusting the amount of Na insertion−extraction with a constant capacity of 500 mA h g^{-1} (Figure 8-10), which suggests that a long cycle lifetime can be successfully achieved. Contrary to our expectation, the capacity was maintained only up to the 10th cycle, and then the capacity gradually dropped down. This result reflects that the decomposition products of the electrolyte passivated surface parts of the electrode, and thereby reduced utilization of the active material. It is inferred that the reason for the capacity decay in PC lies not only in the disintegration, but also the passivation by the surface layer on the phosphorus electrode.

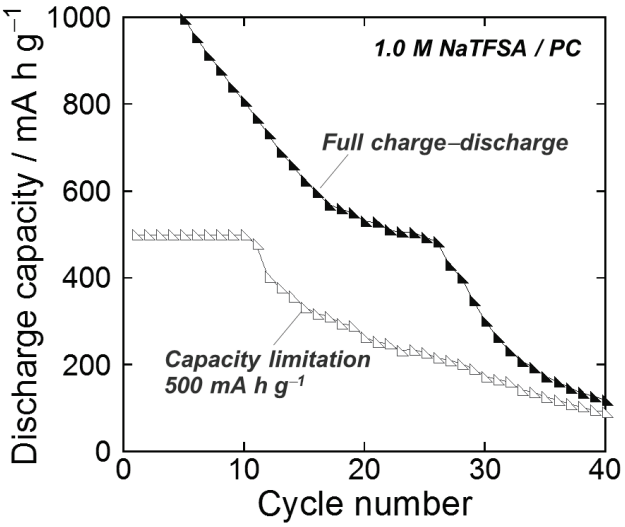

Figure 8-10. Variation in discharge (Na-extraction) capacity of phosphorus electrodes in 1.0 M NaTFSA-dissolved in PC versus cycle number for Na-insertion level fixed to 500 mA h g^{-1}. For comparison, performance without capacity limit was also plotted.

In contrast to the organic electrolyte system, Py1MEM-FSA delivered a superior cycle performance; a relatively high discharge capacity of 310 mA h g^{-1} was attained at the 100th cycle. Compared with surface morphology of both phosphorus electrodes after charge−discharge cycling (Figures 8-9b and 9c), it is obvious that, in Py1MEM-FSA, the disintegration of the electrode was significantly suppressed. Furthermore, the regions in which the disintegration occurred were not localized, but were generated over the entire electrode in comparison that in PC. The most noteworthy point is that surface morphologies markedly varied by an electrolyte solvent. In studies of the Li-ion battery, the author previously found that Li-ions are uniformly inserted into a Si electrode over the entire surface by an ionic-liquid-derived surface layer.[127] The Si electrode can reasonably avoid stress accumulation generated in localized regions, which suppresses the severe disintegration of the electrode leading to a poor cycling performance. From the SEM observations, the author considered that the mechanism of the improved performance of the Si electrode is just as valid for the phosphorus

electrode in Py1MEM-FSA, that is, the Py1MEM-FSA-derived surface layer allowed uniform Na-insertion into the phosphorus electrode. On the other hand, in EMI-FSA, the discharge capacity gradually decreased and was 180 mA h g^{-1} at the 100th cycle though the capacity was higher than that in PC. The coulombic efficiency in Py1MEM-FSA reached a value exceeding 95% after the second cycle, whereas the efficiency in EMI-FSA constantly remained below 90% throughout every cycle. This phenomenon means a side reaction such as continuous growth of a surface layer induced by the decomposition of EMI-FSA, which is the cause of the increase in the resistance for the interfacial Na-ion transfer between phosphorus electrode and EMI-FSA. Since the degree of change in the electrode surface after cycling in EMI-FSA was actually smaller than that in Py1MEM-FSA (Figure 8-9d), it is considered that the deterioration of the electrode arose from a decrease in utilization of the active material due to the surface layer formed on the anode. The investigation of the characteristics for the surface layers such as the chemical composition and thickness is a future study. Experimental results show that the selection of cation in ionic liquids has a significant influence on the cycle performance of a phosphorus electrode, and indicated that ionic liquids with cations having a high stability against cathodic decomposition are needed for achieving a long life cycle.

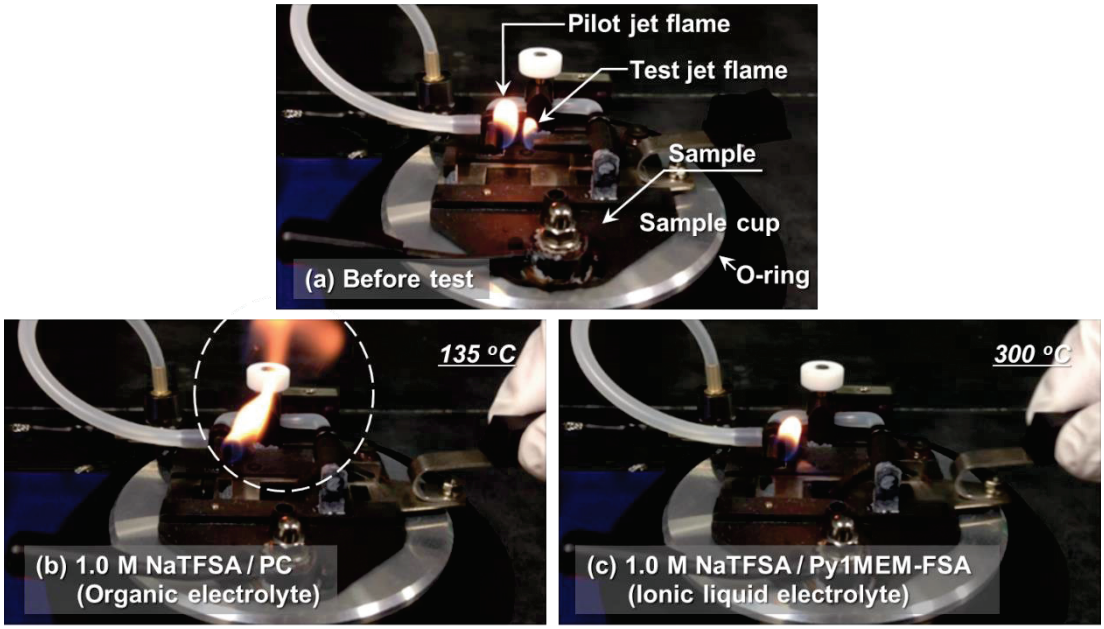

Figure 8-11. (a) Photographs of fire-resistance tester (Setaflash Series: 33000-0). Fire-resistance tests of (b) 1.0 M NaTFSA/PC (organic electrolyte) and (c) 1.0 M NaTFSA/Py1MEM-FSA (ionic liquid electrolyte).

Figure 8-11 shows fire resistance test results of the electrolytes employed in this chapter. Conventionally, the flammability of ionic liquid electrolytes has been examined by directly exposing its solution to a test flame at room temperature.[164] Although this test is a simplified evaluation method to easily understand, the vapor of its solution generated by the heat hardly reaches its combustion limitation because of an open-type measurement, and thereby results in an overestimation. On the other hand, the closed-system evaluation method (Rapid equilibrium closed cup method)[157,158] used in this chapter is prescribed by IOS-standard and JIS. The flame retardant property can therefore be evaluated with a good accuracy and reproducibility. The author, the first time, introduced this technique as the evaluation method for the flame retardancy of ionic liquid electrolytes. When using the organic electrolyte of 1.0 M NaTFSA/PC, the electrolyte ignited with a large flame at the relatively low temperature of 135

ºC (Figure 8-11b). In contrast, no fire was observed at 300 ºC (measurement limitation) in the ionic liquid electrolyte of 1.0 M NaTFSA/Py1MEM-FSA (Figure 8-11c), which clearly demonstrates the non-flammability of the ionic liquid. This characteristic contributes to the establishment of highly safe Na-ion batteries, and allows the charge−discharge reactions over a wide temperature range.

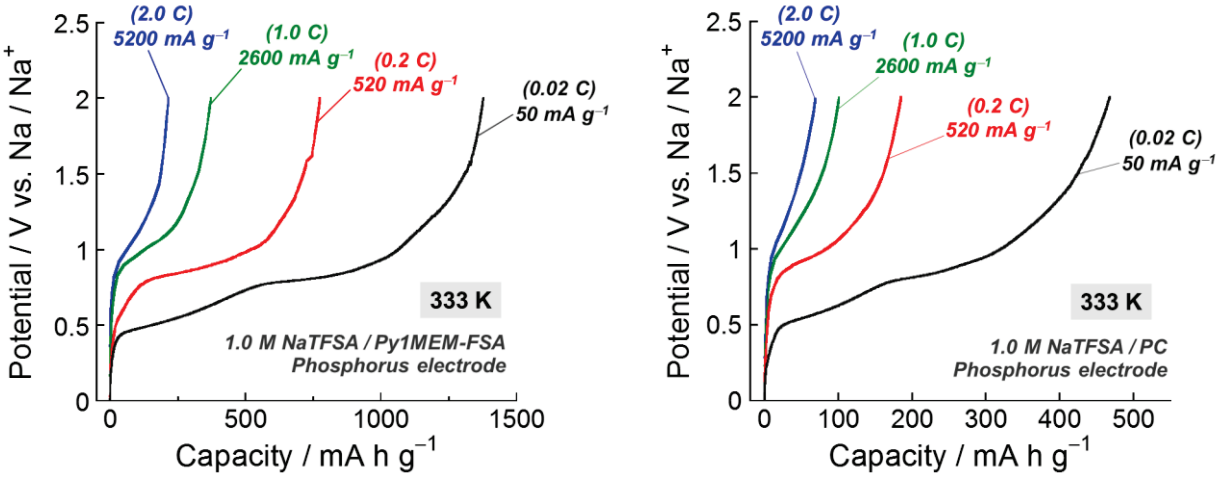

Figure 8-12. Rate capability of phosphorus electrode in 1.0 M NaTFSA/Py1MEM-FSA at 333 K. The rapid charge-discharge property was evaluated at various current densities from 50 (0.02 *C*) to 5200 mA g^{-1} (2.0 *C*).

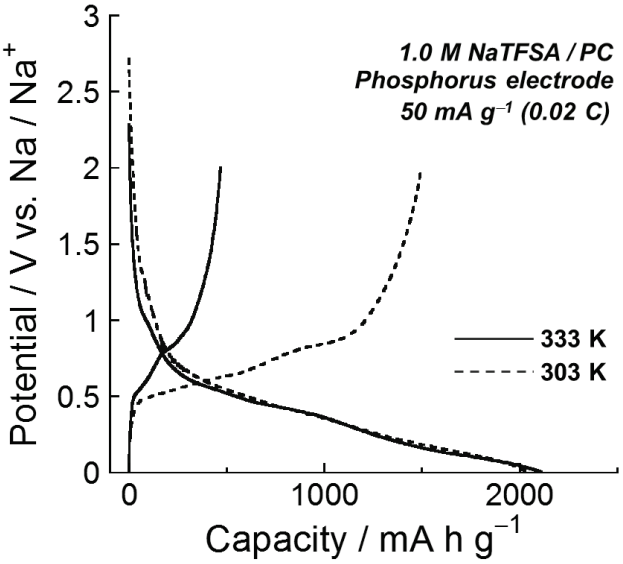

Figure 8-13. Comparison of charge-discharge profiles of phosphorus electrode in 1.0 M NaTFSA/PC at 303 K and 333 K.

Figure 8-12 exhibits a rate performance of the phosphorus electrode in Py1MEM-FSA at 60 ºC. Although the reversible capacity decreased with the increasing current density, the capacity of 1380 mA h g^{-1} was achieved at a current density of 50 mA g^{-1}, and the capacity was 1.7 times larger than that obtained at 30 ºC. This is because the ionic transport property, kinetics of the desolvation of $[Na(FSA)_x]^{1-x}$, and solid-phase diffusion were improved. The significant enhancement was confirmed only in Py1MEM-FSA, and the charge−discharge capacities in PC became small (Figure 8-13). This is considered to be due to the poor thermal stability of the electrolyte solvent itself and a surface layer formed on the negative-electrode.[165]

8.4 Summary

Black phosphorus powder was simply synthesized by mechanical milling, and phosphorus electrodes without any binder or conductive additive were prepared by a gas-deposition method using the resulting powder. For the first time, the author investigated the applicability of ionic liquid electrolytes using a phosphorus electrode as the Na-ion battery anode. The phosphorus electrode in Py1MEM-FSA exhibited the best cycling performance. The discharge capacity at the 100th cycle was 310 mA h g^{-1} with a capacity retention of approximately 40%. The good electrode property is based on its high stability against cathodic decomposition. On the other hand, an organic electrolyte, 1.0 M NaTFSA-dissolved in PC, delivered the poor cycling performance; the capacity decreased to 40 mA h g^{-1} by the 100th cycle though the electrode showed the initial high capacity of 1500 mA h g^{-1}. Based on the SEM observation results, it was revealed that the use of Py1MEM-FSA allowed the uniform Na-insertion into the phosphorus electrode surface, which avoids the disintegration of the electrode leading to a poor electrode property. In light of the low-electrochemical stability of EMI-FSA and the smallest degree of change in the electrode surface after cycling, the reason for the capacity decay in EMI-FSA is that the surface layer induced by the irreversible decomposition of it restricts Na-insertion into the electrode. In the cycling test at a relatively high temperature of 60 ºC, the

charge−discharge capacities were significantly increased only in Py1MEM-FSA which showed an excellent fire resistance. This property indicates that the application of the ionic liquid as an electrolyte solvent is an advantage for realizing a Na-ion battery combining a high energy density and a high safety.

Concluding Remarks

In this thesis, the author tried to fabricate the electrode–electrolyte interface which can enhance an electrochemical property of negative electrode for alkali-metal-ion rechargeable batteries by modifying cation structure of ionic liquid or by employing a film-forming additive. In addition, the author is suggesting novel active materials as promising Na-ion battery anodes. Main results of this work are as follows:

1. Thick-film electrode composed of only *c*-Si powder was prepared by a gas-deposition method. Electrochemical reactions of the Si electrodes in organic electrolyte including film-forming additive were investigated without commercially used conductive additive or binder. VC- and FEC-derived surface films are electrical insulating, which leads to the suppression of the additional reductive decomposition of the electrolyte. Si electrode in VC-containing electrolyte exhibited good cycle performance with the discharge capacity of 1000 mA h g^{-1} beyond 750th cycles at a constant charge capacity of 1000 mA h g^{-1}.

2. Effect of cation structure in ionic liquid on electrochemical property of Si electrode was studied. It was revealed that the introduction of ether functional group into piperidinium-cation can reduce the electrostatic interaction between Li ion and TFSA anions to promote Li-insertion into Si and therefore increase Li-insertion/extraction capacities of Si electrode at initial cycles. In spite of the enhanced initial capacity, the cycle stability of Si electrode in PP1MEM-TFSA was significantly improved in comparison with that of Si electrode in the organic electrolyte.

3. Influence of cation structure on solvation environment for Li ion in piperidinium-based ionic liquid electrolytes was studied by Raman spectroscopic measurements. The ether

group in PP1MEM cation diminished the solvation number of TFSA anion per Li ion compared to that in PP16-TFSA (PP1MEM-TFSA: 1.56, PP16-TFSA: 2.40). The less solvation number in PP1MEM-TFSA allowed the facile Li-ion diffusion in the electrolyte bulk rather than the interfacial Li-ion transfer and significantly improved rate performance.

4. Two-dimensional lithiation distribution on Si electrode surface by using Raman microspectroscopy revealed the following: In the case of using PC, unreacted Si locally remained in the electrode after cycling, and Li−Si alloying and dealloying occurred in limited regions on the electrode. On the other hand, in the ionic liquid electrolyte, Li−Si reactions uniformly took place over the entire electrode, which relatively avoided any stress accumulation leading to its disintegration. This is probably considered to be the reason why the cycle performance of the Si electrode was significantly improved by using the ionic liquid instead of the conventional electrolytes.

5. SnO was applied to an anode material for Na-ion battery, and the reaction mechanism was examined by electrochemical tests. The SnO reacted Na to show a reversible capacity of 580 mA h g^{-1} at the first cycle, which is superior to a theoretical capacity of carbon-based materials. The Na_2O which was formed by irreversible reduction of SnO at the first cycle acted as a buffer to release the stress induced by alloying and dealloying reactions of Sn with Na. FEC-derived surface layer on the electrode effectively suppressed the continuous electrolyte decomposition, and thereby resulted in an achievement of a high capacity of 250 mA h g^{-1} at the 50th cycle.

6. Na-insertion/extraction property of Si was studied for the first time through the intermediary of SiO being an amorphous material which is composed of three-dimensional

SiO_4 tetrahedral network similar to silica glass and Si clusters. The SiO electrode reacted with Na to exhibit a reversible capacity of over 200 mA h g^{-1} (678 mA h $g(Si)^{-1}$) at the first cycle, whereas Si electrode showed less capacity. The capacities of the SiO electrodes became larger when the crystallite size of Si in its SiO was smaller. Given this characteristics, it is considered that the capacity obtained from the SiO originates from an alloying reaction of the Si clusters having a high surface energy with Na.

7. Tin phosphides, Sn_4P_3 and SnP_3, were prepared using a mechanical alloying method, and their electrochemical behaviors in an organic electrolyte and ionic liquid electrolytes were evaluated. Based on the results obtained from the study of LIB, ionic liquid electrolytes were applied to the Sn_4P_3 electrode for improvement of cycling performance. Due to a uniformly formed surface layer which was derived from the ionic liquid resulted in better performance, and the electrode exhibited a reversible capacity of 280 mA h g^{-1} at the 50th cycle.

8. The electrochemical Na-insertion/extraction properties of phosphorus as a Na-ion battery anode in ionic liquid electrolytes were investigated. Py1MEM-FSA delivered a high reversible capacity of 310 mA h g^{-1} at the 100th cycle, whereas the phosphorus electrode in EMI-FSA showed a low capacity of only 110 mA h g^{-1}. The Py1MEM-FSA-based electrolyte exhibited an excellent fire resistance in comparison with the PC-based organic electrolyte, which can be an advantage for realizing a Na-ion battery with a high-energy density and a high safety.

Acknowledgments

The author would like to express his sincerest gratitude to Professor Hiroki Sakaguchi at Department of Chemistry and Biotechnology, Graduated School of Engineering, Tottori University, for his continuous guidance, invaluable suggestions, and encouragement throughout this work, and for his advice to my private life.

The author is also deeply grateful to Associate Professor Hiroyuki Usui for his fruitful comments, helpful suggestions, and kind discussions in the preparation of the articles.

The author would like to thank to Assistant Professor Yasuhiro Domi for his stimulating discussions and heartfelt advices, and his guidance of *in-situ* Raman analysis.

The author is much obliged to Professor Toshiyuki Itoh and Associate Professor Toshiki Nokami for their invaluable comments, continuous discussions, and supplying ionic liquids.

The author is gratefully indebted to Professor Rika Hagiwara, Professor Toshiyuki Nohira, and Mr. Takayuki Yamamoto at Graduate School of Energy Science, Kyoto University, for their collaboration and useful discussions.

Special thank should be given to the author's co-workers, Mr. Kazuya Yamane, Mr. Shota Morishita, Mr. Kuniaki Wasada, Mr. Takahiro Suzumura, Mr. Takuma Sakata, Mr. Kazuki Yamaguchi, Mr. Kohei Fujiwara, Mr. Sho Yoshioka, Ms. Hiroka Takahashi, Mr. Yuta Kakimoto, Ms. Ayami Sato, Mr. Kuninobu Matsumoto, Mr. Naoyuki Handa, Mr. Takuya Yamashita, and all other members of the laboratory of Professor Hiroki Sakaguchi for hearty supports and precious memories.

The author thanks Japan Society for the Promotion of Science (JSPS) for research fellowship (No. 2611485).

Finally, the author gratefully acknowledges his father, Hiromu Shimizu, his mother, Kyoko Shimizu, and his younger brother, Takahiro Shimizu.

References

[1] M.N. Obrovac, L. Christensen, *Electrochem. Solid-State Lett.*, **7** (5) (2004) A93–A96.

[2] T.D. Hatchard, J.R. Dahn, *J. Electrochem. Soc*., **151** (6) (2004) A838–A842.

[3] M. Galinski, A. Lewandowski, I. Stepniak, *Electrochim. Acta,* **51** (2006) 5567–5580.

[4] V. I. Pârvulescu, C. Hardacre, *Chem. Rev.,* **107** (2007) 2615–2665.

[5] N. V. Plechkova, K. R. Seddon, *Chem. Soc. Rev*., **37** (2008) 123–150.

[6] P. Hapiot, C. Lagrost, *Chem. Rev.*, **108** (2008) 2238–2264.

[7] S. Kuwabata, T. Tsuda, T. Torimoto, *J. Phys. Chem. Lett*., **1** (2010) 3177–3188.

[8] T. Torimoto, T. Tsuda, K. Okazaki, S. Kuwabata, *Adv. Mater*., **22** (2010) 1196–1221.

[9] Z. Ma, J. Yu, S. Dai, *Adv. Mater*., **22** (2010) 261–285.

[10] H. Wang, G. Gurau, R. D. Rogers, *Chem. Soc. Rev*., **41** (2012) 1519–1537.

[11] X. Sun, H. Luo, S. Dai, *Chem. Rev*., **112** (2012) 2100–2128.

[12] M. Armand, F. Endres, D. R. MacFarlane, H. Ohno, B. Scrosati, *Nat. Mater.*, **8** (2009) 621–629.

[13] D. Molina Piper, T. Evans, K. Leung, T. Watkins, J. Olson, S. C. Kim, S. S. Han, V. Bhat, K. H. Oh, D. A. Buttry, S. H. Lee, *Nat. Commun.*, **6** (2015) 6230.

[14] H. Matsumoto, H. Sakaebe, K. Tatsumi, *J. Power Sources*, **146** (2005) 45–50.

[15] H. Sakaebe, H. Matsumoto, K. Tatsumi, *J. Power Sources*, **146** (2005) 693–697.

[16] H. Matsumoto, H. Sakaebe, K. Tatsumi, M. Kikuta, E. Ishiko, M. Kono, *J. Power Sources*, **160** (2006) 1308–1313.

[17] S. Tsuzuki, W. Shinoda, M. Matsugami, Y. Umebayashi, K. Ueno, T. Mandai, S. Seki, K. Dokko, M. Watanabe, *Phys. Chem. Chem. Phys*., **17** (2014) 126–129.

[18] K. Yoshida, M. Nakamura, Y. Kazue, N. Tachikawa, S. Tsuzuki, S. Seki, K. Dokko, M. Watanabe, *J. Am. Chem.Soc*., **133** (2011) 13121–13129.

[19] K. Tsunashima, M. Sugiya, *Electrochem. Commun*., **9** (2007) 2353–2358.

[20] K. Tsunashima, Y. Ono, M. Sugiya, *Electrochim. Acta*, **56** (2011) 4351–4355.

[21] T. Sugimoto, Y. Atsumi, M. Kikuta, E. Ishiko, M. Kono, M. Ishikawa, *J. Power Sources*, **189** (2009) 802–805.

[22] A. Lewandowski, A. Świderska-Mocek, *J. Power Sources*, **194** (2009) 601–609.

[23] R. Furuya, N. Tachikawa, K. Yoshii, Y. Katayama, T. Miura, *J. Electrochem. Soc*., **162** (2015) H634–H637.

[24] S. Komaba, W. Murata, T. Ishikawa, N. Yabuuchi, T. Ozeki, T. Nakayama, A. Ogata, K. Gotoh, K. Fujiwara, *Adv. Funct. Mater*., **21** (2011) 3859–3867.

[25] N. Yabuuchi, K. Kubota, M. Dahbi, S. Komaba, *Chem. Rev.*, **114** (2014) 11636−11682.

[26] D.A. Stevens, J.R. Dahn, *J. Electrochem. Soc*., **147** (2000) 1271−1273.

[27] R. Alcántara, P. Lavela, G.F. Ortiz, J.L. Tirado, R. Menéndez, R. Santamaría, J.M. Jiménez-Mateos, *Carbon*, **41** (2003) 3003−3013.

[28] N. Adhoum, J. Bouteillon, D. Dumas, J.C. Poignet, *Electrochim. Acta.*, **51** (2006) 5402−5406.

[29] J. Zhao, L. Zhao, K. Chihara, S. Okada, J.-i. Yamaki, S. Matsumoto, S. Kuze, K. Nakane, *J. Power Sources*, **244** (2013) 752−757.

[30] M. Dahbi, T. Nakano, N. Yabuuchi, T. Ishikawa, K. Kubota, M. Fukunishi, S. Shibahara, J.-Y. Son, Y.-T. Cui, H. Oji, S. Komaba, *Electrochem. Commun*., **44** (2014) 66−69.

[31] E. Irisarri, A. Ponrouch, M.R. Palacin, *J. Electrochem. Soc*., **162** (2015) A2476−A2482.

[32] K. Kubota, S. Komaba, *J. Electrochem. Soc*., **162** (2015) A2538−A2550.

[33] C. J. Wen, R. A. Huggins, *J. Solid State Chem*., **37** (1981) 271−278.

[34] M. N. Obrovac, L. J. Krause, *J. Electrochem. Soc*., **154** (2007) A103− A108.

[35] N. Ding, J. Xu, Y. X. Yao, G. Wegner, X. Fang, C. H. Chen, I. Lieberwirth, *Solid State Ionics*, **180** (2009) 222−225.

[36] J. Xie, N. Imanishi, T. Zhang, A. Hirano, Y. Takeda, O. Yamamoto, *Mater. Chem. Phys*., **120** (2010) 421−425.

[37] M. Thakur, S. L. Sinsabaugh, M. J. Isaacson, M. S. Wong, S. L. Biswal, *Sci. Rep*., **2** (2012) 795.

[38] A. Magasinski, P. Dixon, B. Hertzberg, A. Kvit, J. Ayala, G. Yushin, *Nat. Mater*., **9** (2010) 353−358.

[39] Y. Chen, S. Zeng, J. Qian, Y. Wang, Y. Cao, H. Yang, X. Ai, *ACS Appl. Mater. Interfaces*, **6** (2014) 3508−3512.

[40] C. Wang, H. Wu, Z. Chen, M. T. McDowell, Y. Cui, Z. Bao, *Nature Chem*., **5** (2013) 1042 −1048.

[41] K. Xu, *Chem. Rev*., **114** (2014) 11503−11618

[42] I. A. Profatilova, C. Stock, A. Schmitz, S. Passerini, M. Winter, *J. Power Sources*, **222** (2013) 140−149.

[43] M.-Q. Li, M.-Z. Qu, X.-Y. He, Z.-L. Yu, *Electrochim. Acta*, **54** (2009) 4506−4513.

[44] F. Maroni, R. Raccichini, A. Birrozzi, G. Carbonari, R. Tossici, F. Croce, R. Marassi, F. Nobili, *J. Power Sources*, **269** (2014) 873−882.

[45] Z. Jiang, C. Li, S. Hao, K. Zhu, P. Zhang, *Electrochim. Acta*, **115** (2014) 393−398.

[46] A. Bordes, K. Eom, T. F. Fuller, *J. Power Sources*, **257** (2014) 163−169.

[47] V. Etacheri, O. Haik, Y. Goffer, G. A. Roberts, I. C. Stefan, R. Fasching, D. Aurbach, *Langmuir*, **28** (2012) 965−976.

[48] X. Wang, L. Sun, R. A. Susantyoko, Y. Fan, Q. Zhang, *Nano Energy*, **8** (2014) 71−77.

[49] G.-B. Han, M.-H. Ryou, K. Y. Cho, Y. M. Lee, J.-K. Park, *J. Power Sources*, **195** (2010) 3709−3714.

[50] G.-B. Han, J.-N. Lee, J. W. Choi, J.-K. Park, Electrochim. Acta, 56 (2011) 8997.

[51] Y. Domi, M. Ochida, S. Tsubouchi, H. Nakagawa, T. Yamanaka, T. Doi, T. Abe, Z. Ogumi, *J. Electrochem. Soc*., **159** (2012) A1292−A1297.

[52] Y. Domi, T. Doi, T. Yamanaka, T. Abe, Z. Ogumi, *J. Electrochem. Soc*., **160** (2013) A678−A683.

[53] J.-A. Choi, D.-W. Kim, Y.-S. Bae, S.-W. Song, S.-H. Hong, S.-M. Lee, *Electrochim Acta*, **56** (2011) 9818−9823.

[54] H. Usui, M. Shimizu, H. Sakaguchi, *J. Power Sources,* **235** (2013) 29−35.

[55] H. Usui, T. Masuda, H. Sakaguchi, *Chem. Lett.*, **41** (2012) 521−522.

[56] J. C. Lassegues, J. Grondin, D. Talaga, *Phys. Chem. Chem. Phys*., **8** (2006) 5629−5632.

[57] Y. Umebayashi, T. Mitsugi, S. Fukuda, T. Fujimori, K. Fujii, R. Kanzaki, M. Takeuchi, S. Ishiguro, *J. Phys. Chem. B*, **111**, (2007) 13028−13032.

[58] Y. Umebayashi, S. Mori, K. Fujii, S. Tsuzuki, S. Seki, K. Hayamizu, S. Ishiguro, *J. Phys. Chem. B*, **114** (2010) 6513−6521.

[59] M. Yamagata, N. Nishigaki, S. Nishishita, Y. Matsui, T. Sugimoto, M. Kikuta, T. Higashizaki, M. Kono, M. Ishikawa, *Electrochim. Acta*, **110** (2013) 181−190.

[60] Y. Katayama, R. Fukui, T. Miura, *J. Electrochem. Soc*., **154** (2007) D534−D537.

[61] Y. Yamada, Y. Iriyama, T. Abe, Z. Ogumi, *J. Electrochem. Soc*., **157** (2010) A26−A30.

[62] K. Yoshida, M. Tsuchiya, N. Tachikawa, K. Dokko, M. Watanabe, *J. Electrochem. Soc*., **159** (2012) A1005−A1012.

[63] B. Baek, S. Lee, C. Jung, Int. *J. Electrochem. Sci*., **6** (2011) 6220−6234.

[64] Y. Wang, K. Zaghib, A. Guerfi, F.F.C. Bazito, R.M. Torresi, J.R. Dahn, *Electrochim. Acta*, **52** (2007) 6346−6352.

[65] H. Sakaguchi, T. Toda, Y. Nagao,T. Esaka, *Electrochem. Solid-State Lett*., **10** (2007) J146−J149.

[66] T. Nokami, K. Matsumoto, T. Itoh, Y. Fukaya T. Itoh, *Org. Process Res. Dev*., **18** (2014) 1367−1371.

[67] H.-B. Han, K. Liu, S.-W. Feng, S.-S. Zhou, W.-F. Feng, J. Nie, H. Li, X.-J. Huang, H. Matsumoto, M. Armand, Z.-B. Zhou, *Electrochim. Acta*, **55** (2010) 7134−7144.

[68] J. Reiter, E. Paillard, L. Grande, M. Winter, S. Passerini, *Electrochim. Acta*, **91** (2013) 101−107.

[69] K. Tsunashima, A. Kawabata, M. Matsumiya, S. Kodama, R. Enomoto, M. Sugiya, Y. Kunugi, *Electrochem. Commun*., **13** (2011) 178−181.

[70] J.-T. Li, J. Swiatowska, A. Seyeux, L. Huang, V. Maurice, S.-G. Sun, P. Marcus, *J. Power Sources*, **195** (2010) 8251−8257.

[71] I. Rey, P. Johansson, J. Lindgren, J. C. Lassègues, J. Grondin, L. Servant, *J. Phys. Chem. A*, **102** (1998) 3249−3258.

[72] S. P. Gejji, C. H. Suresh, K. Babu, S. R. Gadre, *J. Phys. Chem. A*, **103** (1999) 7474−7480.

[73] M. Herstedt, M. Smirnov, P. Johansson, M. Chami, J. Grondin, L. Servant, J. C. Lassègues, *J. Raman Spectrosc*., **36**, (2005) 762−770.

[74] M. Kunze, S. Jeong, E. Paillard, M. Schönhoff, M. Winter, S. Passerini, *Adv. Energy Mater*., **1** (2011) 274−281.

[75] S. Tsuzuki, H. Tokuda, K. Hayamizu, M. Watanabe, *J. Phys. Chem. B*, **109**, (2005) 16474−16481.

[76] S. Tsuzuki, K. Hayamizu, S. Seki, Y. Ohno, Y. Kobayashi, H. Miyashiro, *J. Phys. Chem. B*, **112** (2008) 9914−9920.

[77] J.-W. Song, C. C. Nguyen, S.-W. Song, *RSC Adv*., **2** (2012) 2003−2009.

[78] M.K. Datta, P.N. Kumta, *J. Power Sources*, **194** (2009) 1043−1052.

[79] N. Yabuuchi, K. Shimomura, Y. Shimbe, T. Ozeki, J.-Y. Son, H. Oji, Y. Katayama, T. Miura, S. Komaba, *Adv. Energy Mater*., **1** (2011) 759−765.

[80] V. Chakrapani, F. Rusli, M. A. Filler, P. A. Kohl, *J. Phys. Chem. C*, **115** (2011) 22048−22053.

[81] F. Sagane, T. Abe, Z. Ogumi, *J. Electrochem. Soc*., **159** (2012) A1766−A1769.

[82] Y. Ishihara, K. Miyazaki, T. Fukutsuka, T. Abe, *J. Electrochem. Soc*., **161** (2014) A1939−A1942.

[83] M. Shimizu, H. Usui, K. Matsumoto, T. Nokami, T. Itoh, H. Sakaguchi, *J. Electrochem. Soc*., **161** (2014) A1765−A1771.

[84] M. Egashira, A. Kanetomo, N. Yoshimoto, M. Morita, *J. Power Sources*, **196** (2011) 6419−6424.

[85] T. Ohzuku, A. Ueda, N. Yamamoto, *J. Electrochem. Soc*., **142** (1995) 1431−1435.

[86] Y. H. Rho, K. Kanamura, *J. Solid State Chem*., **177** (2004) 2094−2100.

[87] L. Aldon, P. Kubiak, M. Womes, J. C. Jumas, J. Olivier-Fourcade, J. L. Tirado, J. I. Corredor, C. P. Vicente, *Chem. Mater.*, **16** (2004) 5721−5725.

[88] J. Haetge, P. Hartmann, K. Brezesinski, J. Janek, T. Brezesinski, *Chem. Mater*., **23** (2011) 4384−4393.

[89] H.-G. Jung, S.-T. Myung, C. S. Yoon, S.-B. Son, K. H. Oh, K. Amine, B. Scrosati, Y.-K. Sun, *Energy Environ. Sci.,* **4** (2011) 1345−1351.

[90] T. Abe, H. Fukuda, Y. Iriyama, Z. Ogumi, *J. Electrochem. Soc*., **151** (2004) A1120−A1123.

[91] Y. Yamada, Y. Iriyama, T. Abe, Z. Ogumi, *Langmuir*, **25** (2009) 12766−12770.

[92] T. Doi, Y. Iriyama, T. Abe, Z. Ogumi, *Anal. Chem*., **77** (2005) 1696−1700.

[93] J. Evans, C. A. Vincent, P. G. Bruce, *Polymer*, **28** (1987) 2324−2328.

[94] S. Seki, Y. Ohno, H. Miyashiro, Y. Kobayashi, A. Usami, Y. Mita, N. Terada, K. Hayamizu, S. Tsuzuki, M. Watanabe, *J. Electrochem. Soc*, **155** (2008) A421−A427.

[95] K. Matsumoto, Y. Okamoto, T. Nohira, R. Hagiwara, *J. Phys. Chem. C*, **119** (2015) 7648−7655.

[96] M. Morita, Y. Asai, N. Yoshimoto, M. Ishikawa, *J. Chem. Soc., Faraday Trans.*, **94** (1998) 3451−3456.

[97] Y. Yamada, Y. Koyama, T. Abe, Z. Ogumi, *J. Phys. Chem. C*, **113** (2009) 8948–8953.

[98] K. Xu, A. von Cresce, U. Lee, *Langmuir*, **26** (2010) 11538−11543.

[99] S. Duluard, J. Grondin, J.-L. Bruneel, I. Pianet, A. Grélard, G. Campet, M.-H. Delville, J.-C. Lassègues, *J. Raman Spectrosc*., **39** (2008) 627−632.

[100] S. Menne, T. Vogl, A. Balducci, *Phys. Chem. Chem. Phys*., **16** (2014) 5485−5489.

[101] C.C. Nguyen, S.-W. Woo, S.-W. Song, *J. Phys. Chem. C*, **116** (2012) 14764−14771.

[102] M. Nie, D.P. Abraham, Y. Chen, A. Bose, B.L. Lucht, *J. Phys. Chem. C*, **117** (2013) 13403−13412.

[103] A. Tokranov, B.W. Sheldon, C. Li, S. Minne, X. Xiao, *ACS Appl. Mater. Interfaces*, **6** (2014) 6672−6686.

[104] X. H. Liu, L. Zhong, S. Huang, S-X. Mao, T. Zhu, J. Y. Huang, *ACS Nano,* **6** (2012) 1522−1531.

[105] H. Wu, G. Chan, J.W. Choi, I. Ryu, Y. Yao, M.T. McDowell, S.W. Lee, A. Jackson, Y. Yang, L. Hu, Y. Cui, *Nature Nanotech*., **7** (2012) 310−315.

[106] T. Gruber, D. Thomas, C. Röder, F. Mertens, J. Kortus, *J. Raman Spectrosc*., **44** (2013) 934−938.

[107] J. Nanda, M.K. Datta, J.T. Remillard, A. O'Neill, P.N. Kumta, *Electrochem. Commun*., **11** (2009) 235−237.

[108] S. Murugesan, J.T. Harris, B.A. Korgel, K.J. Stevenson, *Chem. Mater*., **24** (2012) 1306−1315.

[109] C. Pereira-Nabais, J. Światowska, A. Chagnes, F. Ozanam, A. Gohier, P. Tran-Van, C.-S. Cojocaru, M. Cassir, P. Marcus, *Appl. Surf. Sci.*, **266** (2013) 5−16.

[110] M. Gauthier, D. Mazouzi, D. Reyter, B. Lestriez, P. Moreau, D. Guyomard, L. Roué, *Energy Environ. Sci*., **6** (2013) 2145−2155.

[111] M.T. McDowell, S.W. Lee, J.T. Harris, B.A. Korgel, C. Wang, W.D. Nix, Y. Cui, *Nano lett*., **13** (2013) 758−764.

[112] S. H. Won, J. H. Youn, J. Jang, *J. Korean Phys. Soc*., **39** (2001) 123−126

[113] R.C. Teixeira, I. Doi, M.B.P. Zakia, J.A. Diniz, J.W. Swart, *Mater. Sci. Eng. B*, **12** (2004) 160−164.

[114] B. Key, M. Morcrette, J.-M. Tarascon, C. P. Grey, *J. Am. Chem. Soc*., **133** (2011) 503−512.

[115] B. Philippe, R. Dedryvère, J. Allouche, F. Lindgren, M. Gorgoi, H. Rensmo, D. Gonbeau, K. Edström, *Chem. Mater.*, **24** (2012) 1107−1115.

[116] M. Thakur, S.L. Sinsabaugh, M.J. Isaacson, M.S. Wong, S.L. Biswal, *Sci. Rep*., **2** (2012) 795.

[117] L.-F. Cui, L. Hu, H. Wu, J.W. Choi, Y. Cui, *J. Electrochem. Soc*., 158 (2011) A592−A596.

[118] M. K. Datta, R. Epur, P. Saha, K. Kadakia, S. K. Park, P. N. Kumta, *J. Power Sources,* **225** (2013) 316−322.

[119] V. L. Chevrier, G. Ceder, *J. Electrochem. Soc*., **158** (2011) A1011−A1014.

[120] T. Yamamoto, T. Nohira, R. Hagiwara, A. Fukunaga, S. Sakai, K. Nitta, S. Inazawa, *J. Power Sources*, **217** (2012) 479−484.

[121] Y. Xu, Y. Zhu, Y. Liu , C. Wang, *Adv. Energy Mater*., **3** (2013) 128−133.

[122] S. Komaba, Y. Matsuura, T. Ishikawa, N. Yabuuchi, W. Murata, S. Kuze, *Electrochem. Commun*., **21** (2012) 65−68.

[123] Y. Idota, T. Kubota, A. Matsufuji, Y. Maekawa, T. Miyasaka, *Science*, **276** (1997) 1395−1397.

[124] D. Aurbach, A. Nimberger, B. Markovsky, E. Levi, E. Sominski, A. Gedanken, *Chem. Mater*., **14** (2002) 4155−4163.

[125] S.-C. Chao, Y.-C. Yen, Y.-F. Song, H.-S. Sheu, H.-C. Wu, N.-L. Wu, *J. Electrochem. Soc*., **158** (2011) A1335−1339.

[126] I. A. Courtney, W. R. McKinnon, J. R. Dahn, *J. Electrochem. Soc*., **146** (1999) 59−68.

[127] M. Shimizu, H. Usui, T. Suzumura, H. Sakaguchi, *J. Phys. Chem. C*, **119** (2015) 2975−2982.

[128] L. D. Ellis, T. D. Hatchard, M. N. Obrovac, *J. Electrochem. Soc*., **159** (2012) A1801−A1805.

[129] J.-T. Li, J. Swiatowska, A. Seyeux, L. Huang, V. Maurice, S.-G. Sun, P. Marcus, *J. Power Sources*, **195** (2010) 8251−8257.

[130] L. Xiao, Y. Cao, J. Xiao, W. Wang, L. Kovarik, Z. Nie, J. Liu, *Chem. Commun*., **48** (2012) 3321−3323.

[131] H. Nakai, T. Kubota, A. Kita, A. Kawashima, *J. Electrochem. Soc*., **158** (2011) A798−A801.

[132] J. Qian, X. Wu, Y. Cao, X. Ai, H. Yang, *Angew. Chem.,* **125** (2013) 4731−4734.

[133] S. Komaba, T. Ishikawa, N. Yabuuchi, W. Murata, A. Ito, Y. Ohsawa, *ACS Appl. Mater. Interfaces*, **3** (2011) 4165−4168.

[134] J. Qian, Y. Chen, L. Wu, Y. Cao, X. Ai, H. Yang, *Chem. Commun*., **48** (2012) 7070−7072.

[135] P.R. Abel, Y.-M. Lin, T. de Souza, C.-Y. Chou, A. Gupta, J.B. Goodenough, G.S. Hwang, A. Heller, C.B. Mullins, *J. Phys. Chem. C,* **117** (2013) 18885−18890.

[136] J. Sangster, A. D. Pelton, *J. Phase Equilib*. **13** (1992) 67−69.

[137] H. Morito, T. Yamada, T. Ikeda, H. Yamane, *J. Alloys Comp*. **480** (2009) 723−726.

[138] Y. Nagao, H. Sakaguchi, H. Honda, T. Fukunaga, T. Esaka, *J. Electrochem. Soc*., **151** (2004) A1572−A1575.

[139] J.I. Lee, K.T. Lee, J. Cho, J. Kim, N.S. Choi, S. Park, *Angew. Chem. Int. Ed.,* **51** (2012) 2767−2771.

[140] J.-H. Kim, H.-J. Sohn, H. Kim, G. Jeong, W. Choi, *J. Power Sources*, **170** (2007) 456−459.

[141] T. Kim, S. Park, S.M. Oh, *J. Electrochem. Soc*., **154** (2007) A1112−A1117.

[142] V. M. Marchenko, V. V. Koltashev, S. V. Lavrishchev, D. I. Murin, V. G. Plotnichenko, *Laser Physics*, **10** (2000) 576−582.

[143] L.D. Ellis, B.N. Wilkes, T.D. Hatchard, M.N. Obrovac, *J. Electrochem. Soc*., **161** (2014) A416−A421.

[144] H. Yamamura, K. Nobuhara, S. Nakanishi, H. Iba, S. Okada, *J. Ceram. Soc. Japan,* **119** (2011) 855−860.

[145] N. Yan, F. Wang, H. Zhong, Y. Li, Y. Wang, L. Hu, Q. Chen, *Sci. Rep*., **3** (2013) 1568.

[146] S.C. Jung, D.S. Jung, J.W. Choi, Y.-K. Han, *J. Phys. Chem. Lett*., **5** (2014) 1283−1288.

[147] N. Yabuuchi, Y. Matsuura, T. Ishikawa, S. Kuze, J.-Y. Son, Y.-T. Cui, H. Oji, S. Komaba, *ChemElectroChem*, **1** (2014) 580−589.

[148] J. Qian, Y. Xiong, Y. Cao, X. Ai, H. Yang, *Nano Lett*., **14** (2014) 1865−1869.

[149] Y. Kim, Y. Park, A. Choi, S. Woo, D. Mok, N.-S. Choi, Y. S. Jung, J. H. Ryu, S. M. Oh, K. T. Lee, *Adv. Mater*., **26** (2014) 4139−4144.

[150] J. Y. Jang, Y. Lee, Y. Kim, J. Lee, S.-M. Lee, K. T. Lee, N.-S. Choi, *J. Mater. Chem. A*, **3** (2015) 8332−8338.

[151] M. Shimizu, H. Usui, H. Sakaguchi, J. Power Sources, **248** (2014) 378−382.

[152] M. Shimizu, H. Usui, K. Fujiwara, K. Yamane, H. Sakaguchi, *J. Alloys Compd*, **640** (2015) 440−443.

[153] H. Usui, S. Yoshioka, K. Wasada, M. Shimizu, H. Sakaguchi, *ACS Appl. Mater. Interfaces*, **7** (2015) 6567−6573.

[154] C. Ding, T. Nohira, R. Hagiwara, K. Matsumoto, Y. Okamoto, A. Fukunaga, S. Sakai, K. Nitta, S. Inazawa, *J. Power Sources*, **269** (2014) 124−128.

[155] W.J. Li, S.L. Chou, J.Z. Wang, H.K. Liu, S.X. Dou, *Nano Lett*., **13** (2013) 5480−5484.

[156] L. Lombardo, S. Brutti, M.A. Navarra, S. Panero, P. Reale, *J. Power Sources*, **227** (2013) 8−14.

[157] ISO3679:2004, https://www.iso.org/obp/ui/#iso:std:iso:3679:ed-3:v1:en, (accessed April 2015).

[158] JISK2265-2, http://www.jisc.go.jp/app/pager?id=538998, (accessed April 2015).

[159] C. A. Vanderborgh, D. Schiferl, *Phys. Rev. B*, **40** (1989) 9595−9599.

[160] D. Monti, E. Jónsson, M.R. Palacín, P. Johansson, *J. Power Sources*, **245** (2014) 630−636.

[161] A. Fukunaga, T. Nohira, R. Hagiwara, K. Numata, E. Itani, S. Sakai, K. Nitta, S. Inazawa, *J. Power Sources*, **246** (2014) 387−391.

[162] M.C. Buzzeo, R.G. Evans, R.G. Compton, *ChemPhysChem*, **5** (2004) 1106−1120.

[163] Y. Kim, Y. Park, A. Choi, N.S. Choi, J. Kim, J. Lee, J.H. Ryu, S.M. Oh, K.T. Lee, *Adv. Mater*., **25** (2013) 3045−3049.

[164] N. Wongittharom, C.H. Wang, Y.C. Wang, C.H. Yang, J.K. Chang, *ACS Appl. Mater. Interfaces*, **6** (2014) 17564−17570.

[165] A. Ponrouch, E. Marchante, M. Courty, J.-M. Tarascon, M.R. Palacín, *Energy Environ. Sci*., **5** (2012) 8572−8583.

List of Publications

[1] Effect of Film-Forming Additives on Electrochemical Performances of Silicon Negative-Electrode in Lithium-Ion Batteries
Y. Domi, H. Usui, M. Shimizu, K. Miwa, and H. Sakaguchi,
Int. J. Electrochem. Sci., **10** (2015) 9678–9686.

[2] Effect of cation structure of ionic liquid on anode properties of Si electrodes for LIB
M. Shimizu, H. Usui, K. Matsumoto, T. Nokami, T. Itoh, and H. Sakaguchi,
J. Electrochem. Soc., **161** (12) (2014) A1765–A1771.

[3] Effect of cation structure of ionic liquid on anode properties of Si electrodes for LIB
M. Shimizu, H. Usui, K. Matsumoto, T. Nokami, T. Itoh, and H. Sakaguchi,
J. Electrochem. Soc., **161** (12) (2014) A1765–A1771.

[4] Functional ionic liquid for enhancement of Li-ion transfer: Effect of cation structure on charge−discharge performance of $Li_4Ti_5O_{12}$ electrode
M. Shimizu, H. Usui, and H. Sakaguchi,
Phys. Chem. Chem. Phys., (2016) *in press.*

[5] Electrochemical Na-insertion/extraction properties of SnO thick-film electrodes prepared by gas-deposition
M. Shimizu, H. Usui, and H. Sakaguchi,
J. Power Sources, **248** (2014) 378–382.

[6] Electrochemical behavior of SiO as an anode material for Na-ion battery
M. Shimizu, H. Usui, K. Fujiwara, K. Yamane, and H. Sakaguchi,
J. Alloys Compd., **640** (2015) 440–443.

[7] Electrochemical Na-insertion/extraction properties of Sn-P anodes
H. Usui, T. Sakata, M. Shimizu, and H. Sakaguchi,
Electrochemistry, **83** (10) (2015) 810–812.

[8] Electrochemical Na-insertion/extraction properties of phosphorus electrodes in ionic liquid electrolytes
M. Shimizu, H. Usui, K. Yamane, T. Sakata, T. Nokami, T. Itoh, and H. Sakaguchi,
Int. J. Electrochem. Sci., **10** (2015) 10132–10144.

Supplementary Publications

[1] Applicability of ionic liquid electrolytes to $LaSi_2$/Si composite thick-film anodes in Li-ion battery
H. Usui, M. Shimizu, and H. Sakaguchi,
J. Power Sources, **235** (2013) 29–35.

[2] TiO_2/Si composites synthesized by sol–gel method and their improved electrode performance as Li-ion battery anodes
H. Usui, K. Wasada, M. Shimizu, and H. Sakaguchi,
Electrochim. Acta, **111** (2013) 575–580.

[3] Nb-Doped Rutile TiO_2: a Potential Anode Material for Na-Ion Battery
H. Usui, S. Yoshioka, K. Wasada, M. Shimizu, and H. Sakaguchi,
ACS Appl. Mater. Interfaces, **7** (12) (2015) 6567–6573.